

**COMPARISONS OF NUCLEIC ACID DUPLEXES PROVIDE FUNDAMENTAL
INSIGHT INTO LONG-RANGE SINGLE MOLECULE CONDUCTANCE**

by

Edward Joseph Beall

B.S., Lebanon Valley College, 2013

Submitted to the Graduate Faculty of
the Dietrich School of Arts and Sciences in partial fulfillment
of the requirements for the degree of
Doctor of Philosophy.

University of Pittsburgh
2018

UNIVERSITY OF PITTSBURGH

Dietrich School of Arts and Sciences

This dissertation was presented

by

Edward Beall

It was defended on

August 23rd, 2018

and approved by

Dr. Shigeru Amemiya, Professor, Department of Chemistry

Dr. Sean Garrett-Roe, Assistant Professor, Department of Chemistry

Dr. Catalina Achim, Professor, Department of Chemistry, Carnegie Mellon University

Dissertation Advisor: Dr. David Waldeck, Professor, Department of Chemistry

Copyright © by Edward Beall
2018

COMPARISONS OF NUCLEIC ACID DUPLEXES PROVIDE FUNDAMENTAL INSIGHT INTO LONG-RANGE SINGLE MOLECULE CONDUCTANCE

Edward Beall, PhD
University of Pittsburgh, 2018

The understanding of charge transfer on the nanoscale is rapidly expanding and achievement in the construction of increasingly intricate single molecule platforms is advancing the field of molecular electronics. Functional biomimetic structures are the subject and pursuit of considerable research aimed at continuing the miniaturization of electrical components. In this dissertation, fundamental factors affecting charge transfer are investigated through the measurement of single molecule conductance. In the first study, an experimental procedure is presented that includes a modulated bias and a novel data analysis technique. This technique is utilized in the subsequent studies. In the second study, the effect of the flexibility of nucleic acid duplexes on their single molecule conductance is shown. It is found that the single molecule conductance increases as the flexibility of the backbone increases. The third study determines the effect of a nick in the backbone of the duplex. The nicked duplexes are shown to have a more variable single molecule conductance relative to their full analogues, while the average conductance values agree for both duplex types. The final study furthers recent work on DNA duplexes by comparing them to the single molecule conductance of PNA duplexes of varying lengths. The length dependence of the single molecule conductance does not show the oscillatory effect observed for DNA duplexes, shedding light on the relevant charge transfer mechanism. The results of these studies serve to progress the field of molecular electronics and will aid in future studies elucidating the underlying aspects governing electron transfer.

TABLE OF CONTENTS

LIST OF TABLES	XII
LIST OF FIGURES	XIV
LIST OF EQUATIONS.....	XXIV
LIST OF SCHEMES	XXV
PREFACE.....	XXVI
1.0 INTRODUCTION.....	1
1.1 INTRODUCTION TO MOLECULAR ELECTRONICS	1
1.2 PRELIMINARY STUDIES IN SINGLE MOLECULE CONDUCTANCE.....	1
1.3 BIOMOLECULES AS CANDIDATES FOR MOLECULAR ELECTRONICS	3
1.3.1 Preliminary Studies in DNA Conductance.....	4
1.4 MECHANISMS OF CHARGE TRANSFER.....	5
1.4.1 Coherent Tunneling.....	6
1.4.2 Incoherent Charge Hopping.....	6
1.4.3 Flickering Resonance	7
1.4.4 Interplay of Charge Transfer Mechanisms.....	8
1.5 MOLECULAR LINKERS	9
1.5.1 Conductance Modes	9
1.5.2 Backbone Linkers	10
1.5.3 Base Stack Linkers	11
1.6 ELECTROCHEMICAL CHARGE TRANSFER RATE AND CONDUCTANCE... 	11
1.7 DISSERTATION OUTLINE.....	13
1.8 REFERENCES.....	15

2.0	A SCANNING TUNNELING MICROSCOPE BREAK JUNCTION METHOD WITH CONTINUOUS BIAS MODULATION.....	20
2.1	INTRODUCTION.....	21
2.2	RESULTS AND DISCUSSION	22
	2.4.1 Conductance Measurements.....	35
	2.4.1.1 Sample Preparation	36
	2.4.1.2 Data Collection	36
	2.4.1.3 Data Analysis	37
	2.4.2 Calculation of the Dipole Moment of Solvent Molecules Under Various Electrical Fields.....	38
2.5	REFERENCES.....	38
3.0	EFFECTS OF THE BACKBONE AND CHEMICAL LINKER ON THE MOLECULAR CONDUCTANCE OF NUCLEIC ACID DUPLEXES.....	40
3.1	INTRODUCTION.....	41
3.2	RESULTS	45
	3.2.1 Conductance Measurements.....	45
	3.2.1.2 Linker Study.....	51
	3.2.1.3 Summary.....	53
	3.2.2 Computational Results.....	54
3.3	CONCLUSIONS	58
3.4	METHODS	59
	3.4.1 Synthesis of PNA Monomers and Linkers	59
	3.4.2 Synthesis of ^LS-^γPNA Monomers.....	60

3.4.3	Synthesis of PNA Oligomers.....	61
3.4.4	Preparation of Samples for Conductance Measurements	62
3.4.4.1	Nucleic Acid Duplexes	62
3.4.4.2	Gold Substrates	62
3.4.5	Conductance Measurements and Analysis.....	63
3.4.6	Molecular Dynamics.....	64
3.4.7	Conductance Calculations	64
3.5	REFERENCES.....	65
4.0	THE MOLECULAR CONDUCTANCE OF NICKED NUCLEIC ACID DUPLEXES	69
4.1	INTRODUCTION.....	70
4.2	RESULTS	72
4.2.1	Characterization of the Nucleic Acids	72
4.2.1.1	Melting Curves	73
4.2.1.2	Circular Dichroism Spectra	73
4.2.1.3	Fluorescence Spectra for the DNA/PNA Heteroduplexes	74
4.2.2	The Effect of the Nick on the Conductance of the Duplexes	75
4.2.3	Effect of PNA Content on Conductance.....	81
4.3	DISCUSSION	83
4.4	CONCLUSION	86
4.5	METHODS	86
4.5.1	PNA Synthesis.....	86
4.5.2	Conductance Measurements.....	87

4.5.2.1	Substrate Fabrication	87
4.5.2.2	Data Collection	88
4.5.2.3	Data Analysis	88
4.6	REFERENCES.....	88
5.0	EFFECT OF FLEXIBILITY ON THE INTERPLAY OF COHERENCE AND INCOHERENCE IN NUCLEIC ACID CONDUCTANCE.....	92
5.1	INTRODUCTION.....	92
5.2	RESULTS	95
5.3	DISCUSSION	97
5.4	METHODS	98
5.4.1	PNA Synthesis.....	98
5.4.2	PNA Characterization.....	98
5.4.3	Substrate Preparation	99
5.4.4	Conductance Measurements.....	99
5.4.5	Data Analysis	99
5.5	REFERENCES.....	100
6.0	CONCLUDING REMARKS	103
	APPENDIX A.....	106
A.1	CURRENT RESPONSE OF THE SOLVENTS ON THE BIAS APPLIED WITH VARIOUS MODULATION FREQUENCIES.....	106
A.2	INFLUENCE OF MACROSCOPIC GEOMETRICAL FACTORS ON THE CAPACITIVE CURRENT WAVEFORMS.....	108
A.3	REFERENCES.....	110

APPENDIX B	111
B.1 SOLID-PHASE PNA SYNTHESIS	111
B.1.1 General Procedures	112
B.1.2 Synthesis of Propyl Thiol Linker Containing PNAs.....	113
B.1.3 Synthesis of 4-(Tritylthio)Butyric Acid.....	114
B.1.4 Synthesis of T_(C2-NH2) Linker Containing PNAs.....	115
B.1.5 Synthesis of Thymidine 5-C2 Amino Linker	116
B.2 CONDUCTANCE MEASUREMENTS.....	119
B.2.1 Equipment	119
B.2.2 Nucleic Acid Duplexes	119
B.2.3 Gold Substrates	120
B.2.4 Conductance Measurements	120
B.2.5 Data Analysis.....	121
B.2.6 Thiol Location Control.....	121
B.2.7 Mode Analysis	122
B.3 COMPUTATIONAL RESULTS	124
B.3.1 The Electronic Coupling Strength Between Nearest Neighbor Purine Sites	124
B.3.2 Simulation Results of Helical Parameter Thermal Fluctuations.....	125
B.3.3 Linker Study.....	127
B.4 REFERENCES	130
APPENDIX C	131
C.1 NUCLEIC ACID SEQUENCES.....	131
C.2 MATERIALS AND METHODS	132

C.2.1	Synthesis of PNA Oligomers	132
C.2.2	Attachment of Pyrene to the C-End Of PNA	132
C.2.3	Attachment of Pyrene to the N-end of PNA	133
C.2.4	Thermal Stability	133
C.2.5	Chirality of the Nicked Homo- and Heteroduplexes	134
C.2.6	Fluorescence Studies.....	135
C.2.7	Conductance Measurements.....	135
C.2.7.1	Equipment.....	135
C.2.7.2	Nucleic Acid Duplexes.....	136
C.2.7.3	Substrate Fabrication	136
C.2.7.4	Substrate Preparation.....	136
C.2.7.5	Conductance Measurements	136
C.2.7.6	Data Analysis	137
C.2.8	Thiol Location Control.....	137
C.2.9	Serial Correlation	139
C.3	DNA CONDUCTANCE COMPARISON.....	141
C.4	REFERENCES.....	142
	APPENDIX D.....	144
D.1	BACKGROUND CONTROL EXPERIMENTS.....	144
	APPENDIX E:.....	146
E.1	CELL PREPARATION.....	146
E.2	STAGE PREPARATION	146
E.3	SCANNER PREPARATION	147

E.4	APPLICATION OF THE EXTERNAL BIAS	148
E.5	DATA ACQUISITION	150
E.6	DATA ANALYSIS	151
E.6.1	Reading and Filtering Trajectories	151
E.6.2	Creating the Sample Trajectories	152
E.6.3	Partitioning the Dataset.....	153
E.6.4	Fitting the Partitioned Dataset	155
E.6.5	Excluding the Worst-Fit Modulation Periods	156

LIST OF TABLES

Table 3.1: Summary of the single molecule conductance measurements for the nucleic acid duplexes.	54
Table 4.1. Melting Temperatures (T_m) of Nucleic Acid Duplexes.	73
Table 4.2. Summary of the single molecule conductance, G , and its standard deviation, σ_G , for the nucleic acid duplexes.	83
Table B.1. PNA sequences and MALDI data.	111
Table B.2. The applied bias for each measured duplex.	121
Table B.3. The relative fraction of the high conductance mode calculated for the studied duplexes using the fitted Gaussian functions.	123
Table B.4: Root-mean-square of coupling strengths (in front of \pm) and found for the nucleic acid duplexes in eV.....	125
Table B.5: Mean values and standard deviations of DNA helical parameters (from 10,000 MD snapshots).....	125
Table B.6: Mean values and standard deviations of aeg-PNA helical parameters (from 10,000 MD snapshots).....	125
Table B.7: Mean values and standard deviations of γ -PNA helical parameters (from 10,000 MD snapshots).....	126
Table B.8: Mean values and standard deviations of aeg-PNA-DNA helical parameters (from 10,000 MD snapshots).	126
Table B.9. Summary of the contact distance calculations for the measured duplexes.	130
Table C.1. Sequence of oligonucleotides ^a	131
Table C.2. Oligomer Sequences and MALDI MS Data	133

Table C.3. Summary of Thermal Stabilities for DNA/DNA and PNA/PNA Homoduplexes(T_m [°C]), and DNA/PNA Heteroduplexes(T_m [°C]) 134

LIST OF FIGURES

- Figure 1.1.** A) The STM-BJ technique is demonstrated. The black spheres are gold atoms and the linkers are shown as yellow spheres on the molecular termini. B) The current responses for the STM-BJ technique show current plateaus corresponding to molecular junctions during the tip retraction process. C) A current histogram is shown to demonstrate how the current responses are compiled to reflect the most probable molecular conductance. (Taken from Ref. 9) 3
- Figure 1.2.** The length dependence of the single molecular conductance is shown for two different families of DNA duplexes. An exponential dependence is shown for sequences containing AT pairs (A) and an inversely proportional dependence is observed for sequences with only GC pairs..... 5
- Figure 1.3.** A) The structure of the thiol, backbone linkers are shown for DNA molecular junctions. B) The base stack linker (blue) is shown as a thymine (red) modification as a linkage between the Au electrodes. (Taken from Ref. 57) 11
- Figure 1.4.** The single-molecule conductance versus the electrochemical charge transfer rate constant is shown for alkanes (red), single strand PNA constructed of thymine nucleotides (green), and double stranded PNAs (blue). 12
- Figure 2.1.** Panel A shows a schematic illustration of the molecular junction formed in a scanning tunneling microscope with a gold tip and gold substrates as the electrodes. Panels B and C show sample current – time traces obtained in the presence of 1,8-octanedithiol in mesitylene solvent, measured under a constant bias of 0.3 V (B) and a modulated bias of 0.3 ± 0.3 V (C). In both cases the retraction speed is 40 nm/s. Black traces in B and C are characteristic for molecule-free junctions. Arrows indicate the current responses of the molecules trapped in the junction. 23
- Figure 2.2.** Panels A through C show current responses of the solvent under a bias voltage of 0.3 V that is modulated by 0.3 V at a frequency of 500 Hz for (A) mesitylene (dielectric constant

$\epsilon=2.28$)¹⁴, (B) 2,4-dichlorotoluene ($\epsilon=5.68$)¹⁴, and (C) 3,4-dichlorotoluene ($\epsilon=8.97$)¹⁵. Panel D shows calculated results for the influence of the electrical field strength on the dipole moment induced in these molecules. Note that zero electric field corresponds to the static dipole moment of the solvent molecules..... 25

Figure 2.3. Panels A and B show sample current – time traces obtained in the presence of 1,8-octanedithiol in mesitylene (A) and in 2,4-dichlorotoluene (B) solvent, measured under a bias of 0.3 ± 0.3 V modulated with frequency of 500 Hz. Panel C shows histograms of many current versus time traces, measured in mesitylene and in 2,4-dichlorotoluene. The currents corresponding to a narrow 0.29 – 0.31 V range of applied bias (shown schematically in the inset in panel C as yellow box) were extracted to construct the distributions. Data obtained under constant bias of 0.3 V in mesitylene is shown for comparison. The current response characteristic for the solvent was not included in the analysis..... 27

Figure 2.4. Results of fitting the experimental current versus time trace using a model electrical circuit. Panel A shows a sample experimental curve obtained in mesitylene under 0.3 ± 0.3 V bias modulation applied with 500 Hz frequency (black symbols), together with a simulated current response of the model electrical circuit (red lines). In the model electrical circuit, the measured molecule (1,8-octanedithiol) is represented as a resistor (R_M), and the solvent is modeled as a leaky capacitor [two resistors (R_S , R_S') and a capacitor (C_S)]. Parameters of the circuit elements associated with the solvent were kept constant ($R_S'=1 \times 10^{11}$ Ω , $R_S=9 \times 10^8$ Ω , $C_S=8.25 \times 10^{-14}$ F). The simulations were performed to match each individual modulation period in the experimental curve using the most general circuit presented in the bottom row of the figure (green rectangle). Circuits in the blue and yellow rectangular region represent limiting approximations of the most general model circuit (green), in which the current response is determined solely by the molecule

trapped in the junction (blue) or by the response of the solvent media alone (yellow). Panel B shows R_M values obtained for the 1,8-octanedithiol molecule in the current-time profile shown in panel A. 30

Figure 2.5. Results of fittings to experimental data with the model electrical circuit. Panel A shows a sample experimental curve obtained in mesitylene under 0.3 ± 0.3 V bias modulation applied with 500 Hz frequency (black symbols), together with a simulated current response of the model electrical circuit (red lines). Panel B shows examples of modulation periods, within which a change in the conformation of the molecules in the junction was observed. Only fits shown in red are included in panel A. Circuit parameters associated with the solvent are the same for all the simulated data ($R_S'=1.0 \times 10^{11} \Omega$, $R_S=9.0 \times 10^8 \Omega$, $C_S=7.8 \times 10^{-14}$ F). Panel C shows the fitted R_M value corresponding to subsequent modulation periods shown in panels A (red symbols) and B (violet symbols). 32

Figure 2.6. Panel A shows a two-dimensional current – voltage distribution constructed from two thousand current - time traces recorded for 1,8-octanedithiol in mesitylene under the bias modulation conditions of 0.3 ± 0.3 V (500 Hz). Because the bias voltage is generated continuously and is independent of the STM tip withdrawal procedure, the applied bias and the current measured in the junction were matched in phase based on the characteristic response of the solvent to the applied bias. Panel B shows the octanedithiol conductance distribution obtained by matching the modulation periods in experimental traces (blue histogram) with the library of two hundred current responses simulated for the circuits with predefined R_M values in a range 10^7 - 10^{11} ohm. Parameters of the circuit elements associated with the solvent were kept constant ($R_S'=1 \times 10^{11} \Omega$, $R_S=9 \times 10^8 \Omega$, $C_S=8.25 \times 10^{-14}$ F). The data is compared with the conductance distribution obtained using the

constant bias STM BJ method (black curve). The conductance values are expressed in the units of the quantum conductance, $G_0 = 2e^2/h \approx 77 \mu\text{S}$ 34

Figure 3.1. Renderings for the four duplexes (A) DNA homoduplex, (B) DNA /aeg-PNA heteroduplex, (C) aeg-PNA homoduplex, and (D) γ -PNA homoduplex are shown. In each case the sequence is AGTTTGTACG. The insets show the chemical structures for the backbones of DNA, aeg-PNA, and γ -PNA..... 43

Figure 3.2. Chemical structure of the linkers that connect PNA to the Au surface. Panel A shows the propylthiol that is situated at the C end of the single stranded PNA. Panel B shows the thymidine 5-C2 amino linker which can be situated at any position in a single stranded PNA. .. 45

Figure 3.3. (A) The schematic for the single molecule conductance measurements. (B) Example current-time responses for the aeg-PNA homoduplex showing the triangular wave current response resulting from a molecular junction (i) and an ‘empty’ current response where a molecular junction does not occur (ii). For the current response showing the molecular junction, a clear transition occurs from the high conductance mode (H) to a lower conductance mode (M)..... 47

Figure 3.4. Panel A shows example current responses for the duplexes. The conductance histograms are shown for the DNA homoduplex (B), the aeg-PNA homoduplex (C), the DNA/aeg-PNA heteroduplex (D), and the γ -PNA homoduplex (E). The black curve is a fit of the histogram by a sum of two Gaussian functions. The peaks in the distributions are associated with major conductance modes, referred to as high and medium modes..... 49

Figure 3.5. The conductance histograms for the DNA homoduplex (gray) with amine linkers and PNA homoduplex (blue) with amine linkers. The peaks in the distributions correspond to major conductance modes; the overlaid black curves are fits to the histogram by a sum of Gaussian functions..... 52

Figure 3.6. The ratio of structural parameter fluctuations (standard deviation of 10,000 MD snapshots, averaged among the middle 6-mers) between different backbone species as compared to DNA. Structural parameters are defined and calculated with x3DNA⁶¹. The detailed information about the parameter means and standard deviations of all base pairs are shown in the Supporting Information. 57

Figure 4.1. The architectures of the full and nicked DNA homoduplexes and DNA/PNA heteroduplexes. The sequence of the top strand of each duplex is written in the 5'-to-3' direction for DNA and N-to-C direction for PNA. PNA strands (P) are shown in blue. DNA strands (D) are shown in black. 72

Figure 4.3. (A) Three pyrene labeling schemes for the duplexes. The red lines represent the 20-base DNA template strand. The blue and yellow lines represent the 10-base PNA strands. The blue ellipses represent the pyrenes. (B) The fluorescence spectra for pyrene-labelled DNA/PNA heteroduplexes. The solid, dotted, and dashed lines correspond to Schemes 1, 2, and 3, respectively. The data have been scaled to have equivalent intensity at $\lambda = 400$ nm..... 75

Figure 4.4. (A) An example current-time $I(t)$ trajectory of a full DNA molecular junction is shown (black) with the fitted current response overlaid (red). The STM tip retracts 0.2 \AA during each current response period. The inset shows the fitted conductance, $G(n)$, for each period in the current response. Conductance histograms are shown for the full DNA duplex (shaded cells) with the nicked analogue (unfilled cells) overlaid (B) and the full DNA/PNA duplex (shaded cells) with the nicked analogue (unfilled cells) overlaid (E). Three dimensional plots of conductance histograms for specific periods of the current responses are shown for all four duplexes (C), (D), (F), and (G). 79

Figure 4.5. Two-dimensional correlation plots for the full DNA (A), full DNA/PNA (D), and nicked duplexes (B) and (E). Each square represents the correlation between the conductance values for given periods n and k . By nature, the correlation has a value of one along the diagonal, when $n = k$. Panels C and F show the average ratio of the fitted conductance for period n to the fitted conductance for period 1. The total displacement over ten current response periods is 2 \AA 80

Figure 4.6. The conductance histograms for the full DNA/PNA heteroduplex (turquoise), the full PNA homoduplex (magenta), and the nicked PNA/PNA:DNA heteroduplex (blue). The black curves in each case are fits by a sum of two Gaussian functions. For the purposes of comparison, the height of the histogram for the full DNA/PNA heteroduplex is scaled by a factor of 0.3..... 82

Figure 4.7. Conductance values for DNA duplexes as a function of the A/T content of the duplex measured by various methods. In the conductance measurements, the DNA was attached to the surface by three-carbon (C3) thiol linkers. Squares identify the conductance measured by the scanning tunneling microscope break junction method. Triangles identify values measured by atomic force microscopy conductance utilizing a gold nanoparticle. The dashed line indicates the best fit function; and the shaded region shows a 95% confidence interval for the best fit..... 86

Figure 5.1. The opposing termini orientations are shown for N to N transport and C to C transport for $n = 3$. In both cases, the duplexes are anchored to the gold electrodes via amine modifications on the terminal thymine nucleobase. The arrows indicate the path of charge transport through the duplex via a hopping mechanism, including a cross-strand step at the center of the duplex. 94

Figure 5.2. Conductance histograms are shown for the N linker PNA for $n = 3-7$. The black curve overlaid is a fit to two Gaussian functions. The histograms shown are total counts after subtraction

of the background counts collected over the same number of experiments for each duplex (see Appendix D)..... 96

Figure 5.3. The results for the N linker PNA are presented with data for 3' linker DNA and 5' linker DNA from a previous study.²⁰ The open symbols are measurements performed to confirm the results taken from ref. 20. The smaller symbols are the medium modes observed for the N linker PNA. Error bars are shown for the duplexes studied here representing a single standard deviation of the fitted Gaussian function for the highest observable mode..... 97

Figure A.1. Current-time traces in the solvent regime recorded for mesitylene, 2,4-dichlorotoluene, and 3,4-dichlorotoluene at 0.5, 1, and 2 kHz frequency of the 0.3 ± 0.3 V bias modulation. 106

Figure A.2. Dependence of the solvents capacitance simulated using the model electrical circuit (Figure 4 in manuscript) on the bias modulation frequency. The error is estimated as 5%. The data is compared to the dielectric constant values adapted from refs 1 and 2..... 107

Figure A.3. Current-time traces recorded in air above the gold substrates with different geometrical surface areas. The traces were recorded at 0.5 kHz frequency of the 0.3 ± 0.3 V bias modulation. The STM tip – substrate separation was of about 300 μm 108

Figure A.4. Current-time traces recorded in the cell filed with different volumes of the 3,4-dichlorotoluene. The traces were recorded at 0.5 kHz frequency of the 0.3 ± 0.3 V bias modulation, with the STM tip – substrate separation of about 300 μm . Subsequent additions of the 0.25 mL of the solvent were made to cell. Note that first additions with total solvent volume below 0.75 mL were not sufficient to cover the surface of the gold substrate with solvent. 109

Figure A.5. The current-time traces recorded at different STM tip – substrate separations. The traces were recorded at 0.5 kHz frequency of the 0.3 ± 0.3 V bias modulation, in the cell filled

with 1 mL of 3,4-dichlorotoluene. Note that the separation is micrometers in length scale, thus a decrease in the current waveform amplitude originates from the decrease of the amount of the gold wire forming the tip that was immersed in the solvent. 109

Figure B.1. C-end (a) and N-end (b) thiol-modified PNA. The propylthiol is used to anchor the PNA to the Au surface is shown in red. 112

Figure B.2. N-end T_(C2-NH2) modified PNA. The thymidine 5-C2 amino linker is used to anchor the PNA to the gold surface is shown in blue. 112

Figure B.3. Loading of the 2-chlorotriptyl resin with the PT linker. 114

Figure B.4. S-alkylation of trityl mercaptan **1**. 115

Figure B.5. Synthesis of Thymidine 5-C2 Amino Linker. 116

Figure B.6. Current-distance trajectories for aeg-PNA/aeg-PNA duplexes with thiol linkers on the C end and N terminus. 122

Figure B.7. The aeg-PNA conductance histograms with three Gaussian fits (A) and two Gaussian fits (B). 124

Figure B.8. Nucleic acid sequence and numbering scheme for the couplings between nearest neighbor purine bases. 124

Figure B.9. The contact distance distributions for DNA/DNA (left), aeg-PNA/aeg-PNA (middle) and γ -PNA/ γ -PNA (right). 128

Figure B.10. Time evolution of the contact distance (left); A typical snapshot of the vDW contact between the S atom (colored in yellow) on the thiol linker (green) and the guanine (colored as atom type) (right). 129

Figure B.11. Contact distance distributions for amine modified DNA (top) and PNA (bottom). 129

Figure C.1. (A) The melting curves for the full DNA and nicked DNA. (B) The melting curves for the full DNA/PNA and nicked DNA/PNA. 134

Figure C.2. CD spectra of nicked PNA/PNA:DNA and DNA duplexes. Samples containing stoichiometric amounts of oligonucleotides at 3 μ M strand concentration were prepared in 10 mM sodium phosphate buffer. 135

Figure C.3. The conductance histograms for the full and nicked versions of the DNA/DNA and DNA/PNA duplexes. The Gaussian fits are shown as overlaid black curves. 137

Figure C.4. Conductance histograms for the nicked PNA/PNA:DNA heteroduplex with the thiol linker on the DNA 10-mer (black), and with the thiol linker on the PNA 10-mer (blue). 138

Figure C.5. A current-time, $I(t)$, trajectory showing the method of solvent removal and period concatenation. The set-point of the conductance measurements is shown as a red, dashed line. The red, shaded region depicts the periods of the current response that are within the solvent threshold and are filtered out of the correlation analysis. 140

Figure C.6. Serial correlation is shown for the full and nicked versions of the DNA and DNA/PNA duplexes using the ‘frozen junction’ method. 141

Figure C.7. Conductance values for DNA duplexes as a function of the total number of base pairs of the duplex measured by various methods. In the conductance measurements, the DNA was attached to the surface by three-carbon (C3) thiol linkers. Squares identify the conductance measured by the scanning tunneling microscope break junction method. Triangles identify values measured by atomic force microscopy conductance utilizing a gold nanoparticle. The dashed line indicates the best fit function shown in Figure 7; and the shaded region shows a 95% confidence interval for the best fit. 142

Figure D.1. The results of the control study are shown for the number of experiments performed using PNA duplexes. The number of modulation periods is considerably less than those for each PNA duplex..... 144

Figure D.2. A comparison of the modulation periods observed for an unmodified substrate and a substrate that has undergone electrochemical oxidation. An equivalent number of trajectories was collected for both substrates..... 145

Figure E.1. The image shows the Teflon cell, which holds the substrates used for the break junction experiments. 146

Figure E.2. The image shows the disassembled stage excluding the clip assembly..... 147

Figure E.3. The completely assembled stage including the Teflon cell is shown here. 147

Figure E.4. The scanner with a gold tip inserted into the preamplifier tube is shown here. 148

Figure E.5. The function generator (SRS Model DS345) used to apply the externally modulated bias is shown. 148

Figure E.6. The breakout box for the Agilent 5500 SPM system is shown. The incoming coaxial cable from the function generator is split and enters the breakout box in the “Bias In” port and the “Friction” port. For each port, there is an on/off switch; the position of the switch shown here corresponds to “off” position for both ports. 149

Figure E.7. The image shows the PicoView interface displaying the data panels including currents vs. distance and friction vs. distance measurements..... 150

Figure E.8. Shown here is the Simulink module used to create the sample current responses. The circuit components shown in blue correspond to the solvent current and the circuit component shown in red is the molecular resistance that is varied to generate the library..... 153

LIST OF EQUATIONS

Equation 1.1	6
Equation 1.2	7
Equation 2.1	37
Equation 3.1	55
Equation C.1	139

LIST OF SCHEMES

Scheme 3.1. (i) K_2CO_3 , DMF, α -bromo ethyl acetate, DMF, 0°C to room temperature, 24 h, quantitative yield; (ii) $Pd(OAc)_2$, Bu_4NBr , DMF/DIE/ H_2O , acrylic acid, 80-90°C, 16h, 60%; (iii) $BocNH(CH_2)_2NH_2.HCl$, HATU, DIEA, DMF, 0 °C to room temperature, 12 h; (iv) LiOH, THF, 0°C to rt, 12 h, 75%..... 60

Scheme 3.2. Synthesis of γ -serine modified PNA monomers (i) NMM, $ClCO_2i-Bu$, DME, $NaBH_4$, quantitative Yield (ii) DMSO, $(COCl)_2$, Et_3N , DCM, N_2 , -78°C, % 95 (iii) ethyl ester glycine, MeOH, 4 °C, 4 h, then AcOH, $NaBH(OAC)_3$, 30 min., % 40, (iv) carboxymethylnucleobase (B: A, G, C, T), DCC, DhbtOH, DMF, 40°C, 24 h, %39-63 (v) NaOH/THF (1:1), 30 min., 0°C. %76-96. 61

PREFACE

I have been helped by so many people during my time here at Pitt. There are many people that I am very grateful to have had in my life that I do not mention by name here. I hope they know that I truly appreciate their contribution to this endeavor and that they were instrumental in my success.

Firstly, I would like to thank my boss, Dr. Waldeck. He was willing to take me on and guide me, with great patience, through my course as a ‘gradual student’. I have grown tremendously as a thinker, a writer, and a scientist during my time in his group. The Waldeck group is doing exciting and impactful science, and his brilliance and leadership is clearly responsible. He may have only let me stick around because I made a solid pot of coffee, but I am indebted regardless.

I must also thank the members of my committee, Dr. Amemiya, Dr. Garrett-Roe, and Dr. Achim for their expertise and insightful recommendations. Of course, I need to also recognize the several fruitful collaborations with Dr. Achim and Dr. Beratan and their great students, without whom I would have been unable to complete this work.

To the members of the Waldeck group, both past and present, I owe enormous gratitude. They are all extremely intelligent and competent and it has been an absolute pleasure working with them. I would like to single out Dr. Emil Wierzbinski and Dr. Brian Bloom. Emil took me under his wing, albeit begrudgingly, and taught me how to be a capable researcher. His proficiency and knowledge of our field was indispensable to my development. Brian, in much the same way, was an endless source of information and advice.

I would also like to thank my friends and family. There are not many people that can experience lasting friendships from early childhood into their professional lives, but we have all

maintained our closeness over the years and enjoyed each other's many accomplishments. I should also thank Nan, Aunt Sharon, and Uncle Terry for being a part of my life and encouraging me during this time.

Thank you to my sister, Emily. She is remarkable, like our mother was, and I have no doubt that she will continue to be incredibly successful in all of her pursuits. Thank you to Caitlyn. She is beautiful and brilliant, and she *lights* up my life. Finally, and most importantly, I would like to thank my father. Nobody in my life has been in my corner more and encouraged me with a greater passion. I am proud to be his son and the strength and loyalty that I have, I owe to him.

1.0 INTRODUCTION

1.1 INTRODUCTION TO MOLECULAR ELECTRONICS

The pursuit of the continuing miniaturization of electronics and the integrated circuits that compose them is forcing researchers to explore increasingly small dimensions, turning to individual molecules as candidates to perform complex electrical functionalities.¹ The use of single molecules as circuit components was first theorized by Ratner and Aviram in 1974;² and the field of molecular electronics has progressed rapidly from this inception.³ However, considerable research continues to be devoted to understanding how charges are mediated by single molecules and the implications of this behavior on future molecular devices.⁴ As the means for studying the electrical properties of single molecules have become more effective and reproducible, attention has been directed to elucidating the underlying mechanisms and fundamental factors that undergird nanoscale charge transfer. This chapter will highlight the development of the molecular electronics field and provide the necessary background for the subsequent chapters exploring experiments in single molecule conductance.

1.2 PRELIMINARY STUDIES IN SINGLE MOLECULE CONDUCTANCE

While the idea of using single molecules as circuit components had been several decades old, a major breakthrough in the measurement of single molecule conductance came with the application of the break junction technique to study molecular conductance in 1997.⁵ In this technique, a notched, gold wire, in the presence of dithiolated molecules, was stretched by piezo control until the wire fractured. The two ends were then brought together until a nonnegligible conductance was observed. This conductance was attributed to molecules bridging the gap formed when the gold wire fractured, exploiting the affinity of sulfur and gold to form a molecular junction.⁶ This method was indeed pioneering; however, the technique did not show reproducible

current amplitudes because a consistent number of molecules could not be trapped in the junctions. This emphasized the need for a technique that allows for the formation of only a single molecular junction and discourages the formation of simultaneous molecular junctions.

This led to the incorporation of scanning probe methods for the formation of single molecular junctions, revolutionizing the molecular electronics field. In 2001, an atomic force microscope (AFM) was used to probe individual molecules on a gold substrate, in a variation of host/guest or matrix isolation chemistry.⁷ Dithiolated molecules were allowed to exchange briefly with a monolayer of singly-thiolated molecules, resulting in a diffuse coverage of isolated dithiolated molecules. The matrix-isolated molecules were then exposed to gold nanoparticles (Au NPs), which anchored themselves to the exposed thiols. With an AFM tip, the individual Au NPs could be probed and the conductance through individual molecules could be measured. This method provided much more reproducible molecular junctions; however, there were discrepancies between the measured conductance values and those predicted by theory.⁸ It was concluded that the matrix isolation method, while demonstrating the first instance of single molecular junctions, was harmed by the presence of the organic ligands passivating the surface of the Au NPs, complicating the observed current responses and subsequent analysis.⁹

In 2003, Xu and Tao demonstrated the scanning tunneling microscope-based break junction technique (STM-BJ), ultimately becoming the most widely used method for measuring single molecule conductance (see Figure 1.1).¹⁰ Here, an STM tip is driven to the surface of a conductive substrate (typically gold) on which there is a diffuse monolayer of dithiolated molecules. When the tip is in contact with the metal substrate, the current saturates at a current level dictated by the acting preamplifier. By withdrawing the STM tip, molecules can be trapped to form molecular junctions between the substrate and the tip. As the tip is retracting, the current

displays an exponential decay from the saturation limit; however, if there is a molecular junction formed, the current displays a weaker distance dependence, as the current between the substrate and tip is dictated by the conductance through the molecular junction. The weaker distance dependence results in a current plateau in the current response. When the molecular junction is eventually broken, the current continues to decay to a baseline value. The current axis can be binned and the data points in the current response can be compiled to provide a histogram showing the most probable conductance of the measured molecule. The capability of rapid data collection and the elimination of the ambiguities in the aforementioned strategies solidified the STM-BJ technique as the foremost protocol for single molecule conductance measurements.

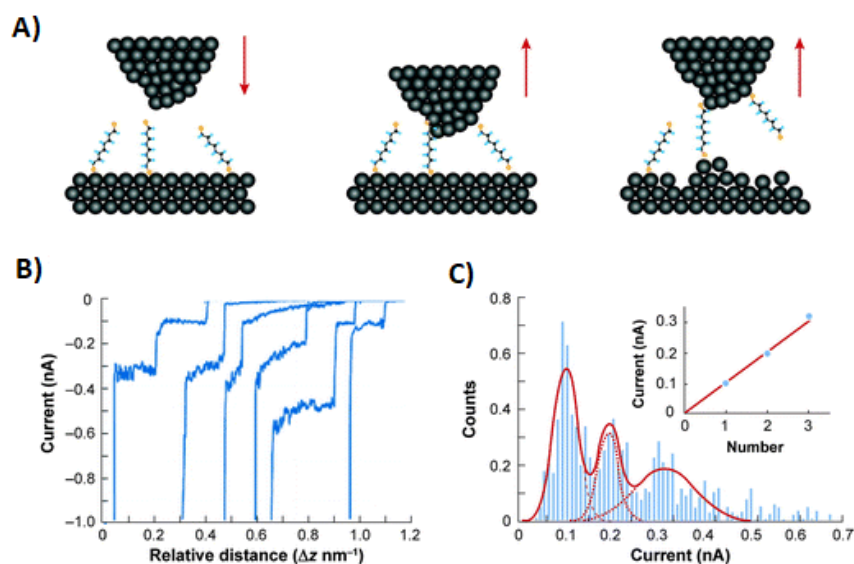


Figure 1.1. A) The STM-BJ technique is demonstrated. The black spheres are gold atoms and the linkers are shown as yellow spheres on the molecular termini. B) The current responses for the STM-BJ technique show current plateaus corresponding to molecular junctions during the tip retraction process. C) A current histogram is shown to demonstrate how the current responses are compiled to reflect the most probable molecular conductance. (Taken from Ref. 9)

1.3 BIOMOLECULES AS CANDIDATES FOR MOLECULAR ELECTRONICS

The concept to explore the use of biomolecules as components in molecular electronics stems from their profound ability to transfer charge over large distances and with spectacular

efficiency in biological processes.¹¹ While the majority of nature's charge transfer occurs through proteins,¹² their unsurpassed programmability¹³⁻¹⁴ has made nucleic acids alluring candidates as motifs for bioelectronic platforms. Not long after the discovery of the structure of DNA in 1953,¹⁵ the research community was contemplating charge transfer through nucleic acid duplexes and attempting to reveal its fundamental mechanisms.¹⁶ It was even suggested that the structure of DNA and the long-range conjugation could allow for ballistic-like transport over large distances.¹⁷ The conductance of single nucleic acid duplexes would become the subject of numerous experiments in the following decades.

1.3.1 Preliminary Studies in DNA Conductance

Pursuing the intriguing and advantageous qualities of DNA, researchers sought to reveal whether DNA behaved as an insulator or a conductor. Preliminary studies achieved conduction through DNA molecules; however, the techniques used measured many duplexes and the conclusions were not in agreement.¹⁸⁻¹⁹ Later experiments succeeded in measuring the conductance of single DNA molecules; although these works did not employ the STM-BJ technique, and subsequently suffered from a lack of agreement and statistical robustness.²⁰⁻²³ It was not until 2004 that single DNA duplexes were measured in aqueous conditions and to a high statistical degree using the STM-BJ method.²⁴ In this study, the conductance of two families of duplexes were investigated. The first family included duplexes of alternating guanine (G) and cytosine (C) nucleobases. For these duplexes, the molecular conductance was observed to decrease linearly with an increase in the duplex length. The second family involved introducing adenine (A) and thymine (T) base pairs (bps) into the duplex. The conductance for this family of duplexes decreased exponentially with increasing duplex length, suggesting that the prevailing charge transfer mechanism is dependent on the sequence of the duplex (see Figure 1.2). Other conductance

versus length analyses have indicated that the effective length of a DNA duplex is solely the number of AT bps.²⁵ This work highlighted the need for a thorough understanding of the charge transfer mechanism on the nanoscale and how they manifest in single molecule conductance measurements.

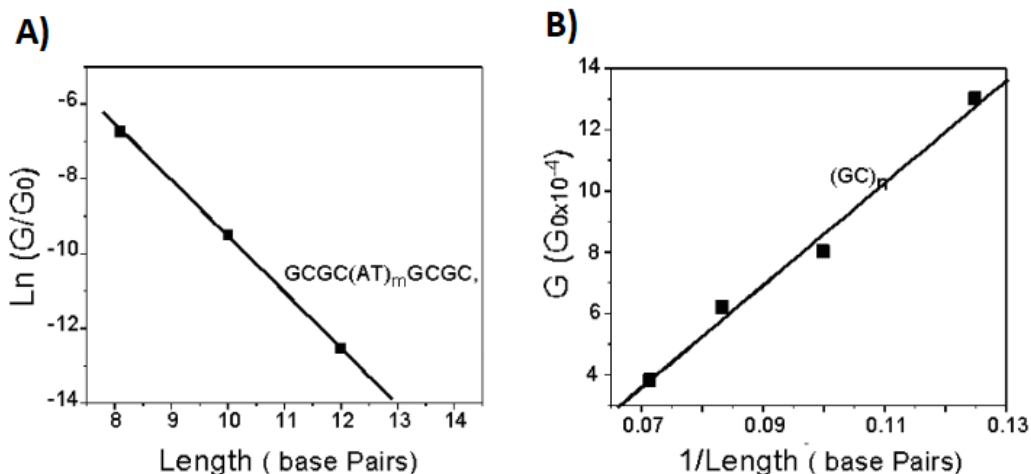


Figure 1.2. The length dependence of the single molecular conductance is shown for two different families of DNA duplexes. An exponential dependence is shown for sequences containing AT pairs (A) and an inversely proportional dependence is observed for sequences with only GC pairs.

1.4 MECHANISMS OF CHARGE TRANSFER

Under the extensive canopy of charge transfer mechanisms and processes, all theoretical models fall between the extremes of completely coherent and completely incoherent transfer.²⁶ Because of the exceeding complexity of nanoscale charge transfer and the numerous factors that affect single molecule conductance, there has been a tremendous effort both experimentally and theoretically to reconcile the proposed models and develop a framework that explains the many conflicting observations.²⁷ The most prominent mechanisms evoked to explain these experiments are coherent tunneling and incoherent charge hopping.

1.4.1 Coherent Tunneling

Quantum mechanical tunneling is a classically-forbidden phenomenon where the energy barrier of the bridge state(s) between a donor and acceptor is greater than the energies of the donor and acceptor, themselves. In this instance, an electron can ‘tunnel’ through the energy barrier in a coherent manner.²⁸ The tunneling probability has an exponential dependence on the length of the barrier between the donor and acceptor:

$$G \propto e^{-\beta L} \qquad \text{Equation 1.1}$$

where G is the transmission probability, or conductance, β is the decay constant, and L is the barrier length. For the case of DNA, this is taken to be the length of the duplex.²⁹ Because the occurrence of tunneling is predicated on a large barrier height relative to the energies of the donor and acceptor, this mechanism accurately predicts the conductance of alkane chains, where the energy gap between the highest occupied molecular orbital (HOMO) and lowest unoccupied molecular orbital (LUMO) is large.¹⁰ It is therefore clear that the accuracy of the tunneling model in predicting the charge transfer in DNA will be dependent on the energies of the nucleobases. If the energies do not result in a sufficiently high tunneling barrier, other mechanisms become possible as well, a possible explanation for the linear length dependence observed in the alternating GC sequence DNA in the 2004 study.²⁴

1.4.2 Incoherent Charge Hopping

In the event that molecular orbital energies do not provide a large energy barrier, an incoherent transfer mechanism becomes possible.³⁰ Rather than transport through a barrier, as observed in quantum tunneling, charge hopping involves movement over a barrier. Thus, one can intuit that the transport will be extremely sensitive to thermal effects. Indeed, the conductance can be described in a manner that is dependent on an Arrhenius factor:

$$G \propto \frac{e^{-\Delta E/k_B T}}{L} \quad \text{Equation 1.2}$$

where ΔE is the difference in energy between hopping sites, k_B is Boltzmann's constant, and T is the temperature. Note that, using this model, charge hopping is inversely proportional to the distance between hopping sites. It is also important to observe that coherent tunneling should not depend on temperature, theoretically, while incoherent hopping is thermally-activated.³¹ It is for this reason that experimental endeavors have been sought to determine the identity of the principal mechanism by means of temperature-dependent studies.³²⁻³⁴

The length-dependence of the single molecule conductance for DNA duplexes is shown to transition from an exponential dependence at short lengths to an inversely proportional dependence around 30 Å.³⁵⁻³⁶ This can be rationalized because, at short distances, a coherent mechanism is efficient; however, the efficiency of the tunneling decays exponentially and gives way to the hopping mechanism, with a much weaker distance dependence.

1.4.3 Flickering Resonance

The observation that, for short DNA duplexes, the combined charge carrier populations of the donor and acceptor sites do not reflect the total charge populations has led to the conception of the flickering resonance mechanism.³⁷ In this model, the base pairs function as sites where charges are able to localize. When sites become energetically degenerate, electrons move via the conjugated base stack in a coherent, pseudo-ballistic manner. Because electronic degeneracy is required for transport, the transmission probability is strongly dependent on the structural fluctuations of the molecule and its coupling to the solvent medium. The probability that an electron will traverse the length of a duplex is a product of the individual energy matching probabilities. This results in an exponential dependence with length, mimicking the dependence for the tunneling model.

1.4.4 Interplay of Charge Transfer Mechanisms

The emergence and interplay of the various charge transfer mechanisms is dictated by the energy of the molecular orbitals of the bridging molecule relative to the electrode Fermi levels and the overlap of adjacent molecular orbitals. For alkanedithiol molecular junctions, nonbonding molecular orbitals are situated at energies well above the Fermi level of gold.³⁸ In this case, the molecular orbitals where electrons can localize are positioned beyond the extent that thermal fluctuations of the orbital energies can reach. Thus, the electron hopping pathway is excluded, as electrons do not have the ability to overcome the barrier height and occupy the bridge states.³⁰ In contrast, the frontier molecular orbitals of nucleic acid duplexes are positioned at energies much closer to the Fermi level of the electrodes.³⁹ Because the position of the molecular orbital energies for nucleic acid duplexes are within thermal fluctuations of the Fermi level of the electrodes, mechanisms can manifest that involve occupation of the molecular orbitals of the bridging molecule.

With the energies of the molecular orbitals for nucleic acid duplexes falling near the Fermi level of the electrodes, competing charge transfer mechanisms arise. In addition to coherent tunneling and incoherent charge hopping,^{28, 30} flickering resonance, as a charge transfer pathway, becomes viable because the molecular orbital energies may become energetically degenerate.³⁷ This occurrence is contingent on the average energy and energy level width of the bridge orbitals with respect to the Fermi level of the electrodes and between molecular orbitals. The coexistence of these charge transfer mechanisms complicates the ability to predict long-range conductance of nucleic acid duplexes and emphasizes the subtle effects that will influence which mechanism dominates in these systems.⁴⁰

In addition to the energies of the frontier orbitals, electronic couplings of the molecular orbitals are also dependent on orbital overlap.⁴¹ The ability of adjacent orbitals to overlap relies on their spatial proximity. The strong influence of proximity on orbital overlap makes flexibility of the molecular junction a significant factor in the charge transfer ability.⁴² Because structural fluctuations have a considerable impact on electronic couplings,⁴³ the role of temperature and solvent interactions as a modulator of molecular conformation becomes substantial. In the same manner as the absolute energies of the molecular orbitals, the positions of the molecular orbitals, and the consequent orbital overlap, dictate the electronic couplings between frontier orbitals and the electron transfer ability of the molecular junction. The contributions of these two factors balance the interplay of the competing charge transfer mechanisms.

1.5 MOLECULAR LINKERS

The single molecule conductance measurements that followed the development of the STM-BJ technique initially displayed greatly differing results.⁴⁴⁻⁴⁶ Experimental values were orders of magnitude different between publications and theoretical studies.⁴⁷ It was ultimately determined that modeling individual molecules as resistors is too simple; the conductance of single molecules can have multiple values, or ‘modes’. This realization resulted in numerous ensuing investigations that revealed the tremendous impact that the linkers connecting the molecular bridge to the electrodes have on the measured single molecule conductance.⁹

1.5.1 Conductance Modes

The lack of agreement between early experiments in single molecule conductance served as the impetus for an elucidating study utilizing a logarithmic preamplifier.⁴⁸ The logarithmic preamplifier allowed for a large current response range, monitoring several orders of magnitude in conductance. The results of this experiment reconciled the previous findings and showed that

single molecule junctions can display multiple conductance modes. The origin of these modes was hypothesized to arise from differing linker-electrode geometries.⁴⁹ This hypothesis was supported by computational studies revealing the nature of the covalent linkage between thiols and Au surfaces.⁵⁰⁻⁵¹ The modes observed were assigned as ‘high’, ‘medium’, and ‘low’, with the observance of the modes dependent on the technique used to measure the single molecule conductance.⁵² The ability of the STM-BJ technique to access all of the conductance modes accompanied the other factors that made it become the most prominent technique for conductance measurements.

1.5.2 Backbone Linkers

The profound effect that the thiol linkers had on the measured conductance led to subsequent studies exploring alternative molecular linkers.⁵³⁻⁵⁶ A comparative study of thiol-, amine-, and carboxylic acid-terminated molecules indicated that amine and carboxylic acid contacts are viable terminal groups for single-molecule conductance measurements; however, the anchoring groups led to different contact resistances, presumably because of differing electronic coupling.⁵⁴ It was shown that the contact resistance varied in the order of Au-COOH > Au-NH₂ > Au-S, indicating that thiol-terminated molecules are the most ideal for minimizing the contact contribution to the measured conductance. Amine and carboxylic acid anchoring groups also suffered from a dependence on pH, with the protonation of each at low pH decreasing the binding affinity. Despite these considerations, amine anchoring groups gave rise to less variability in conductance measurements, as concluded from the broadness in the current histograms.⁵⁶ This well-defined molecular conductance was speculated to be a result of isotropy in the N lone pair coupling to the electrodes leading to fewer conformation variations, and consequently, a more consistent single-molecule conductance value.

1.5.3 Base Stack Linkers

For the specific application of nucleic acids, amine linkers were used to link the base stack of the nucleic acid duplex directly to Au electrodes (see Figure 1.3).⁵⁷ The amine linker arose from previous studies that aimed to address the breakdown mechanism in DNA single molecule junctions.⁵⁸⁻⁶⁰ It was shown that when the molecular linkers provide a linkage directly to the base stack of DNA, the single molecule conductance is much greater than that for backbone linkers. The increase in the molecular conductance was rationalized by acknowledging that the base stack linkers allow the electron to inject into the base stack much more effectively than do the backbone linkers.

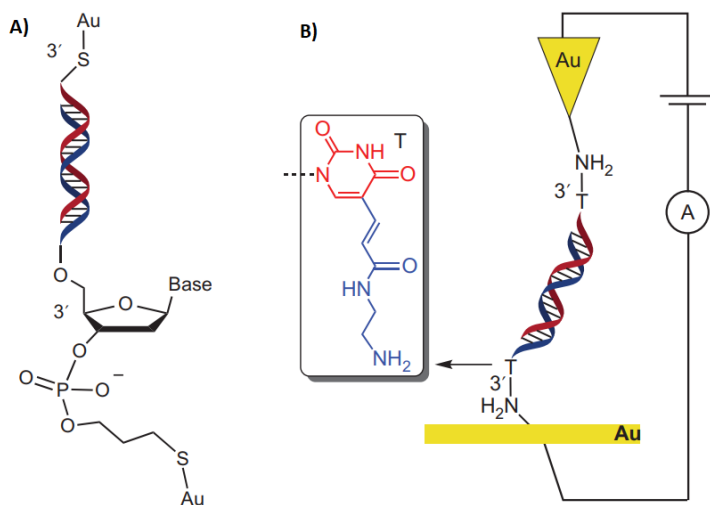


Figure 1.3. A) The structure of the thiol, backbone linkers are shown for DNA molecular junctions. B) The base stack linker (blue) is shown as a thymine (red) modification as a linkage between the Au electrodes. (Taken from Ref. 57)

1.6 ELECTROCHEMICAL CHARGE TRANSFER RATE AND CONDUCTANCE

Early attempts to understand the relationship between the electrochemical charge transfer rate and the molecular conductance of single molecules predicted a linear relationship for both tunneling and charge hopping mechanisms.⁶¹⁻⁶⁴ Future experimental studies were able to shed light

on this topic.⁶⁵⁻⁶⁶ Ultimately, it was determined that the electrochemical rate constant and single molecule conductance are related by a power law, with the empirical power depending on the molecular bridge (see Figure 1.4).⁶⁶ It is under this framework that comparisons between electrochemical studies and single molecule conductance measurements can be drawn and the conclusions reached for molecular systems in single-electrode, electrochemical contexts can be extrapolated to experimental conditions with two electrodes.

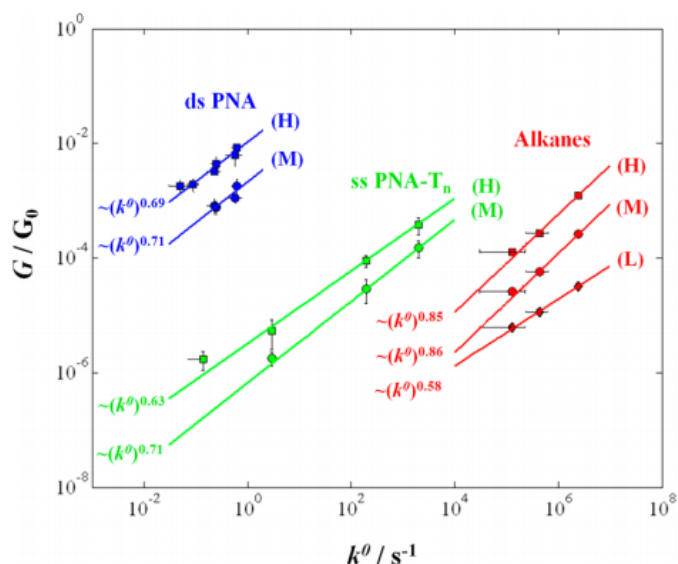


Figure 1.4. The single-molecule conductance versus the electrochemical charge transfer rate constant is shown for alkanes (red), single strand PNA constructed of thymine nucleotides (green), and double stranded PNAs (blue).

Of particular importance to understanding how electron transfer proceeds is the role of flexibility in charge transport. It was hypothesized that conductance in DNA duplexes was strongly dependent on the well-coupled arrangement of the nucleobases, with the movement of the bases having a tremendous impact on the single molecular conductance.³² This supposition was tested in subsequent electrochemical studies.⁶⁷⁻⁶⁹ It was shown that a greater degree of flexibility resulted in a larger electrochemical rate constant because the nucleobases could more frequently fluctuate in conformation to reach arrangements that increased couplings in the more flexible systems.

Further electrochemical studies attempted to address the manner in which electrons traverse nucleic acid duplexes by introducing ‘nicked’ duplexes.⁷⁰⁻⁷¹ In these systems, the duplexes are hybridized such that the backbone is broken, while the nucleobase stack is unaffected. It was shown that the electrochemical rate constant was not affected as long as the base stack was not affected, regardless of the number of nicks in the nucleic acid backbone; however, the electrochemical rate constant decreased considerably when the base stack was compromised. The conclusion was that charges move through the duplex base stack rather than along the nucleic acid backbone.⁷¹ Understanding how these observations in an electrochemical setting are affected by the geometry of the STM-BJ protocol represent important challenges in understanding single molecule conductance.

1.7 DISSERTATION OUTLINE

Following the pioneering experiments that have formed the foundation of the single molecule conductance field, experiments have now turned towards understanding the subtle effects that deviate from classical phenomena. The role of orbital position, molecular conformation, structural fluctuations, etc. in charge transfer on the nanoscale is being explored. These fundamental insights will pave the way for assemblies of complex molecular scaffolds that act as a functional bioelectronic platform. The work presented in this dissertation seeks to address central questions in the single molecule conductance field and build upon the base of knowledge pursuing the realization of molecular electronics.

Chapter 2 presents a protocol for the measurement of single molecule conductance involving a modification of the STM-BJ technique. Rather than utilizing a constant bias, this protocol applies a modulated bias across the STM tip and substrate. This produces modulated current responses corresponding to molecular junctions rather than the current plateaus observed

in the traditional STM-BJ method. The modulated bias method shows increased sampling at low conductance values and it offers the ability to easily partition the current response for intricate statistical analyses.

Chapter 3 reports the use of the modulated bias method to study the effects of flexibility on the molecular conductance of nucleic acid duplexes. A series of duplexes of the same length and sequence, but with varying degrees of backbone rigidity, are compared. The single molecule conductance is observed to be larger for the more flexible duplexes. A computational investigation is employed to understand which structural parameters are susceptible to conformational fluctuations and to shed light on their relative effect on the conductance.

Chapter 4 compares the conductance of duplexes with two strands of the same length with duplexes formed from smaller strands hybridized with a longer, template strand. This creates a ‘nick’ in the backbone of the latter duplex. These nicked duplexes are shown to have an equivalent average molecular conductance to the full duplexes; however, the nicked duplexes display an increased variability within a current response and suffer from a lowered duplex stability. There is also a presentation of DNA conductance from literature that treats the length as determined solely by the number of AT bps.

Chapter 5 builds upon previous studies on DNA conductance that investigated the interplay between coherent and incoherent charge transfer mechanisms. The single molecule conductance of a family of PNA molecules is measured to determine whether flexibility affects the relationship between electron delocalization and cross-strand charge hopping in the system of nucleic acid duplexes. The more flexible PNA is shown to dampen the oscillatory nature of the conductance with respect to increasing chain length, suggesting that the coherent contribution to the charge transfer mechanism is dominated by the cross-strand charge hopping event.

1.8 REFERENCES

1. Moore, G. E., Cramming More Components onto Integrated Circuits. *Electronics* **1965**, 38.
2. Aviram, A.; Ratner, M. A., Molecular Rectifiers. *Chem. Phys. Lett.* **1974**, 29, 277-283.
3. Baldea, I., *Molecular Electronics: An Experimental and Theoretical Approach*; Pan Stanford, 2016.
4. Karthäuser, S., Control of Molecule-Based Transport for Future Molecular Devices. *J. Phys. Condens. Matter* **2011**, 23, 013001.
5. Reed, M. A.; Zhou, C., Conductance of a Molecular Junction. *Science* **1997**, 278, 252-254.
6. Pensa, E.; Cortés, E.; Corthey, G.; Carro, P.; Vericat, C.; Fonticelli, M. H.; Benítez, G.; Rubert, A. A.; Salvarezza, R. C., The Chemistry of the Sulfur–Gold Interface: In Search of a Unified Model. *Acc. Chem. Res.* **2012**, 45, 1183-1192.
7. Cui, X. D.; Primak, A.; Zarate, X.; Tomfohr, J.; Sankey, O. F.; Moore, A. L.; Moore, T. A.; Gust, D.; Harris, G.; Lindsay, S. M., Reproducible Measurement of Single-Molecule Conductivity. *Science* **2001**, 294, 571-574.
8. Di Ventra, M.; Pantelides, S. T.; Lang, N. D., First-Principles Calculation of Transport Properties of a Molecular Device. *Phys. Rev. Lett.* **2000**, 84, 979-982.
9. Chen, F.; Hihath, J.; Huang, Z.; Li, X.; Tao, N. J., Measurement of Single-Molecule Conductance. *Annu. Rev. Phys. Chem.* **2007**, 58, 535-564.
10. Xu, B.; Tao, N. J., Measurement of Single-Molecule Resistance by Repeated Formation of Molecular Junctions. *Science (Washington, DC, U. S.)* **2003**, 301, 1221-1223.
11. Giese, B.; Graber, M.; Cordes, M., Electron Transfer in Peptides and Proteins. *Curr. Opin. Chem. Biol.* **2008**, 12, 755-759.
12. Gray, H. B.; Winkler, J. R., Electron Tunneling through Proteins. *Q. Rev. Biophys.* **2003**, 36, 341-372.
13. Topping, T.; Voigt, N. V.; Nangreave, J.; Yan, H.; Gothelf, K. V., DNA Origami: A Quantum Leap for Self-Assembly of Complex Structures. *Chem. Soc. Rev.* **2011**, 40, 5636-5646.
14. Adleman, L., Molecular Computation of Solutions to Combinatorial Problems. *Science* **1994**, 266, 1021-1024.
15. Watson, J. D.; Crick, F. H., Molecular Structure of Nucleic Acids; a Structure for Deoxyribose Nucleic Acid. *Nature* **1953**, 171, 737-8.
16. Eley, D. D.; Spivey, D. I., Semiconductivity of Organic Substances. Part 9.-Nucleic Acid in the Dry State. *Trans. Faraday Soc.* **1962**, 58, 411-415.
17. Murphy, C. J.; Arkin, M. R.; Jenkins, Y.; Ghatlia, N. D.; Bossmann, S. H.; Turro, N. J.; Barton, J. K., Long-Range Photoinduced Electron Transfer through a DNA Helix. *Science* **1993**, 262, 1025-1029.
18. Braun, E.; Eichen, Y.; Sivan, U.; Ben-Yoseph, G., DNA-Templated Assembly and Electrode Attachment of a Conducting Silver Wire. *Nature* **1998**, 391, 775.
19. Fink, H.-W.; Schönberger, C., Electrical Conduction through DNA Molecules. *Nature* **1999**, 398, 407.
20. Porath, D.; Bezryadin, A.; de Vries, S.; Dekker, C., Direct Measurement of Electrical Transport through DNA Molecules. *Nature* **2000**, 403, 635.

21. Storm, A. J.; Noort, J. v.; Vries, S. d.; Dekker, C., Insulating Behavior for DNA Molecules between Nanoelectrodes at the 100 Nm Length Scale. *Appl. Phys. Lett.* **2001**, *79*, 3881-3883.
22. Yoo, K. H.; Ha, D. H.; Lee, J. O.; Park, J. W.; Kim, J.; Kim, J. J.; Lee, H. Y.; Kawai, T.; Choi, H. Y., Electrical Conduction through Poly(Da)-Poly(Dt) and Poly(Dg)-Poly(Dc) DNA Molecules. *Phys. Rev. Lett.* **2001**, *87*, 198102.
23. Shigematsu, T.; Shimotani, K.; Manabe, C.; Watanabe, H.; Shimizu, M., Transport Properties of Carrier-Injected DNA. *J. Chem. Phys.* **2003**, *118*, 4245-4252.
24. Xu, B. Q.; Zhang, P. M.; Li, X. L.; Tao, N. J., Direct Conductance Measurement of Single DNA Molecules in Aqueous Solution. *Nano Lett.* **2004**, *4*, 1105-1108.
25. Beall, E.; Sargun, A.; Ulku, S.; Bae, Y.; Wierzbinski, E.; Clever, C.; Waldeck, D. H.; Achim, C., Molecular Conductance of Nicked Nucleic Acid Duplexes. *J. Phys. Chem. C* **2018**, *122*, 7533-7540.
26. Yin, X.; Waldeck, D. H., Electron Transfer: Basic Theory, Experiments and Computational Methods. *Adv. Sci. Eng. Med.* **2015**, *7*, 1093-1111.
27. Venkatramani, R.; Keinan, S.; Balaeff, A.; Beratan, D. N., Nucleic Acid Charge Transfer: Black, White and Gray. *Coord. Chem. Rev.* **2011**, *255*, 635-648.
28. Kuhn, H.; Försterling, H. D.; Waldeck, D. H., *Principles of Physical Chemistry*; Wiley, 2009.
29. Priyadarshy, S.; Risser, S. M.; Beratan, D. N., DNA Is Not a Molecular Wire: Protein-Like Electron-Transfer Predicted for an Extended Π -Electron System. *J. Phys. Chem.* **1996**, *100*, 17678-17682.
30. Marcus, R. A., Electron Transfer Reactions in Chemistry: Theory and Experiment (Nobel Lecture). *Angew. Chem. Int. Ed. Engl.* **1993**, *32*, 1111-1121.
31. Bixon, M.; Jortner, J., Charge Transport in DNA Via Thermally Induced Hopping. *J. Am. Chem. Soc.* **2001**, *123*, 12556-67.
32. O'Neill, M. A.; Becker, H. C.; Wan, C.; Barton, J. K.; Zewail, A. H., Ultrafast Dynamics in DNA-Mediated Electron Transfer: Base Gating and the Role of Temperature. *Angew. Chem. Int. Ed. Engl.* **2003**, *42*, 5896-900.
33. Yun, Y. J.; Park, G.; Jung, S.; Ha, D. H., Anomalous Temperature Dependence of Electrical Conductance of DNA-Linked Au Nanoparticle Aggregates. *Appl. Phys. Lett.* **2006**, *88*, 063902.
34. Zalinge, H. v.; Schiffrin, D. J.; Bates, A. D.; Starikov, E. B.; Wenzel, W.; Nichols, R. J., Variable-Temperature Measurements of the Single-Molecule Conductance of Double-Stranded DNA. *Angew. Chem. Int. Ed.* **2006**, *45*, 5499-5502.
35. Berlin, Y. A.; Burin, A. L.; Ratner, M. A., Elementary Steps for Charge Transport in DNA: Thermal Activation Vs. Tunneling. *Chem. Phys.* **2002**, *275*, 61-74.
36. Lu, Q.; Liu, K.; Zhang, H.; Du, Z.; Wang, X.; Wang, F., From Tunneling to Hopping: A Comprehensive Investigation of Charge Transport Mechanism in Molecular Junctions Based on Oligo(P-Phenylene Ethynylene)S. *ACS Nano* **2009**, *3*, 3861-8.
37. Zhang, Y.; Liu, C.; Balaeff, A.; Skourtis, S. S.; Beratan, D. N., Biological Charge Transfer Via Flickering Resonance. *Proc. Natl. Acad. Sci. U.S.A.* **2014**, *111*, 10049-10054.
38. Akkerman, H. B.; Naber, R. C. G.; Jongbloed, B.; van Hal, P. A.; Blom, P. W. M.; de Leeuw, D. M.; de Boer, B., Electron Tunneling through Alkanedithiol Self-Assembled

- Monolayers in Large-Area Molecular Junctions. *Proc. Natl. Acad. Sci.* **2007**, *104*, 11161-11166.
39. Staykov, A.; Tsuji, Y.; Yoshizawa, K., Conductance through Short DNA Molecules. *J. Phys. Chem. C* **2011**, *115*, 3481-3490.
 40. Risser, S. M.; Beratan, D. N.; Meade, T. J., Electron Transfer in DNA: Predictions of Exponential Growth and Decay of Coupling with Donor-Acceptor Distance. *J. Am. Chem. Soc.* **1993**, *115*, 2508-2510.
 41. Weiss, U., *Quantum Dissipative Systems*; World Scientific: Singapore, 1999.
 42. Liu, C.; Beratan, D. N.; Zhang, P., Coarse-Grained Theory of Biological Charge Transfer with Spatially and Temporally Correlated Noise. *J. Phys. Chem. B* **2016**, *120*, 3624-3633.
 43. Grozema, F. C.; Tonzani, S.; Berlin, Y. A.; Schatz, G. C.; Siebbeles, L. D. A.; Ratner, M. A., Effect of Structural Dynamics on Charge Transfer in DNA Hairpins. *J. Am. Chem. Soc.* **2008**, *130*, 5157-5166.
 44. Hu, Y.; Zhu, Y.; Gao, H.; Guo, H., Conductance of an Ensemble of Molecular Wires: A Statistical Analysis. *Phys. Rev. Lett.* **2005**, *95*, 156803.
 45. Haiss, W.; Wang, C.; Grace, I.; Batsanov, A. S.; Schiffrin, D. J.; Higgins, S. J.; Bryce, M. R.; Lambert, C. J.; Nichols, R. J., Precision Control of Single-Molecule Electrical Junctions. *Nat. Mater.* **2006**, *5*, 995-1002.
 46. Jang, S.-Y.; Reddy, P.; Majumdar, A.; Segalman, R. A., Interpretation of Stochastic Events in Single Molecule Conductance Measurements. *Nano Lett.* **2006**, *6*, 2362-2367.
 47. Salomon, A.; Cahen, D.; Lindsay, S.; Tomfohr, J.; Engelkes, V. B.; Frisbie, C. D., Comparison of Electronic Transport Measurements on Organic Molecules. *Adv. Mat.* **2003**, *15*, 1881-1890.
 48. He, J.; Sankey, O.; Lee, M.; Tao, N.; Li, X.; Lindsay, S., Measuring Single Molecule Conductance with Break Junctions. *Faraday Discuss.* **2006**, *131*, 145-154.
 49. Li, C.; Pobelov, I.; Wandlowski, T.; Bagrets, A.; Arnold, A.; Evers, F., Charge Transport in Single Au | Alkanedithiol | Au Junctions: Coordination Geometries and Conformational Degrees of Freedom. *J. Am. Chem. Soc.* **2008**, *130*, 318-326.
 50. Cometto, F. P.; Paredes-Olivera, P.; Macagno, V. A.; Patrito, E. M., Density Functional Theory Study of the Adsorption of Alkanethiols on Cu(111), Ag(111), and Au(111) in the Low and High Coverage Regimes. *J. Phys. Chem. B* **2005**, *109*, 21737-21748.
 51. Yu, M.; Bovet, N.; Satterley, C. J.; Bengio, S.; Lovelock, K. R. J.; Milligan, P. K.; Jones, R. G.; Woodruff, D. P.; Dhanak, V., True Nature of an Archetypal Self-Assembly System: Mobile Au-Thiolate Species on Au(111). *Phys. Rev. Lett.* **2006**, *97*, 166102/1-166102/4.
 52. Haiss, W.; Martín, S.; Leary, E.; Zalinge, H. v.; Higgins, S. J.; Bouffier, L.; Nichols, R. J., Impact of Junction Formation Method and Surface Roughness on Single Molecule Conductance. *J. Phys. Chem. C* **2009**, *113*, 5823-5833.
 53. Tivanski, A. V.; He, Y.; Borguet, E.; Liu, H.; Walker, G. C.; Waldeck, D. H., Conjugated Thiol Linker for Enhanced Electrical Conduction of Gold-Molecule Contacts. *J. Phys. Chem. B* **2005**, *109*, 5398-5402.
 54. Chen, F.; Li, X.; Hihath, J.; Huang, Z.; Tao, N., Effect of Anchoring Groups on Single-Molecule Conductance: Comparative Study of Thiol-, Amine-, and Carboxylic-Acid-Terminated Molecules. *J. Am. Chem. Soc.* **2006**, *128*, 15874-15881.

55. Park, Y. S.; Whalley, A. C.; Kamenetska, M.; Steigerwald, M. L.; Hybertsen, M. S.; Nuckolls, C.; Venkataraman, L., Contact Chemistry and Single-Molecule Conductance: A Comparison of Phosphines, Methyl Sulfides, and Amines. *J. Am. Chem. Soc.* **2007**, *129*, 15768-15769.
56. Venkataraman, L.; Klare, J. E.; Tam, I. W.; Nuckolls, C.; Hybertsen, M. S.; Steigerwald, M. L., Single-Molecule Circuits with Well-Defined Molecular Conductance. *Nano Lett.* **2006**, *6*, 458-462.
57. Xiang, L.; Palma, J. L.; Bruot, C.; Mujica, V.; Ratner, M. A.; Tao, N., Intermediate Tunnelling–Hopping Regime in DNA Charge Transport. *Nat. Chem.* **2015**, *7*, 221-226.
58. Huang; Chen, F.; Bennett, P. A.; Tao, Single Molecule Junctions Formed Via Au–Thiol Contact: Stability and Breakdown Mechanism. *J. Am. Chem. Soc.* **2007**, *129*, 13225-13231.
59. Bruot, C.; Xiang, L.; Palma, J. L.; Tao, N., Effect of Mechanical Stretching on DNA Conductance. *ACS Nano* **2015**, *9*, 88-94.
60. Bruot, C.; Xiang, L.; Palma, J. L.; Li, Y.; Tao, N., Tuning the Electromechanical Properties of Single DNA Molecular Junctions. *J. Am. Chem. Soc.* **2015**, *137*, 13933-13937.
61. Nitzan, A., The Relationship between Electron Transfer Rate and Molecular Conduction 2. The Sequential Hopping Case. *Isr. J. Chem.* **2002**, *42*, 163-166.
62. Nitzan, A., A Relationship between Electron-Transfer Rates and Molecular Conduction. *J. Phys. Chem. A* **2001**, *105*, 2677-2679.
63. Berlin, Y. A.; Ratner, M. A., Intra-Molecular Electron Transfer and Electric Conductance Via Sequential Hopping: Unified Theoretical Description. *Radiat. Phys. Chem.* **2005**, *74*, 124-131.
64. Traub, M. C.; Brunschwig, B. S.; Lewis, N. S., Relationships between Nonadiabatic Bridged Intramolecular, Electrochemical, and Electrical Electron-Transfer Processes. *J. Phys. Chem. B* **2007**, *111*, 6676-6683.
65. Zhou, X.-S.; Liu, L.; Fortgang, P.; Lefevre, A.-S.; Serra-Muns, A.; Raouafi, N.; Amatore, C.; Mao, B.-W.; Maisonhaute, E.; Schöllhorn, B., Do Molecular Conductances Correlate with Electrochemical Rate Constants? Experimental Insights. *J. Am. Chem. Soc.* **2011**, *133*, 7509-7516.
66. Wierzbinski, E.; Venkatramani, R.; Davis, K. L.; Bezer, S.; Kong, J.; Xing, Y.; Borguet, E.; Achim, C.; Beratan, D. N.; Waldeck, D. H., The Single-Molecule Conductance and Electrochemical Electron-Transfer Rate Are Related by a Power Law. *ACS Nano* **2013**, *7*, 5391-5401.
67. O'Neill, M. A.; Barton, J. K., DNA Charge Transport: Conformationally Gated Hopping through Stacked Domains. *J. Am. Chem. Soc.* **2004**, *126*, 11471-83.
68. O'Neill, M. A.; Barton, J. K., DNA-Mediated Charge Transport Requires Conformational Motion of the DNA Bases: Elimination of Charge Transport in Rigid Glasses at 77 K. *J. Am. Chem. Soc.* **2004**, *126*, 13234-5.
69. Wierzbinski, E., et al., Effect of Backbone Flexibility on Charge Transfer Rates in Peptide Nucleic Acid Duplexes. *J. Am. Chem. Soc.* **2012**, *134*, 9335-9342.
70. Lewis, F. D.; Wu, Y.; Zhang, L.; Zuo, X.; Hayes, R. T.; Wasielewski, M. R., DNA-Mediated Exciton Coupling and Electron Transfer between Donor and Acceptor Stilbenes Separated by a Variable Number of Base Pairs. *J. Am. Chem. Soc.* **2004**, *126*, 8206-8215.

71. Liu, T.; Barton, J. K., DNA Electrochemistry through the Base Pairs Not the Sugar-Phosphate Backbone. *J. Am. Chem. Soc.* **2005**, *127*, 10160-10161.

2.0 A SCANNING TUNNELING MICROSCOPE BREAK JUNCTION METHOD WITH CONTINUOUS BIAS MODULATION

This work was published as: Beall, E.; Yin, X.; Waldeck, D. H.; Wierzbinski, E. *Nanoscale* **2015**, 7, 14965-14973. The author of the dissertation performed all the experiments presented. The author of the dissertation was the first author. The supporting information for this chapter can be found in Appendix A.

Single molecule conductance measurements on 1,8-octanedithiol were performed using the Scanning Tunneling Microscope Break Junction method with an externally controlled modulation of the bias voltage. Application of an AC voltage is shown to improve the signal to noise ratio of low current (low conductance) measurements as compared to the DC bias method. The experimental results show that the current response of the molecule(s) trapped in the junction and the solvent media to the bias modulation can be qualitatively different. A model RC circuit which accommodates both the molecule and the solvent is proposed to analyze the data and extract a conductance for the molecule.

2.1 INTRODUCTION

Development of experimental methods for determining the charge transfer properties of organic molecules has evolved to allow measurements on individual molecules.¹⁻⁴ Among the measurement methods, the scanning tunneling microscope break junction (STM-BJ) has earned considerable popularity because of its simplicity and high measurement rate and because of the ability to make measurements on a variety of molecules and their conformers.¹ In STM-BJ the STM tip is repeatedly brought into contact with the substrate and then pulled away (withdrawn). This process forms a tip-substrate gap that is narrow enough to be bridged by a molecule(s) of sub-nanometer to nanometer length range. At a constant applied bias, the presence of a molecule(s) in the break junction gives rise to a non-zero current manifested as a plateau or series of plateaus in the current versus tip displacement curves. The magnitude of the current in the plateau is related to the conductance and number of molecules in the junction.

Several improvements to the method have expanded its applicability and the amount of the information provided by each experiment. One set of modifications focuses on mechanical modulation of the STM-BJ.⁵⁻⁷ Control over the tip – substrate separation in these experimental approaches is accomplished by modulation of the extension/contraction of the piezoelement that controls the z-direction movement of the STM tip. Consequently, the transition between different molecular conformations can be probed with greater control than in the traditional STM-BJ, which uses a constant tip withdrawal rate.^{5,7} Furthermore, the application of a continuous, high frequency, low amplitude modulation in the piezoelement movement helps resolve changes in the molecule-electrode contact or molecule conformation in the junction, in particular in differentiating a junction occupied by a molecule from an empty gap between the junction electrodes.⁶ In a related set of STM-BJ modifications, modulation of the bias voltage within the STM-BJ is accomplished

by sweeping the bias voltage while the position of the STM tip is stopped during the withdrawal in STM-BJ.⁸⁻¹⁰ Recently, Adak et al. applied a small amplitude, 22 kHz AC sinusoidal modulation in addition to a constant DC bias rather than linear bias sweeps in order to determine details of energy alignment and electronic couplings between molecular levels of pyridine-linked molecular bridges and of gold and silver electrodes.¹¹ Application of such procedures can provide more information about the molecular junction than that obtained by a constant bias junction. However, these methods require rigorous control of the STM tip movement and extreme tip position stability.

This work describes a simple experimental procedure in which single molecule current-voltage curves are collected for the STM BJ under a constant tip movement. In this procedure, we utilize the same tip crashing-withdrawal procedure typically used in STM-BJ but instead of applying a constant bias from the STM controller, a modulation voltage is applied continuously from an external voltage source. The present work focuses on a symmetrical triangular bias waveform (linear voltage-time sweeps in every modulation period with the same sweep rate in up and down directions) between 0 and 0.6 V.^{12, 13} Current responses are collected for a voltage bias modulation over the frequency range of 500 – 2000 Hz. The workable range of applied modulation frequency is limited by the duration of the junction and the sampling time on the low and high frequency end, respectively.

2.2 RESULTS AND DISCUSSION

A schematic illustration of a junction with the gold tip withdrawn at a constant rate from the gold substrate, in the presence of 1,8-octanedithiol in an organic solvent is shown in Figure 2.1A. In the experiment, the electrical current flowing through the junction is measured as a function of voltage and tip displacement (or time). The current traces have three main characteristic regions: (i) a rapid exponential current drop after the break of the metal-metal nanowire contact

between the electrodes; (ii) an intermediate state in which current flows through the molecules spanning the electrodes (indicated by arrows in Figure 2.1B,C), and (iii) a low current condition at large tip-surface separations. In the case of a modulated bias, the magnitude of the current varies with the potential bias applied at any given moment; thus the measured current varies with the frequency of the bias voltage waveform. The current traces obtained in the absence of a molecule(s) in the junction are also different under constant and modulated bias conditions. While under constant bias, the current remains constant (nominally zero) after the initial exponential drop. The current oscillates around zero when a bias modulation is applied (inset in Figures 2.1B,C).

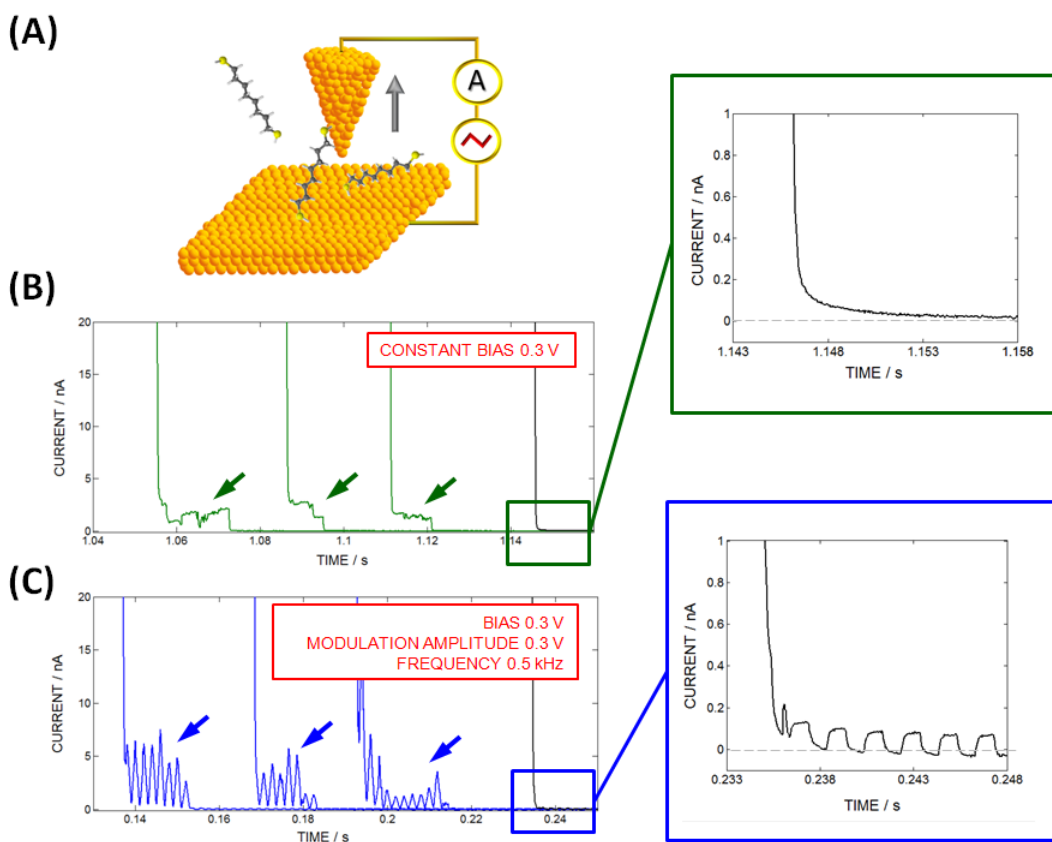


Figure 2.1. Panel A shows a schematic illustration of the molecular junction formed in a scanning tunneling microscope with a gold tip and gold substrates as the electrodes. Panels B and C show sample current – time traces obtained in the presence of 1,8-octanedithiol in mesitylene solvent, measured under a constant bias of 0.3 V (B) and a modulated bias of 0.3 ± 0.3 V (C). In both cases the retraction speed is 40 nm/s.

Black traces in B and C are characteristic for molecule-free junctions. Arrows indicate the current responses of the molecules trapped in the junction.

In the absence of any molecule(s) bound in the junction (i.e., solvent only), the measurement displays a charging current waveform. This waveform originates from the STM tip and the substrate electrode forming a capacitor. The capacitance is characteristic for a given experimental system and depends on the surface area of the substrate electrode, the diameter of the wire used for preparation of the STM tip, and the volume of the solvent in the experimental liquid cell. These geometrical parameters were kept constant in our measurements, and a consistent current response was observed over the course of all performed experiments. A uniform amplitude response was recorded for the STM tip –substrate separations between a few angstroms to 40 nm (the amplitude of the charging current waveform is very weakly dependent on the STM tip – substrate separation: about 1% decrease per 100 micrometers). Detailed information on the dependence of the geometrical factors on the response of the junction to the bias voltage is provided in the Appendix A. The capacitance response displays strong sensitivity to the solvent used in the measurements (see Figure 2.2). Figure 2.2 A-C shows current waveforms measured for mesitylene, 2,4-dichlorotoluene, and 3,4-dichlorotoluene. The shapes can be rationalized by a simple RC circuit model. The amplitude of the current modulation increases with the polarity of solvent. Note the change in current scale for panels A, B, and C. Because of the different solvent molecule polarities, their dielectric constants are different, which leads to a change in the junction's capacitance. For mesitylene, the current waveform resembles closely the square wave characteristic expected for an in-series capacitor-resistor circuit below its frequency cutoff (i.e., the duration of the voltage modulation period is longer than the time constant of the circuit, see Appendix A). For dichlorotoluene, the junction response has a longer time constant and the current waveform is more triangular; i.e., the current is passed by the junction with less attenuation and

less distortion (see Supporting Information for more detail). Figure 2.2D shows the calculated dipole moment of the solvent molecules under an increasing electrical field. Note that the static dipole moment of the solvent molecules increases from mesitylene (0 D) to 3,4-dichlorotoluene (3.1 D) and the induced dipole moment increases linearly with the strength of the applied electric field. The deformation of the current waveform decreases for mesitylene at higher frequency of the bias modulation (see Supporting Information). A more detailed description of the model equivalent circuit developed for the solvent is provided later in the text. The data in Figure 2.2 reveal that the solvent affects the current response to a voltage sweep in the molecular junction. This effect must be considered when quantifying the overall current signal through the molecular junction.

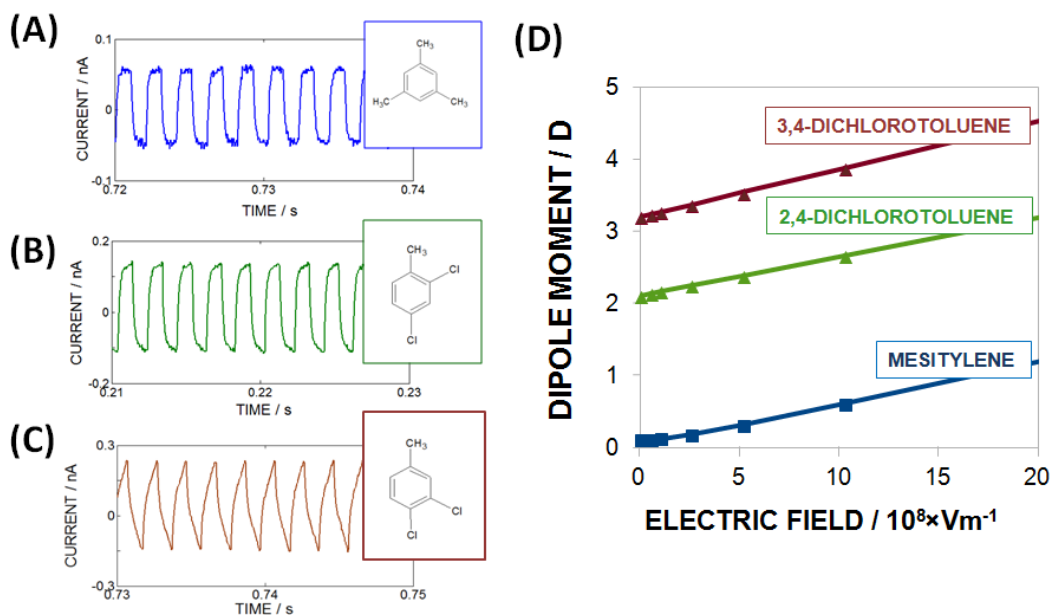


Figure 2.2. Panels A through C show current responses of the solvent under a bias voltage of 0.3 V that is modulated by 0.3 V at a frequency of 500 Hz for (A) mesitylene (dielectric constant $\epsilon=2.28$)¹⁴, (B) 2,4-dichlorotoluene ($\epsilon=5.68$)¹⁴, and (C) 3,4-dichlorotoluene ($\epsilon=8.97$)¹⁵. Panel D shows calculated results for the influence of the electrical field strength on the dipole moment induced in these molecules. Note that zero electric field corresponds to the static dipole moment of the solvent molecules.

If octanedithiol molecules are present, the amplitude of the bias-induced current oscillations through the junction is significantly higher than that of the mesitylene solvent (Figure 2.3A) or the 2,4-dichlorotoluene solvent (Figure 2.3B). Furthermore, the current waveforms become triangular and are offset from the zero current. This behavior is consistent with a resistance in parallel with the junction capacitance. If ohmic behavior is assumed for the molecule in the junction, the variations in the current amplitude within the experimental trace can be explained by the changes in the resistance from the molecule(s) in the junction during the course of the junction extension. Note that the presence of the adlayer of the octanedithiol molecules on the gold substrate surface does not have a noticeable influence on the solvent capacitive charging current waveform.

In the STM-BJ method, a large number of individual molecules and their conformations can be probed by repeating the experiment many times. This process allows one to construct distributions of the observed current. Because these global distributions are constructed by summation of the distributions built from many individual traces, they represent a property of the ensemble rather than the behavior of a given molecule. For the case of measurements under constant bias, the currents within the plateaus observed on the individual traces are observed more often than other fragments of the trace, so that peaks are formed in the current distributions. For the modulated bias case, the measured current varies with applied bias and the current response is sampled over a voltage range, albeit narrow. The current distributions constructed from the data recorded under constant and modulated bias for 1,8-octanedithiol in mesitylene and 2,4-dichlorotoluene are shown in Figure 2.3C. All the distributions show a main peak around 1 nA, and an additional small shoulder at 0.05 to 0.15 nA. The position of the ~ 1 nA peak is independent of the measurement method (DC versus modulated bias), which indicates that the solvent's response to the applied bias modulation has a negligible effect on the measured current, the current

response is higher than that of the solvent alone. For low currents (< 0.5 nA), the peak is shifted towards higher values when the bias modulation method is used. The magnitude of the shift is proportional to the current response of the solvent and it is notably bigger in 2,4-dichlorotoluene than in mesitylene.

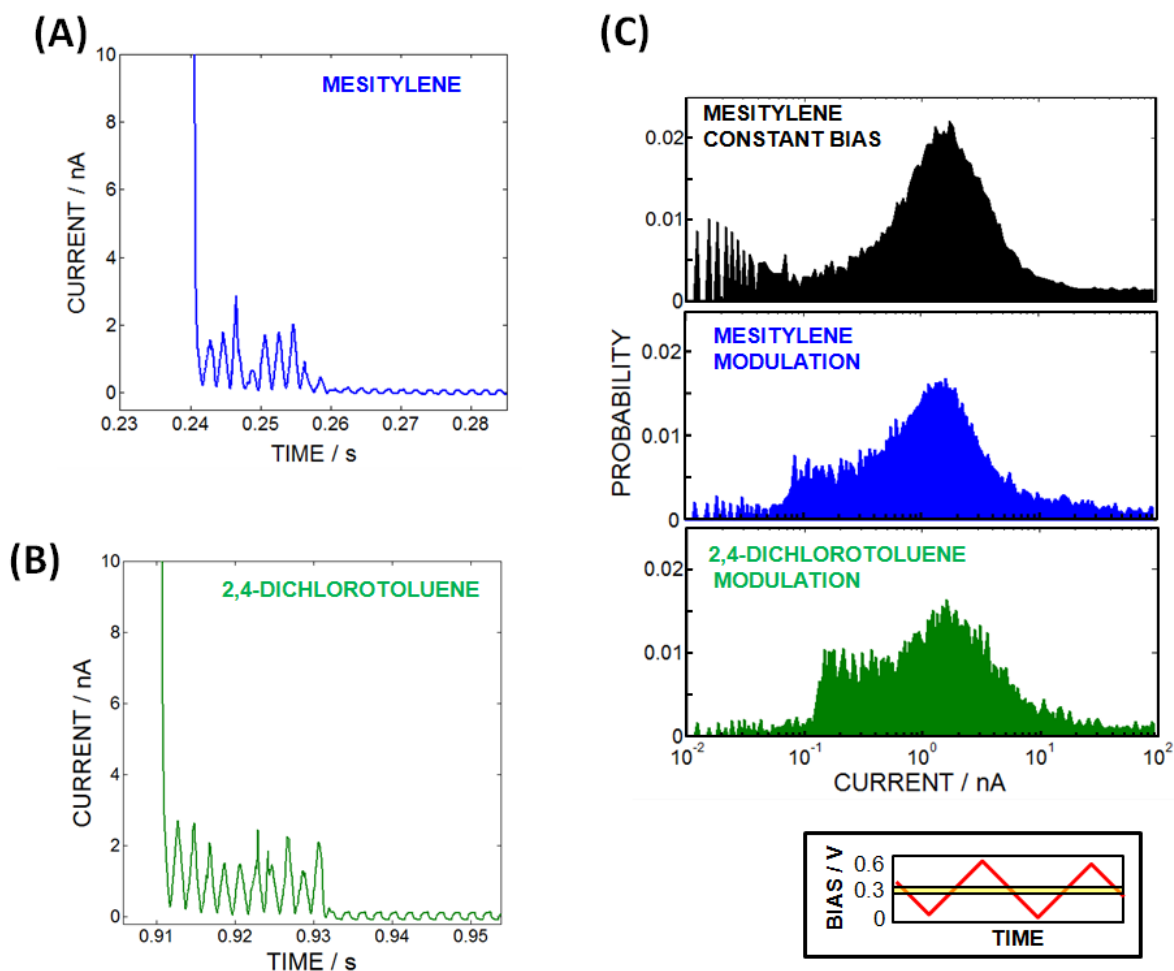


Figure 2.3. Panels A and B show sample current – time traces obtained in the presence of 1,8-octanedithiol in mesitylene (A) and in 2,4-dichlorotoluene (B) solvent, measured under a bias of 0.3 ± 0.3 V modulated with frequency of 500 Hz. Panel C shows histograms of many current versus time traces, measured in mesitylene and in 2,4-dichlorotoluene. The currents corresponding to a narrow 0.29 – 0.31 V range of applied bias (shown schematically in the inset in panel C as yellow box) were extracted to construct the distributions. Data obtained under constant bias of 0.3 V in mesitylene is shown for comparison. The current response characteristic for the solvent was not included in the analysis.

We note that the influence of the solvent on the conductance of the molecular bridge may be due to the shift in the alignment of its molecular levels with respect to the Fermi levels of the electrodes and to the broadening of the bridge energy level distribution, which was predicted by theory.¹⁶ However, previous experimental studies showed no¹⁷ or only a weak effect¹⁸ of the solvent on the molecular conductance. In the present studies, a similar position of the current peak at ~ 1 nA in the current distributions of 1,8-octanedithiol in 2,4-dichlorotoluene and in 3,4-dichlorotoluene (see Figure 2.3C) indicates that the solvent does not affect the molecular conductance of the dithiol significantly, but adds up to the current measured in the junction.

To quantify the influence of the solvent and to extract the conductance of the molecule from the current measured in the octanedithiol junction, simulations of the current response arising from the applied bias were performed with a model electrical circuit and the Matlab Simulink software. Figure 2.4A shows a comparison of an experimental current – time trace (black diamonds) with that simulated by an RC circuit (red curve). In this model the octanedithiol molecule is treated as a resistor that acts in parallel to the solvent, which is modeled as a resistor and capacitor in series. Parameters of the solvent RC circuit (yellow rectangle in Figure 2.4) were simulated first to match the current response of the junction with only solvent (modulation periods number 9 and 10). Note that simulation of the leakage current through the solvent (i.e., leaky capacitor model) requires inclusion of a resistor R_S' ; however, this resistor is not necessary for mesitylene.

When an octanedithiol molecule is present in the junction, the amplitude of the current oscillations are higher than in the case of solvent alone. This change is modeled by a shunt resistance (R_M) that is associated with a molecule binding across the gap. Two distinct regions with two different resistances were present for the current trace of Figure 2.4A. In the region

highlighted in green, the amplitude of the current oscillations is closer to that observed for the solvent (mesitylene) alone than it is to that of the oscillations highlighted in blue. Furthermore, the current response shown in the green region has a shape that is intermediate between triangular (purely resistive) and square wave (purely capacitive). This distorted waveform reflects the combination of the solvent and the molecule to the response. In the region highlighted in blue, the current displays a triangular waveform with significantly higher amplitude than the solvent. In this current range, elimination of the solvent RC arm in the model electrical circuit causes little to no effect on the simulated current. Therefore, the equivalent circuit for this part of the trace can be simplified to the circuit shown in blue. Note that the distribution of the currents constructed for 1,8-octanedithiol in mesitylene from the modulated-bias data shown in Figure 2.3C is dominated by the peak with a maximum at 1-2 nA. In this regime, the solvent response to the bias modulation is negligible and the current measured around 0.3 V bias was the same as in the case of the constant bias measurement.

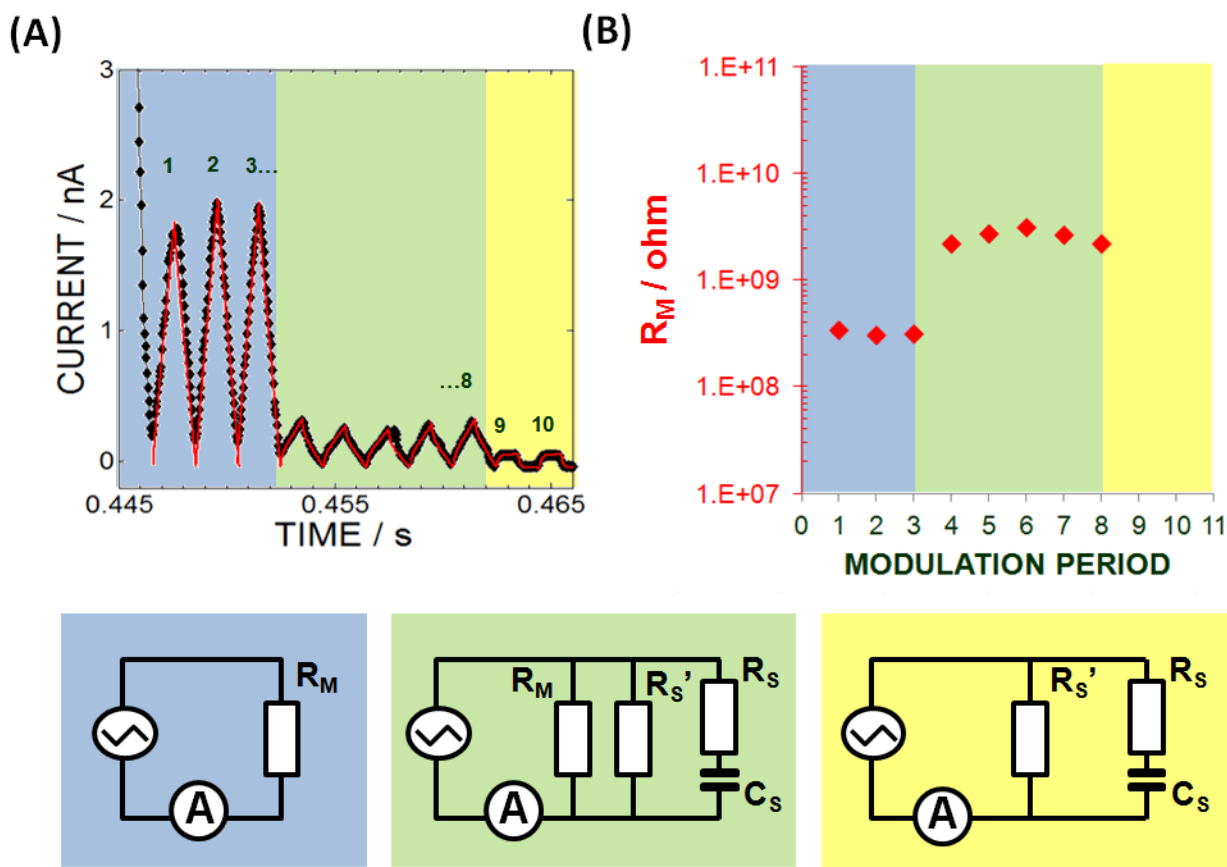


Figure 2.4. Results of fitting the experimental current versus time trace using a model electrical circuit. Panel A shows a sample experimental curve obtained in mesitylene under 0.3 ± 0.3 V bias modulation applied with 500 Hz frequency (black symbols), together with a simulated current response of the model electrical circuit (red lines). In the model electrical circuit, the measured molecule (1,8-octanedithiol) is represented as a resistor (R_M), and the solvent is modeled as a leaky capacitor [two resistors (R_S , R_S') and a capacitor (C_S)]. Parameters of the circuit elements associated with the solvent were kept constant ($R_S'=1 \times 10^{11} \Omega$, $R_S=9 \times 10^8 \Omega$, $C_S=8.25 \times 10^{-14}$ F). The simulations were performed to match each individual modulation period in the experimental curve using the most general circuit presented in the bottom row of the figure (green rectangle). Circuits in the blue and yellow rectangular region represent limiting approximations of the most general model circuit (green), in which the current response is determined solely by the molecule trapped in the junction (blue) or by the response of the solvent media alone (yellow). Panel B shows R_M values obtained for the 1,8-octanedithiol molecule in the current-time profile shown in panel A.

The resistance of the molecule in the green and blue regions differs by nearly one order of magnitude, whereas within the blue or green region the resistances for the different cycles are within 30% of each other. This observation is consistent with the presence of two different molecule-electrode conformations (low versus medium conductance) rather than a difference in

the number of molecules effectively wired in the junction.¹⁹⁻²² Within the blue region, the fit gives a resistance of $0.32 \pm 0.02 \text{ G}\Omega$ for the three cycles; within the green region, the fit gives a resistance of $2.55 \pm 0.37 \text{ G}\Omega$.

Figure 2.5 shows an example of an experimental trace, in which current oscillations are more complex. The trace is divided in a similar way to that in Figure 2.4, although notable current fluctuations are observed within the regions associated with octanedithiol. These variations between different modulation periods result in a change of simulated resistance close to a factor of two; thus it is very likely that the trace represents the situation in which two octanedithiol molecules are trapped simultaneously. Note that the inverse of the bias voltage frequency applied in the experiment is relatively large in comparison to the time for a molecule to ‘jump’ from one configuration to another in the junction; however, its residence time in a particular geometry appears to last for many periods. Figure 2.5B shows examples of the modulation periods for which two simulations were performed to match different fragments of the data. Interestingly, the obtained R_M values correspond to the same resistances found for the other modulation periods, which is in agreement with the assumption of two molecules being trapped in the junction (one or two equivalent resistors in parallel wired into the circuit); and they ‘jump’ between being ‘wired’ and not ‘wired’.

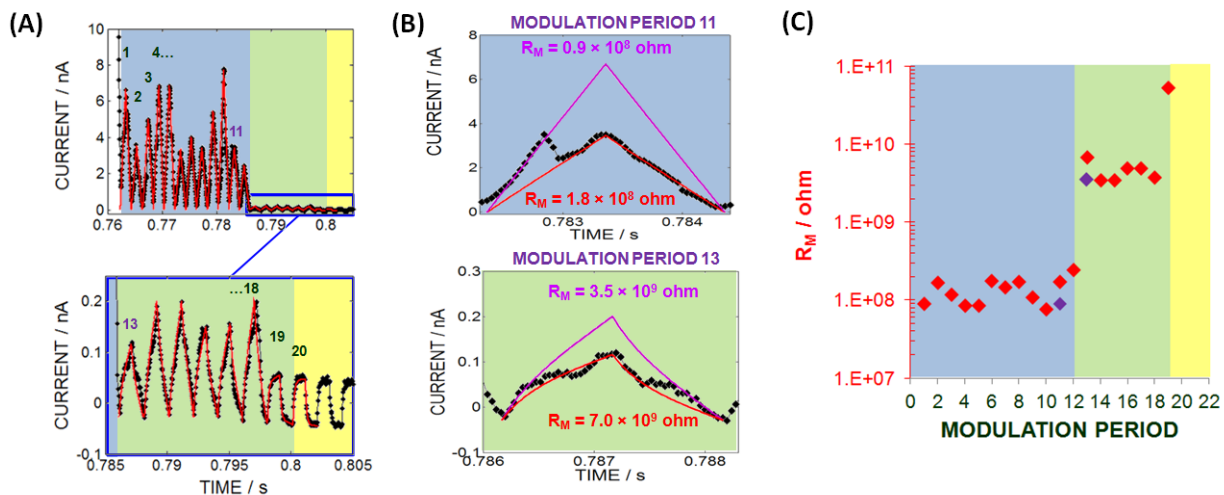


Figure 2.5. Results of fittings to experimental data with the model electrical circuit. Panel A shows a sample experimental curve obtained in mesitylene under $0.3 \pm 0.3 \text{ V}$ bias modulation applied with 500 Hz frequency (black symbols), together with a simulated current response of the model electrical circuit (red lines). Panel B shows examples of modulation periods, within which a change in the conformation of the molecules in the junction was observed. Only fits shown in red are included in panel A. Circuit parameters associated with the solvent are the same for all the simulated data ($R_S'=1.0 \times 10^{11} \Omega$, $R_S=9.0 \times 10^8 \Omega$, $C_S=7.8 \times 10^{-14} \text{ F}$). Panel C shows the fitted R_M value corresponding to subsequent modulation periods shown in panels A (red symbols) and B (violet symbols).

One would expect that a decrease of the modulation frequency would result in a larger proportion of the periods in which changes of the conformation of the molecule(s) in the junction are captured, and the information about the molecule(s)' conductance would more closely approximate the average of that for one and two molecules. The average resistance determined from all the periods within the blue region in Figure 2.4A is $0.13 \pm 0.05 \text{ G}\Omega$; however, the current-time trace indicates a bimodal distribution of currents. The junction changes dynamically between two resistances, approximately $0.17 \pm 0.03 \text{ G}\Omega$ and $0.09 \pm 0.01 \text{ G}\Omega$; see Figure 2.5C. Similarly, in the green region, the average resistance from all the periods gives $4.50 \pm 1.30 \text{ G}\Omega$, while distinct periods indicate two groups of resistances of $3.58 \pm 1.26 \text{ G}\Omega$ and $5.68 \pm 1.12 \text{ G}\Omega$. In this study, the octanedithiol current-time traces were recorded at sub-kHz frequency of the bias voltage modulation, and the examples shown demonstrate that the kinetics of the molecule(s) binding in

the junction can be probed at the single molecule level; i.e. within a single experimental trace. Application of even higher voltage modulation frequencies will likely prove to be even more beneficial for this type of quantification.

By collecting together data from one to two thousand curves, current-voltage distributions that correspond to an average electrical response of the ensemble of molecules can be constructed. Figure 2.6A shows an example of such a distribution for 1,8-octanedithiol. Importantly, it contains data at significantly more bias potentials than the characteristics constructed in traditional STM-BJ (typically from less than ten bias voltages). For example, construction of such a two-dimensional distribution using constant bias would require one hundred and twenty datasets (typically a few hundred traces each) recorded between 0 and 0.6 V with 5 mV increments. In contrast to the measurements with the bias sweeps at constant tip position, the histogram obtained using the procedure presented in this manuscript gives averaged information over the ensemble of the molecules and conformations. Furthermore, because each experimental trace contains information about the response of the solvent, that information can be used to extract the resistance data of the molecule more reliably, in particular for small currents (low conductance).

Figure 2.6B shows the distribution of conductance values obtained for the same dataset as the current distributions shown in Figure 2.3C for mesitylene. The conductance values were obtained by matching the periods in the current-time traces to a library of current responses simulated using predefined R_M values. The main peak in the distribution, around $7 \times 10^{-5} G_0$, is close to the conductance reported for 1,8-octanedithiol ($6 \times 10^{-5} G_0$),¹⁹⁻²¹ while the broad peak/shoulder agrees with the reported value of $\sim 1 \times 10^{-6} G_0$.²² In all these literature studies, differences in the measured conductance were interpreted as originating from details of the Au-S contact. The distribution obtained using the modulated STM-BJ (blue histogram) and the DC bias

method (black solid line) match with respect to the position of the conductance peaks. Nevertheless, in the case of modulated STM-BJ, the octanedithiol conductance is determined well over the entire available conductance range (with the lowest conductance restricted by the conductance of the pure solvent, and the high limit given by the sensitivity of STM preamplifier). In the case of DC measurements, the low conductance data (nominally calculated from the currents lower than 50 pA) is strongly affected by the sensitivity of the STM pre-amplifier and is very noisy.

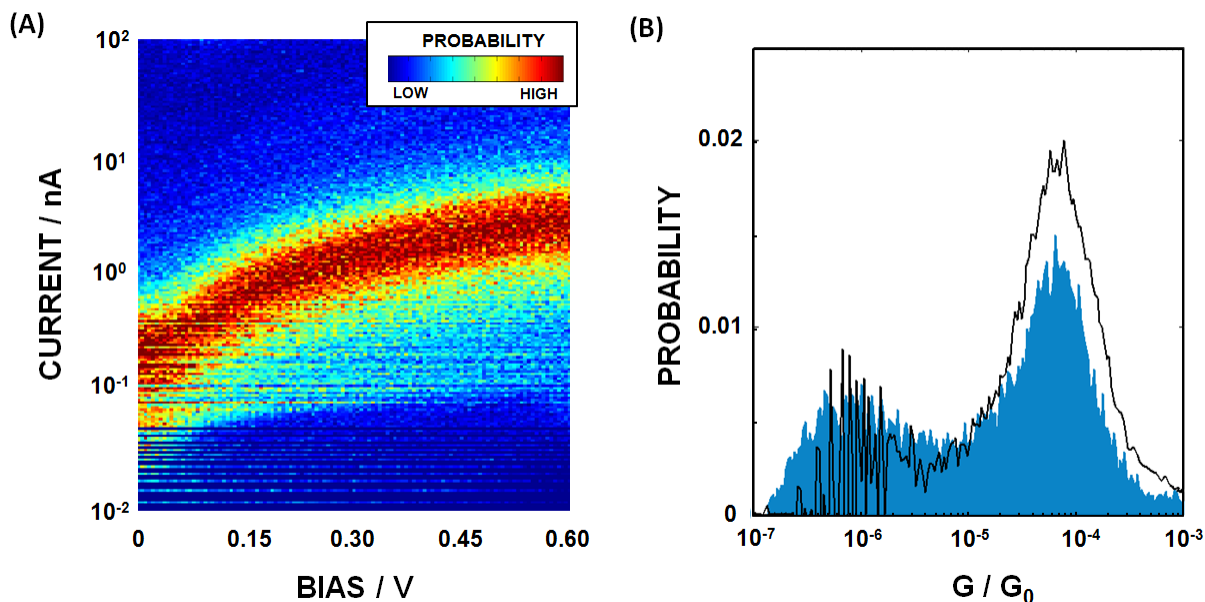


Figure 2.6. Panel A shows a two-dimensional current – voltage distribution constructed from two thousand current - time traces recorded for 1,8-octanedithiol in mesitylene under the bias modulation conditions of 0.3 ± 0.3 V (500 Hz). Because the bias voltage is generated continuously and is independent of the STM tip withdrawal procedure, the applied bias and the current measured in the junction were matched in phase based on the characteristic response of the solvent to the applied bias. Panel B shows the octanedithiol conductance distribution obtained by matching the modulation periods in experimental traces (blue histogram) with the library of two hundred current responses simulated for the circuits with predefined R_M values in a range 10^7 - 10^{11} ohm. Parameters of the circuit elements associated with the solvent were kept constant ($R_S'=1 \times 10^{11}$ Ω , $R_S=9 \times 10^8$ Ω , $C_S=8.25 \times 10^{-14}$ F). The data is compared with the conductance distribution obtained using the constant bias STM BJ method (black curve). The conductance values are expressed in the units of the quantum conductance, $G_0 = 2e^2/h \approx 77$ μ S.

2.3 CONCLUSIONS

In summary, a simple experimental procedure that allows current – voltage characterization of molecular junctions with high statistics was presented. The method is intermediate between the traditional STM BJ (with constant bias applied) and the procedures in which STM movement is controlled within the STM tip withdrawal in order to perform a bias voltage sweep, e.g. transition voltage spectroscopy. Importantly, the AC modulation method reveals the effect of the solvent medium on the response and allows it to be separated from that of the molecule bound across the junction. A model RC-circuit was shown to be useful for quantifying the effect of the solvent and the molecule in the junction. Application of the voltage modulation in molecular conductance measurements improves the extraction of low conductance data when compared to the constant voltage methodology. This study is a stepping stone towards the use of AC impedance methods for characterizing molecular tunnel junctions.

2.4 METHODS

2.4.1 Conductance Measurements

The modulated-bias conductance measurements were performed using a variation on the STM-controlled break-junction method.¹ Through repeated cycles of precise retraction following a crashing of the STM tip, the studied molecule was able to occasionally form a molecular junction between the tip and substrate during the retraction period. The constant retraction speed of 40 nm/s was used in all measurements. During this process, an externally-generated modulated bias voltage (DS345 Function Generator, Stanford Research Systems) was applied in the form of a triangle wave to the bias voltage input of the STM breakout box. The tunneling current was subsequently monitored as a function of time; i.e. voltage and the tip-substrate distance. Piezoelement movement, current measurements, and the constant bias voltage (exclusively in control

experiments) are regulated/measured by the STM which is controlled by standard software provided by the microscope vendor. In all measurements an STM scanner with a 10 nA/V pre-amplifier was used. Conductance values were determined through analysis of the current-distance plots as well as current-voltage characteristics (*vide infra*). All measurements were performed using an Agilent 5500 system with an environmental chamber housed in a homemade acoustically isolated Faraday cage. The cage sits on an active Table Stable anti-vibration system mounted on an optical table.

2.4.1.1 Sample Preparation

Ultraflat template-stripped gold substrates²³ were used. For substrate preparation, a 100 nm gold film was evaporated using a Thermionics VE-180 E-beam evaporator on freshly cleaved mica. Glass slips (10 mm x 25 mm) were affixed to the bare gold and the film was transferred to a glass slip prior to each experiment. The newly exposed atomically flat gold substrates were immersed for 20-30 seconds in a 2 mM 1,8-octanedithiol solution in ethanol, rinsed with ethanol and dried under an argon stream.

2.4.1.2 Data Collection

Experiments were performed using freshly cut gold STM tips (0.25 mm, 99.95% gold wire, Alfa Aesar). All experiments were performed under an argon atmosphere with the substrates in mesitylene, 2,4-dichlorotoluene, or 3,4-dichlorotoluene. The modulation amplitude of the applied bias was ± 0.3 V with the triangle wave centered about 0.3 V and modulation frequencies ranging from 0.5 kHz to 2 kHz. Measurements were collected using a 10 nA/V preamplifier. Thousands of current-distance profiles were collected for each set of parameters, typically requiring several independent substrates and multiple STM tips to be used in order to amass sufficient data.

2.4.1.3 Data Analysis

Home-written Matlab scripts were used for current-distance plot data filtering and analysis. Plots displaying current plateaus were selected from the set of thousands of traces and the current response was matched to the generated triangle-wave bias in order to determine the respective applied bias for every current data point.

A three-dimensional distribution was generated with a logarithmically scaled current axis having 25 bins per decade and a linearly scaled applied bias axis having 25 bins per 0.1 V. The color-scaled surface can then be partitioned to show a normalized histogram for a specific bias. The conductance values were obtained by matching individual periods in the current – time traces with the library of two hundred current responses simulated using model circuit (green rectangular in Figure 2.4 in manuscript) with predefined R_M values spaced logarithmically between 10^7 and 10^{11} ohm. The quality of the match between experimental and simulated data was found by calculating the χ^2 defined as:

$$\chi^2 = \sum_n \left(\frac{i_{exp}(n) - i_{sym}(n)}{error(n)} \right)^2 \quad \text{Equation 2.1}$$

where i_{exp} and i_{sym} are experimental and simulated current values for each data point ‘ n ’ in a given period. A constant error of 5 pA was used for the currents below 100 pA, and 5 percent of the simulated current value for the remaining data points. The R_M value, for which the simulated response produced the smallest χ^2 was used. 10 percent of the periods with the highest χ^2 values out of the entire dataset were omitted in construction of the conductance distribution.

2.4.2 Calculation of the Dipole Moment of Solvent Molecules Under Various Electrical Fields

Ground state geometry optimization was performed at the B3LYP/6-31G(d) level for mesitylene, 2,4-dichlorotoluene, and 3,4-dichlorotoluene using Gaussian 09.²⁴ An external electric field was applied along the direction of the intrinsic dipole moments during optimization. Although DFT methods are known to ignore dispersion, the hybrid B3LYP functional^{25, 26} was found to be acceptable for comparing the trend among small organic molecules^{27, 28} and thus was used in the calculations.

2.5 REFERENCES

1. B. Xu and N. J. Tao, *Science*, 2003, **301**, 1221.
2. X. D. Cui, A. Primak, X. Zarate, J. Tomfohr, O. F. Sankey, A. L. Moore, T. A. Moore, D. Gust, G. Harris and S. M. Lindsay, *Science*, 2001, **294**, 571.
3. M. A. Reed, C. Zhou, C. J. Muller, T. P. Burgin and J. M. Tour, *Science*, 1997, **278**, 252.
4. X. Guo, J. P. Small, J. E. Klare, Y. Wang, M. S. Purewal, I. W. Tam, B. H. Hong, R. Caldwell, L. Huang, S. O'Brien, J. Yan, R. Breslow, S. J. Wind, J. Hone, P. Kim and C. Nuckolls, *Science*, 2006, **311**, 356.
5. J. S. Meisner, M. Kamenetska, M. Krikorian, M. L. Steigerwald, L. Venkataraman and C. Nuckolls, *Nano Lett.*, 2011, **11**, 1575.
6. J. L. Xia, I. Díez-Pérez and N. J. Tao, *Nano Lett.*, 2008, **8**, 1960.
7. J. Zhou, G. Chen and B. Xu, *J. Phys. Chem. C*, 2010, **114**, 8587.
8. J. M. Artés, M. López-Martínez, A. Giraudet, I. Díez-Pérez, F. Sanz and P. Gorostiza, *J. Am. Chem. Soc.*, 2012, **134**, 20218.
9. S. Guo, J. Hihath, I. Díez-Pérez and N. Tao, *J. Am. Chem. Soc.*, 2011, **133**, 19189.
10. K. Wang, J. Hamill, J. Zhou, C. Guo and B. Xu, *Faraday Discuss.*, 2014, **174**, 91.
11. O. Adak, R. Korytár, A. Y. Joe, F. Evers and L. Venkataraman, *Nano Lett.*, 2015, **15**, 3716.
12. *We slightly extended the bias voltage range for which linear current response to applied voltage was reported for 1,8-octanedithiol. (Morita T., Lindsay M, J. Am. Chem. Soc. 2007, 129, 7262)*
13. T. Morita and S. Lindsay, *J. Am. Chem. Soc.*, 2007, **129**, 7262.
14. *CRC Handbook of Chemistry and Physics 84th Ed.*, CRC Press, Boca Raton, FL, 2003.
15. R. R. Dreisbach, in *Physical Properties of Chemical Compounds*, American Chemical Society, 1961, vol. 15, ch. 1, pp. 3-523.
16. I. Baldea, *Nanoscale*, 2013, **5**, 9222.
17. H. van Zalinge, D. J. Schiffrin, A. D. Bates, W. Haiss, J. Ulstrup and R. J. Nichols, *ChemPhysChem*, 2006, **7**, 94.

18. V. Fatemi, M. Kamenetska, J. B. Neaton and L. Venkataraman, *Nano Lett.*, 2011, **11**, 1988.
19. F. Chen, X. Li, J. Hihath, Z. Huang and N. Tao, *J. Am. Chem. Soc.*, 2006, **128**, 15874.
20. W. Haiss, S. Martín, E. Leary, H. v. Zalinge, S. J. Higgins, L. Bouffier and R. J. Nichols, *J. Phys. Chem. C*, 2009, **113**, 5823.
21. C. Li, I. Pobelov, T. Wandlowski, A. Bagrets, A. Arnold and F. Evers, *J. Am. Chem. Soc.*, 2008, **130**, 318.
22. E. Wierzbinski and K. Slowinski, *Langmuir*, 2006, **22**, 5205.
23. M. Hegner, P. Wagner and G. Semenza, *Surf. Sci.*, 1993, **291**, 39.
24. M. J. Frisch, G. W. Trucks, H. B. Schlegel, G. E. Scuseria, M. A. Robb, J. R. Cheeseman, G. Scalmani, V. Barone, B. Mennucci, G. A. Petersson, H. Nakatsuji, M. Caricato, X. Li, H. P. Hratchian, A. F. Izmaylov, J. Bloino, G. Zheng, J. L. Sonnenberg, M. Hada, M. Ehara, K. Toyota, R. Fukuda, J. Hasegawa, M. Ishida, T. Nakajima, Y. Honda, O. Kitao, H. Nakai, T. Vreven, J. A. Montgomery Jr., J. E. Peralta, F. Ogliaro, M. J. Bearpark, J. Heyd, E. N. Brothers, K. N. Kudin, V. N. Staroverov, R. Kobayashi, J. Normand, K. Raghavachari, A. P. Rendell, J. C. Burant, S. S. Iyengar, J. Tomasi, M. Cossi, N. Rega, N. J. Millam, M. Klene, J. E. Knox, J. B. Cross, V. Bakken, C. Adamo, J. Jaramillo, R. Gomperts, R. E. Stratmann, O. Yazyev, A. J. Austin, R. Cammi, C. Pomelli, J. W. Ochterski, R. L. Martin, K. Morokuma, V. G. Zakrzewski, G. A. Voth, P. Salvador, J. J. Dannenberg, S. Dapprich, A. D. Daniels, Ö. Farkas, J. B. Foresman, J. V. Ortiz, J. Cioslowski and D. J. Fox, *Gaussian 09 Revision B.01*, 2010.
25. A. D. Becke, *J. Chem. Phys.*, 1993, **98**, 5648.
26. C. Lee, W. Yang and R. G. Parr, *Phys. Rev. B*, 1988, **37**, 785.
27. Y. Li, J. Zhao, X. Yin and G. Yin, *J. Phys. Chem. A*, 2006, **110**, 11130.
28. X. Quan, C. W. Marvin, L. Seebald and G. R. Hutchison, *J. Phys. Chem. C*, 2013, **117**, 16783.

3.0 EFFECTS OF THE BACKBONE AND CHEMICAL LINKER ON THE MOLECULAR CONDUCTANCE OF NUCLEIC ACID DUPLEXES

This work was published as: Beall, E.; Ulku, S.; Liu, C.; Wierzbinski, E.; Zhang, Y.; Bae, Y.; Zhang, P.; Achim, C.; Beratan, D. N.; Waldeck, D. H. *J. Am. Chem. Soc.* **2017**, *139*, 6726-6735.

The author of the dissertation performed the conductance measurements and prepared the manuscript. The author of the dissertation was the co-first author. The supporting information for this chapter can be found in Appendix B.

Scanning tunneling microscope-break junction measurements are used to examine how the molecular conductance of nucleic acids depends on the composition of their backbone and the linker group to the electrodes. Molecular conductances of 10-base pair long homoduplexes of DNA, aeg-PNA, γ -PNA, and a heteroduplex of DNA/aeg-PNA with identical nucleobase sequence were measured. The molecular conductance was found to vary by 12 to 13 times with the change in backbone. Computational studies show that the molecular conductance differences between nucleic acids of different backbones correlate with differences in backbone structural flexibility. The molecular conductance was also measured for duplexes connected to the electrode through two different linkers, one directly to the backbone and one directly to the nucleobase stack. While the linker causes an order-of-magnitude increase in the overall conductance for a particular duplex, the differences in the electrical conductance with backbone composition are preserved. The highest molecular conductance value, 0.06 G_0 , was measured for aeg-PNA duplexes with a base stack linker. These findings reveal an important new strategy for creating longer and more complex electroactive, nucleic acid assemblies.

3.1 INTRODUCTION

The past decade has witnessed important breakthroughs in DNA nanotechnology.¹⁻³ Researchers have demonstrated how to use Watson-Crick base pairing rules to program the self-assembly of nucleic acids into a diverse array of shapes and structures, and it is now possible to imagine creating a wide range of functional motifs. The use of these nanostructures in electronic and electrochemical applications will rely on a deeper understanding of their charge transmission and electron transfer mechanisms.⁴⁻⁷ Nucleic acids display unusual complexity in their charge transport properties, with mechanisms that range from coherent tunneling at short distances, to incoherent hopping at long distances, and coherent ballistic charge transfer via the flickering resonance mechanism at intermediate distances.^{4, 8-10} Moreover, these various regimes and the transitions between them are known to be sensitive to nucleobase sequence, length, and charge injection energy. For coherent tunneling, the local energetics of the base stack dominates the charge transport; whereas for charge hopping and flickering, the electrical conductance is likely linked to the conformational dynamics of the duplex. For these reasons, understanding the influence of the molecular backbone on the electron transmission properties of nucleic acids is important to developing our understanding and eventually to realizing the promise of DNA molecular electronics.

The use of DNA nanotechnology in bioelectronics will require that we understand and control the structural fluctuations of these soft biomaterials and their effect on the molecular conductance. For example, it has been shown that the conformation of DNA duplexes can lead to drastic changes in the single molecule electrical conductance.¹¹⁻¹³ Additional strategies that include incorporating intercalators and metal ions into the base stack have been used to affect the structure and electrical properties of nucleic acid duplexes.¹⁴⁻¹⁶ Given that orbital overlap of adjacent

nucleobases dictates nearest neighbor electronic couplings, the ability to access different conformations can modulate the conductance of a duplex significantly. This work asks how the single molecule conductance of a duplex depends on its structural flexibility and nucleobase overlap by examining a set of nucleic acid duplexes that have identical nucleobase sequence and identical linkers but different backbone structures, which leads to different conformational flexibility. In particular, the molecular conductance is compared for four different backbone motifs: the phosphate sugar backbone of DNA, aminoethylglycine peptide nucleic acid (aeg-PNA),¹⁷ a gamma-modified (γ -PNA) backbone,¹⁸ and a DNA/aeg-PNA heteroduplex.

PNA is a synthetic analogue of DNA that has a neutral aminoethylglycine backbone rather than the negatively charged, sugar phosphodiester backbone of DNA.¹⁷ γ -PNA has a substituent at the γ -position of the backbone that makes it intrinsically chiral and reduces its conformational freedom.¹⁸ Solution structures obtained by NMR spectroscopy and crystal structures of these nucleic acid duplexes have shown that homoduplexes of aeg-PNA and γ -PNA adopt a P-helix structure,¹⁹⁻²¹ whereas DNA homoduplexes²² and DNA/PNA heteroduplexes²³⁻²⁴ adopt a B-DNA helix structure (Figure 3.1). The fact that both aeg-PNA and γ -PNA are more flexible than DNA is supported by the fact that heteroduplexes of both PNAs with DNA adopt a B-DNA structure characteristic of DNA homoduplexes.²³⁻²⁵ Examination of the backbone's chemical structure suggests that aeg-PNA is more flexible than γ -PNA, which in turn is more flexible than DNA; this inference is supported by NMR studies of these nucleic acids in solution²⁰⁻²¹ and by molecular dynamics studies.²⁶ Thus, a comparison of the conductance of these molecules should provide insight into the importance of backbone flexibility on the single molecule conductance.

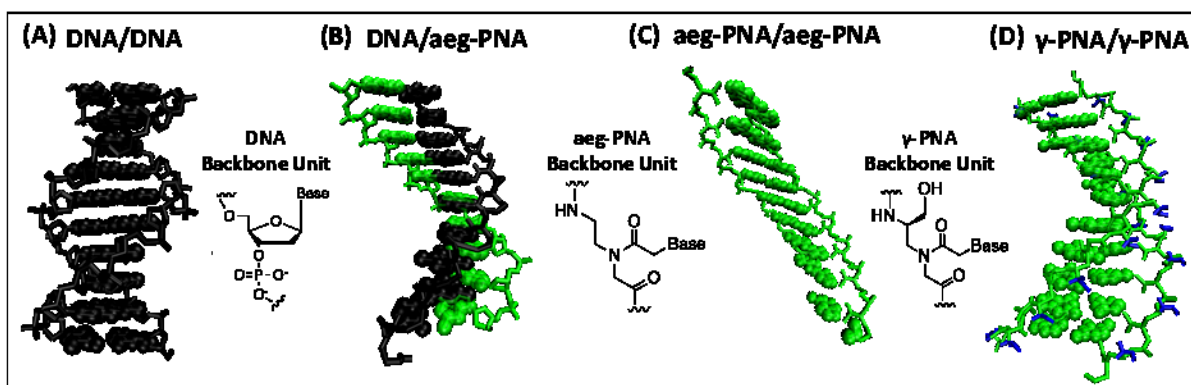


Figure 3.1. Renderings for the four duplexes (A) DNA homoduplex, (B) DNA /aeg-PNA heteroduplex, (C) aeg-PNA homoduplex, and (D) γ -PNA homoduplex are shown. In each case the sequence is AGTTTGTACG. The insets show the chemical structures for the backbones of DNA, aeg-PNA, and γ -PNA.

Previous studies have shown that the electrochemical charge transfer rates of nucleic acids are influenced by their structural flexibility.²⁷⁻²⁹ In a study by Wierzbinski and coworkers, the electrochemical rate constant was measured through aeg-PNA and γ -PNA duplexes, and the γ -PNA duplexes were shown to have a smaller rate by a factor of two.²⁷ The experimental observation of larger electrochemical rate constants for aeg-PNA as compared to those for γ -PNA was rationalized as arising from an increase in the energy level broadening of the hole mediating superexchange states with the increase in duplex flexibility; or, alternatively, arising from the ability of the more flexible aeg-PNA duplexes to access conformations with higher electronic couplings more often than do γ -PNA duplexes. As both γ -PNA and aeg-PNA adopt a P-helix structure,¹⁹⁻²⁰ the diminished rate is likely to arise from the relative flexibility of the backbones rather than from differences in the average nucleobase overlaps that might arise for different helix geometries. The dependence of electron transfer rates on structural fluctuations was also observed in studies on DNA/LNA hybrids²⁹ and reported for DNA duplexes at different temperatures.³⁰ Because the electron transfer rate is directly related to the electrical conductance,³¹ it seems

plausible that such effects can cause differences between the single molecule conductance of nucleic acid duplexes.

In addition to the backbone composition, the effect of changing the chemical linker between the nucleic acid and the electrode was examined. Figure 3.2 shows molecular structures for the two linker types. The propylthiol linker is covalently tethered to the nucleic acid backbone, whereas the amino thymidine linker is covalently coupled to a nucleobase. In recent work on DNA conductance, Tao and coworkers showed that the use of an amino thymidine nucleoside linker significantly increased the conductance relative to a thiol linker.³²⁻³³ This increased conductance suggests that the amino thymidine linkers enhance the charge injection into the nucleobase stack, thus enhancing the molecular conductance. The current work examines whether this linker effect changes the sensitivity of the conductance to the backbone structure. In the limit that the charge transport proceeds by incoherent hopping (i.e., charge injection onto the bridge, hopping through the bridge nucleobases, and escape from the bridge to the counter electrode), one expects the overall resistance of the molecular junction to be a sum of resistances for each of the three steps; such a mechanism was recently used to describe electrochemical charge transfer with PNAs.³⁴ In contrast, if the charge transport proceeds coherently, then the decomposition into resistances for each step is no longer possible; rather the transport should be viewed as a product of transmission probabilities for each step.³⁵ By contrasting how the single molecule conductance of DNA and PNA duplexes change with the different linker types, insights into the nature of the conduction mechanism, incoherent versus coherent, can be ascertained.

3.2 RESULTS

Although extensive research has examined the dependence of molecular conductance of nucleic acid duplexes on the sequence of the duplex, this study is the first to examine the influence of different backbones of nucleic acid duplexes on the molecular conductance of duplexes that have the same sequence of 10 base pairs, AGTTTGTACG and its complement. Specifically we compare duplexes that have a pseudopeptide backbone based on aminoethyl-glycine aeg-PNA, a pseudopeptide backbone based on γ -hydroxymethylene-aminoethyl-glycine γ -PNA, and sugar diphosphate DNA (Figure 3.1). We also examine the influence on the molecular conductance of the linker that connects the duplex to the electrode, through the nucleic acid backbone (propylthiol) or the nucleobase stack to the electrode (a thymidine 5-C2 amino linker) (Figure 3.2).

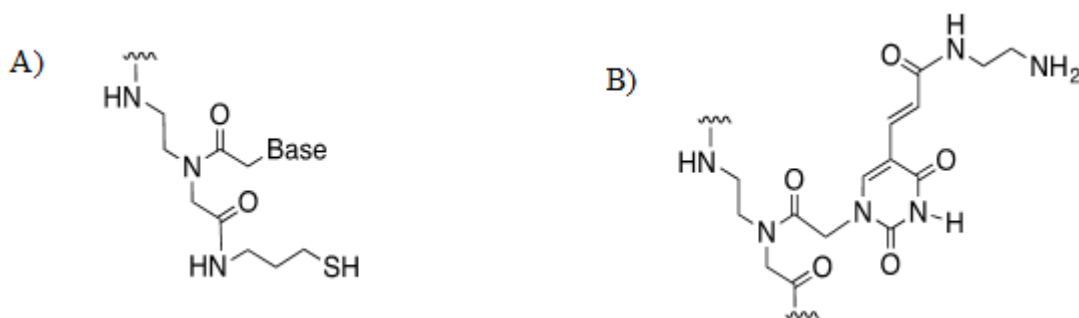


Figure 3.2. Chemical structure of the linkers that connect PNA to the Au surface. Panel A shows the propylthiol that is situated at the C end of the single stranded PNA. Panel B shows the thymidine 5-C2 amino linker which can be situated at any position in a single stranded PNA.

3.2.1 Conductance Measurements

The electrical conductance properties of the nucleic acid duplexes were investigated by using the scanning tunneling microscope break junction (STM-BJ) method,³⁶ in which a triangular waveform bias voltage is applied to the gold STM tip as it is retracted;³⁷ see Figure 3.3A. Molecular junctions are formed between a gold substrate and the gold STM tip by way of terminal linkers positioned on the opposing termini of the duplexes. The current between the electrodes is

monitored as the STM tip is withdrawn from the substrate surface, providing a current-time (current-distance) profile or trajectory. Electrical conduction through a purely resistive molecular junction manifests in a triangular current-time waveform response (see Figure 3.3B), whereas junctions without such molecules give a more complex (leaky capacitor) response. The typical tip displacement over one period of the applied triangle wave is 20 pm; < 9% of an Au-S bond length. A large set of trajectories for resistive molecular junctions were collected and their current responses were fit by an equivalent circuit model to yield a molecular conductance for each period of the waveform (see Supporting Information). A distribution of molecular conductance values was measured for each duplex.

The trajectory shown in Figure 3.3B was taken for an aeg-PNA homoduplex with propanethiol linkers on each strand. It displays two regimes of conductance during the time (~12 periods) that the STM tip is withdrawn and a molecular junction is formed with the substrate. The multiple modes observed within a conductance distribution could be attributed to different relative orientations of the linkers with respect to the gold electrodes and/or to different conformations of the molecule within the molecular junctions.³⁸ At early times, a higher conductance mode is observed and the current fluctuates between 30 and 60 nA. This fluctuation can be attributed to the presence of one and two molecules ‘wired’ in parallel in the junction,³⁶ or to structural variations of the duplex, which have been shown to affect the conductance of the molecular junction.^{30, 39} Varying the concentration of the nucleic acid duplexes on the surface indicated that a higher molecular coverage causes these fluctuations in the current response to occur more frequently, supporting the interpretation that two molecules in the junction cause the fluctuations. At later times, the higher conductance mode transitions to a much lower conductance regime with a more stable current response. This transition could reflect a change in the binding of the linker

groups to the gold substrate or the partial unraveling of the nucleic acid strand.⁴⁰ The latter possibility is less likely, however, as single strand molecules give much lower currents (<100 pA) than the ones observed here (5 to 10 nA for the lower conductance).^{31, 41-42} Although only two conductance modes are observed for some of the systems, the nomenclature of ‘high’ and ‘medium’ conductance modes is kept for consistency with published data on thiol linkers.^{31, 38, 43}

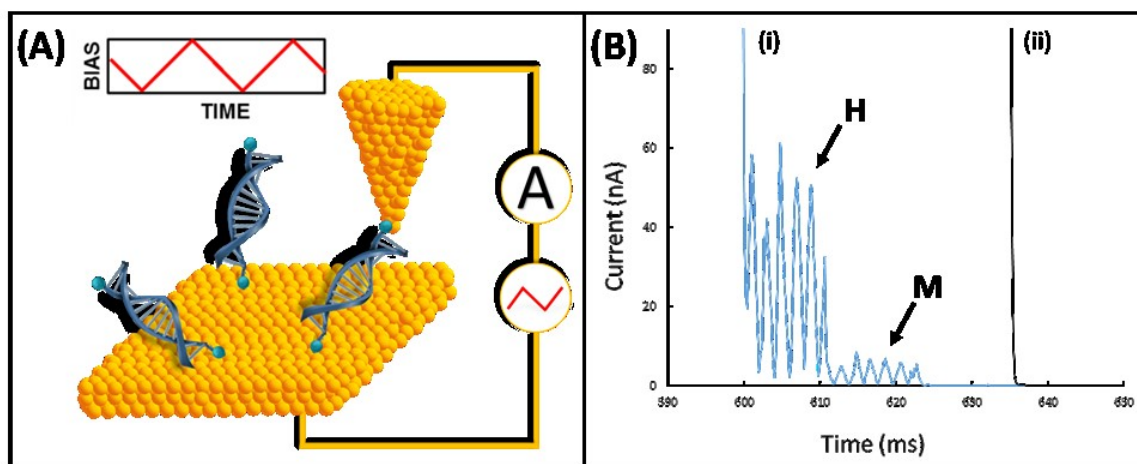


Figure 3.3. (A) The schematic for the single molecule conductance measurements. (B) Example current-time responses for the aeg-PNA homoduplex showing the triangular wave current response resulting from a molecular junction (i) and an ‘empty’ current response where a molecular junction does not occur (ii). For the current response showing the molecular junction, a clear transition occurs from the high conductance mode (H) to a lower conductance mode (M).

3.2.1.1 Backbone Comparison

Conductance distributions are shown in Figures 3.4B through 4E for the DNA, the aeg-PNA, the γ -modified PNA homoduplexes, and the DNA/aeg-PNA heteroduplex, in each case with propylthiol linker groups. These distributions were obtained from several thousands of measurements and are normalized to unit area for comparison purposes. For each duplex type, an example trajectory for one of the molecular junctions is also shown in panel A. The conductance distributions span several orders of magnitude and have a multimodal character. The data set for

the aeg-PNA homoduplex (Figure 3.4C) displays three modes; the data sets of the other three types of duplexes show two dominant conductance modes. The lowest mode of the DNA, γ -modified PNA, and DNA/aeg-PNA duplexes were not observed, presumably because of the sensitivity constraints of the preamplifier. We analyzed and compared the two highest conductance modes, which are observed for all four duplexes. The plots in Figure 3.4, show fits to the data by a sum of two Gaussian functions, which allows a 'peak' conductance value to be assigned for the two higher conductance modes.

Note that the high conductance mode often presents a shoulder on the high conductance side of the peak, at roughly twice the conductance of the peak. Analysis of these trajectories shows that the current response is fluctuating between integer multiples of a single value; i.e., the junction has two molecules bound across the junction and they act as two parallel resistors.³⁷ Thus, the main peak is attributed to the conductance of a single molecule junction and the shoulder to a junction containing two or more molecules.

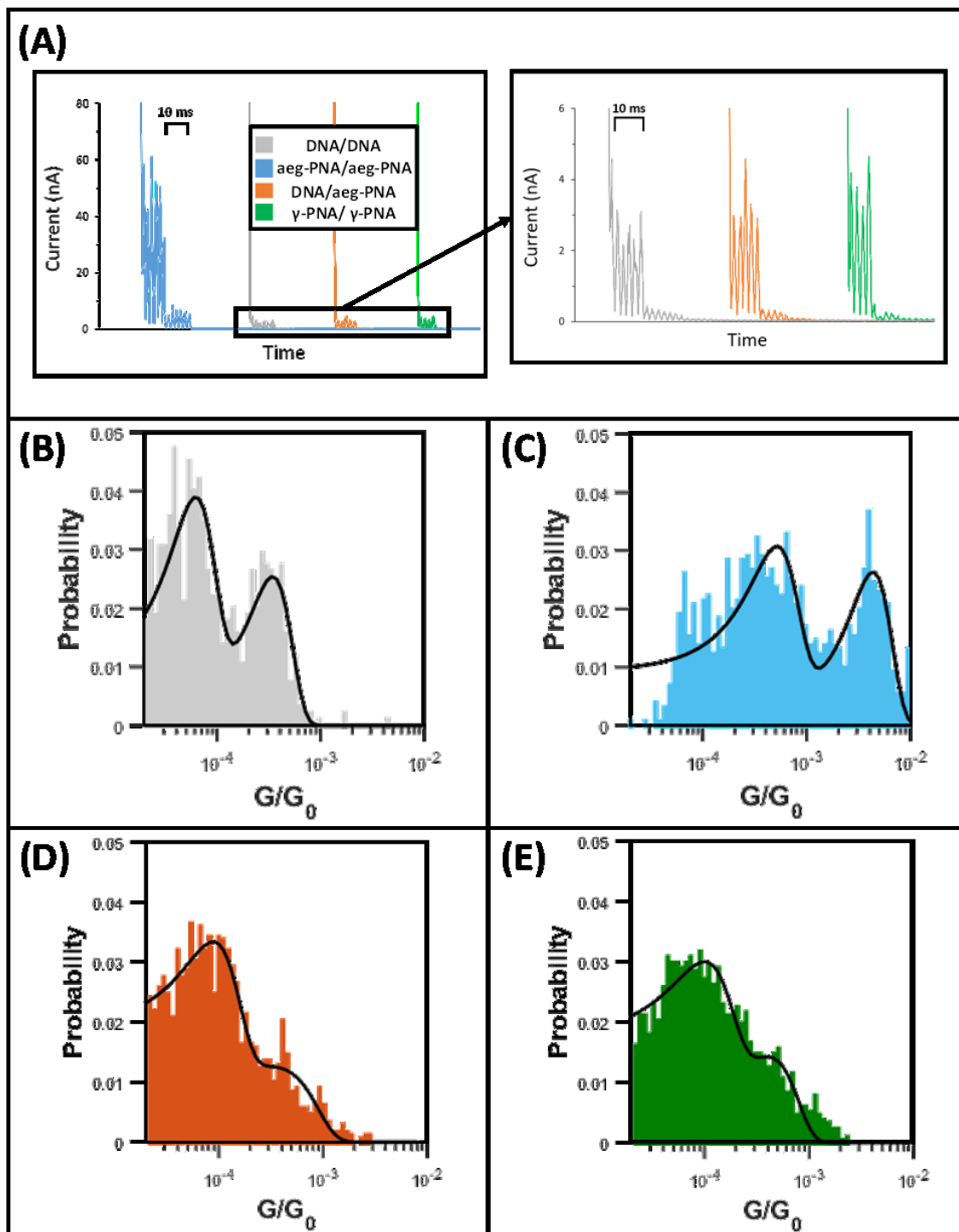


Figure 3.4. Panel A shows example current responses for the duplexes. The conductance histograms are shown for the DNA homoduplex (B), the aeg-PNA homoduplex (C), the DNA/aeg-PNA heteroduplex (D), and the γ -PNA homoduplex (E). The black curve is a fit of the histogram by a sum of two Gaussian

functions. The peaks in the distributions are associated with major conductance modes, referred to as high and medium modes.

The distribution of molecular conductances for the DNA homoduplex is shown in Figure 3.4B. The conductance at the peak maximum for the high conductance mode (most probable conductance for the high mode) is $3 \times 10^{-4} G_0$, where $G_0 = 2e^2/h$ is the quantum of conductance.⁴⁴ This value agrees with results reported for other 10-mer DNA duplexes with thiol linkers.^{40, 45-46} The magnitude of the current responses decreased drastically following roughly 20 angstroms of retraction, which is consistent with what was reported previously for these molecules.⁴⁰ This decrease was attributed to a severing of the hydrogen bonds between the two strands of the duplex which is the origin of the breakdown mechanism of the molecular junction.

Figure 3.4C shows the conductance distribution measured for the aeg-PNA homoduplex. The entire conductance distribution for the aeg-PNA is shifted to higher values than that for DNA (Figure 3.4B). The distribution for the aeg-PNA shows three conductance modes. A fit of these three modes using Gaussians yields most probable conductance values in a ratio of approximately 54 to 6 to 1 for the high to medium to low modes, respectively (see Supporting Information). These ratios are similar to those previously reported for alkanedithiols in Au junctions.³⁸ The values for the high and medium conductance modes of the aeg-PNA homoduplex agree well with those that were reported earlier.³¹ The most probable conductance for the high mode of the aeg-PNA duplex is ten times larger than the most probable conductance for the high mode of the DNA homoduplex.

The conductance distribution for the DNA/aeg-PNA heteroduplex is shown in Figure 3.4D and that for the γ -PNA homoduplex in Figure 3.4E. For both duplexes, the most probable conductance for the high mode, which is about $4 \times 10^{-4} G_0$, falls between the high conductance

mode observed for the DNA and aeg-PNA homoduplexes. This value is within 25% of the DNA homoduplex and about 10 times lower than that found for the high conductance mode of aeg-PNA.

Table 3.1 summarizes the conductance data for all the duplexes that were studied. The data show that the DNA/DNA, DNA/aeg-PNA, and γ -PNA/ γ -PNA have similar conductances. This similarity exists despite the fact that the backbones of the duplexes are different in chemical nature and have different electrostatic charge (see Figure 3.1). Moreover, the DNA homoduplexes and the DNA/PNA heteroduplexes form B-DNA helices, whereas aeg-PNA and γ -PNA homoduplexes form a P-type helix.^{19-20, 22-23}

In an earlier study, the γ -PNA was found to have an electrochemical rate constant smaller than that of aeg-PNA by a factor of two,²⁷ and this decrease was attributed to the change in flexibility of the two duplexes. The difference between the factor of ten in conductance and a factor of two in electrochemistry experiments may reflect the nonlinear relationship between the single molecule conductance and electron transfer rate³¹ as well as the difference in electronic decoherence between the aeg-PNA and γ -PNA.

3.2.1.2 Linker Study

Figure 3.5 shows conductance histograms for DNA and PNA homoduplexes with amino thymidine linkers and a fit to these data by a sum of Gaussians (black line). The DNA homoduplex has a most probable high conductance value of $1.8 \times 10^{-3} G_0$, which is five times higher than the same mode for the DNA homoduplex with a thiol linker (Figure 3.4B). Similarly, the aeg-PNA homoduplex with the amino thymidine linkers has a most probable high conductance mode that is over ten times higher than that observed for the thiol linkers, namely $0.062 G_0$.

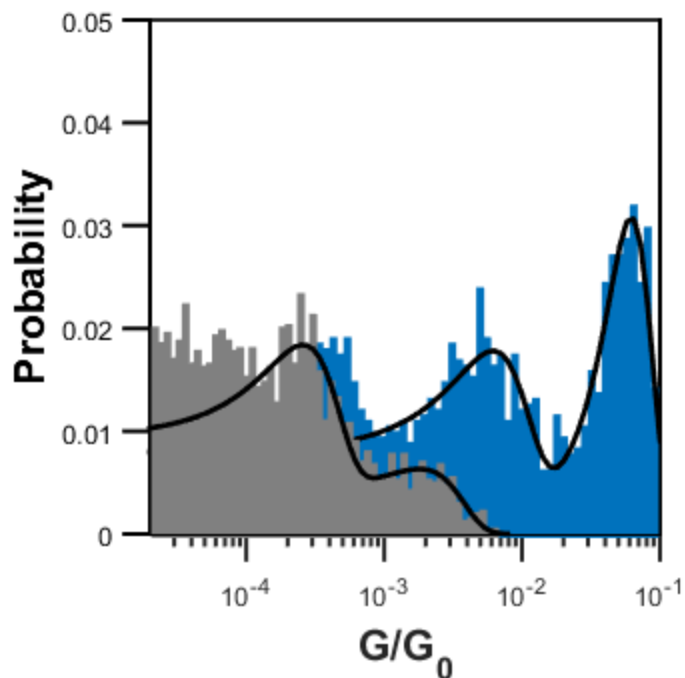


Figure 3.5. The conductance histograms for the DNA homoduplex (gray) with amine linkers and PNA homoduplex (blue) with amine linkers. The peaks in the distributions correspond to major conductance modes; the overlaid black curves are fits to the histogram by a sum of Gaussian functions.

These findings suggest that the linker strongly affects the conductance of duplexes. With this increase in overall conductance, the histogram shows the emergence of a low conductance peak for the DNA duplex, corroborating the earlier supposition that the third, low mode, was not observed for the thiol linkers because of instrumental limitations. The fact that the conductance measured for each duplex with amino thymidine linkers is larger than that for the same duplex with propylthiol linkers is attributed to better electronic coupling between the electrode and the nucleobase stack mediated by the former linker. It is notable that a conductance value as high as six percent of G_0 has been previously reported only for molecular junctions of a few angstroms, i.e. much shorter than the 30 angstrom PNA duplex studied here.⁴⁷⁻⁴⁸

3.2.1.3 Summary

Table 3.1 shows the most probable conductance values for the high (G_H) and medium (G_M) conductance modes observed in this study, as well as the ratios of the conductance of the high mode to medium mode. The conductance for both the high and medium modes increases from the DNA and γ -PNA homoduplexes, to the DNA/aeg-PNA heteroduplex, to the aeg-PNA homoduplex. The relative change in the medium conductance peak maximum for the four duplexes is slightly smaller than the relative change for the high conductance peak maximum; the more conductive duplexes have a slightly higher ratio. One can postulate that different modes of the conductance can originate from different nucleic acid duplex conformations and/or from different linker-gold electrode geometries. The G_H/G_M ratios reported here for the thiol linker are in reasonable agreement with previous findings for both nucleic acid duplexes and for alkanedithiols,³¹ which suggest that the different conductance modes originate from linker-gold conformation. The conclusion that different modes originate from changes in the linker group's binding geometry are further substantiated by comparison of the different conductance modes for the same core structures (notably DNA/DNA and aeg-PNA/aeg-PNA duplexes) but with different linkers $G_H(\text{amine})/G_M(\text{amine})$ and $G_H(\text{thiol})/G_M(\text{thiol})$ indicates somewhat different ratios. Since these conductance ratios are somewhat different, this trend cannot be explained solely by a conformational effect of the molecular backbone because the same 'high' to 'medium' ratios would be maintained when the linker identity is changed.

Table 3.1: Summary of the single molecule conductance measurements for the nucleic acid duplexes.

Linker Type	Duplex	$G_H / (10^{-4} G_0)$	$G_M / (10^{-4} G_0)$	G_H / G_M	% G_H
Thiol	DNA/DNA	3.4 ± 1.7	0.60 ± 0.32	5.7	47
	DNA/aeg-PNA	3.6 ± 1.9	0.86 ± 0.48	4.1	33
	γ -PNA/ γ -PNA	4.0 ± 3.3	0.92 ± 0.79	4.4	52
	aeg-PNA/aeg-PNA	43 ± 21	5.0 ± 3.0	8.7	53
Amine	DNA/DNA	18 ± 16	2.5 ± 1.9	7.2	31
	aeg-PNA/aeg-PNA	620 ± 240	59 ± 45	10.5	39

The relative probabilities of observing the high and medium modes are in reasonable agreement for the different duplexes. This consistency of the relative amounts of high and medium modes also supports the notion that the modes arise from different binding geometries, as one would not expect the relative occurrence of the different linker binding geometries to change significantly with the molecular backbone. See the Supporting Information for further discussion.

3.2.2 Computational Results

Computational studies were used to examine features of the backbone changes in the model system. Molecular dynamics (MD) simulations of the 10-mer duplexes were used to generate structures for the aeg-PNA, DNA, DNA/aeg-PNA, and γ -PNA duplexes. Quantum chemistry calculations (with the ZINDO method in Gaussian 09⁴⁹) of the electronic couplings were performed on the duplex structures generated by the MD simulations.

The Büttiker-Landauer probe approach was used to calculate the molecular conductances.⁵⁰⁻⁵² Büttiker virtual electrodes were introduced to simulate the dephasing induced

by the interaction of the molecule with the environment. In this approach, the conductance was calculated with the Hamiltonian

$$H_M = \sum_{i=1}^N \varepsilon_i |i\rangle \langle i| + \sum_{i=1}^{N-1} V_{i,i+1} |i\rangle \langle i+1| + h. c. \quad \text{Equation 3.1}$$

where ε_i is the mean site energy of purine site i , which is the HOMO energy. These calculations include the middle six base pairs in the molecular Hamiltonian, while treating the two base pairs at each end as part of the electrodes. The coupling between electrodes and the terminal molecular sites is taken to be 0.1 eV. The coupling between Büttiker probes and the molecular sites is set to 0.003 eV for γ -PNA, DNA/aeg-PNA, and DNA (indicative of slower dephasing) and 0.01 eV for aeg-PNA (indicative of faster dephasing) to reproduce the trend observed in the experimental measurements. Using this methodology, the calculated conductances were $18.9 \times 10^{-9} G_0$ for aeg-PNA/aeg-PNA, $2.26 \times 10^{-9} G_0$ for DNA/DNA, $2.67 \times 10^{-9} G_0$ for γ -PNA/ γ -PNA, and $1.48 \times 10^{-9} G_0$ for DNA/aeg-PNA. The conductance for the aeg-PNA homoduplex was also calculated using the same Büttiker probe coupling (0.003 eV) that was used for the other duplexes. In this instance, the calculated conductance is $1.87 \times 10^{-9} G_0$. This indicates that the increased conductance calculated for the aeg-PNA homoduplex is representative of the increased dephasing rate and not an increase in the nucleobase coupling for the aeg-PNA/aeg-PNA duplex. The need for a much faster dephasing rate to capture the experimentally observed conductance differences supports the notion that backbone flexibility affects the conductance. Faster dephasing introduces a greater admixture of incoherence in charge/energy transfer, which can increase the rate of charge⁵³⁻⁵⁵ and energy transfer⁵⁶⁻⁵⁸ in the weak dephasing regime. When the dephasing rate increases, a turning point is expected to be found, beyond which the charge/energy transfer rates

decrease with further increases in the dephasing rate. The experimental and computational results described here indicate that the dephasing rate in the nucleic acid molecular systems are in the weaker dephasing regime, where an increase in dephasing rate produces faster charge transfer rates. Coherent charge transfer may dominate with some contributions from incoherent channels. The reasons for the rate enhancement produced by dephasing include: (1) dephasing may suppress destructive coherent interference⁵⁴ and (2) dephasing produces spectral broadening and grows the probability of approaching a resonant mechanism.^{9, 56} Here, guanines and adenines have a redox potential difference of 0.35 eV.⁹ The flickering resonance mechanism, developed to describe the influence of thermal fluctuations on transient resonant charge transfer, is relevant when thermal fluctuations bring the energies of molecular species into quasi-degeneracy, enabling charge to move coherently across the system's transiently "flat" energy landscape.⁹ The flickering resonance probability grows for aperiodic systems as the site energy width grows. Stochastic Schrödinger equation studies of DNA structures support the idea that fluctuations can accelerate charge transfer in aperiodic systems.⁵⁹

Exploring the backbone flexibility in the context of helicoidal parameters provides a framework to understand the electronic dephasing in charge transfer.⁵⁸⁻⁶⁰ The fluctuations in the duplex structures were explored by simulating the thermal fluctuations of the structural parameters. Figure 3.6 shows the ratio of the structural parameter fluctuations for the aeg-PNA/aeg-PNA, γ -PNA/ γ -PNA, and DNA/aeg-PNA duplexes relative to DNA/DNA. aeg-PNA has systematically higher fluctuation widths in most structural parameters suggesting that aeg-PNA is the most flexible backbone motif. The required Büttiker probe coupling values needed to reproduce the experimentally determined conductance values appear plausible.⁵⁹⁻⁶⁰ The γ -PNA duplex has lower parameter fluctuations as compared to aeg-PNA except for the Buckle metric, indicating the

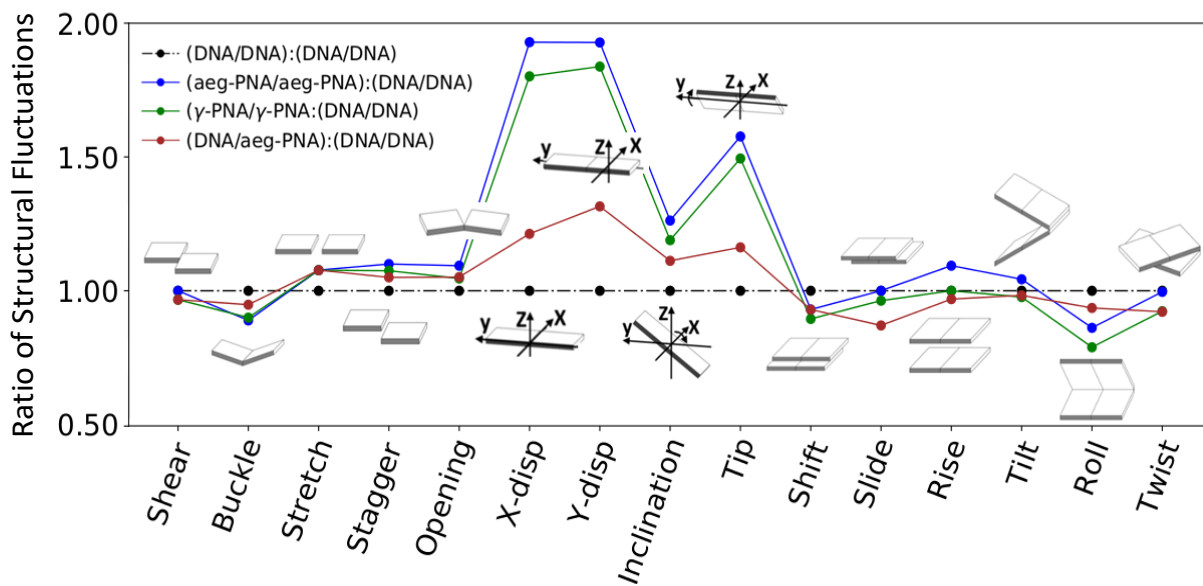


Figure 3.6. The ratio of structural parameter fluctuations (standard deviation of 10,000 MD snapshots, averaged among the middle 6-mers) between different backbone species as compared to DNA. Structural parameters are defined and calculated with x3DNA⁶¹. The detailed information about the parameter means and standard deviations of all base pairs are shown in the Supporting Information.

effective rigidification associated with γ -modification. Pairing a DNA strand with an aeg-PNA strand (as in the DNA/aeg-PNA duplex) rigidifies the whole structure as shown in Figure 3.6. The dephasing rate and the induced conductance enhancement are collective features of the system-environment interaction, which is represented by the fluctuations of structural parameters in our case. Dissecting the dephasing rate and the conductance by assigning a weight to each helical parameter in determining the dephasing rate and conductance is extremely challenging. The conductance enhancement is only observed in the aeg-PNA duplex, although the calculated structural parameter fluctuations of γ -PNA are slightly smaller than the parameter fluctuation width in aeg-PNA (see Figure 3.6).²⁰ More quantitative descriptions of the nucleic acids' structural parameters are limited by available molecular dynamics methods and the force fields. Our qualitative study found that dephasing due to molecular flexibility is an essential parameter that influences charge transfer rates, other than the structure of the energy landscape and the electronic

coupling strength. Details on the conductance calculations, based on the Büttiker-Landauer method, are provided in the supporting information.

Note that the effective charge injection between the STM tip and the guanine (for the amine modified structures) is mediated by a thymine base, which should enhance the effective coupling compared to the case in the thiol modified structures. Finally, we note that the magnitude of the computed conductances is much less than the measured values. Our model describes each purine as one localized orbital (the purine HOMO). Including more orbitals may increase the calculated conductance. The Landauer approach was successfully used to provide qualitative predictions of molecular conductances, although the numerical conductance values are significantly lower than the measured values.^{6, 62}

3.3 CONCLUSIONS

The most probable molecular conductance of 10-base pair nucleic acid duplexes that have identical nucleobase sequence but different backbones show a 200-fold range. The value of $0.06 G_0$ measured for the aeg-PNA duplex is unprecedented for a molecule that is $\sim 30\text{-\AA}$ long. The aeg-PNA has a high mode conductance that is 13 times higher than that of the corresponding DNA duplex when the linker is propylthiol linker and 34 times higher than the DNA when the linker is amino-C2-thymidine. These findings show that both the linker and the nucleic acid backbone play critical roles in determining the overall magnitude of the measured conductance. Hence, the molecular conductance for these $\sim 30\text{-\AA}$ long nucleic acid duplexes cannot be modeled as an incoherent sum of charge injection, charge transport, and charge escape steps, but must be treated as coherent (or semi-coherent) transport through the molecule.

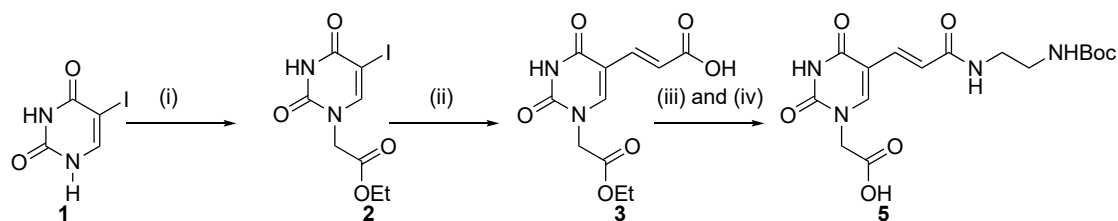
3.4 METHODS

3.4.1 Synthesis of PNA Monomers and Linkers

All reactions were performed under nitrogen atmosphere unless otherwise stated. All commercially available materials were used without further purification unless otherwise specified. Anhydrous solvents, purchased from EMD Millipore, such as dimethylformamide (DMF), dichloromethane (DCM), and tetrahydrofuran (THF), were dried by standard methods and freshly distilled prior to use. All anhydrous reagents were purchased from Aldrich. Common reagents were purchased from either Chem-Impex or Alfa Aesar. ¹H-NMR and ¹³C-NMR spectra were acquired on a Bruker Avance AV-300 or 500 MHz NMR spectrometer.

The thiol linker was introduced at the N-end of PNA oligomers using 4-(tritylthio)butyric acid, which was synthesized by a published procedure,⁶³ S-alkylation of the commercially available trityl mercaptan. The thiol linker was introduced at the C-end of the PNA oligomers using 3-amino-1-propanethiol hydrochloride, which is commercially available.

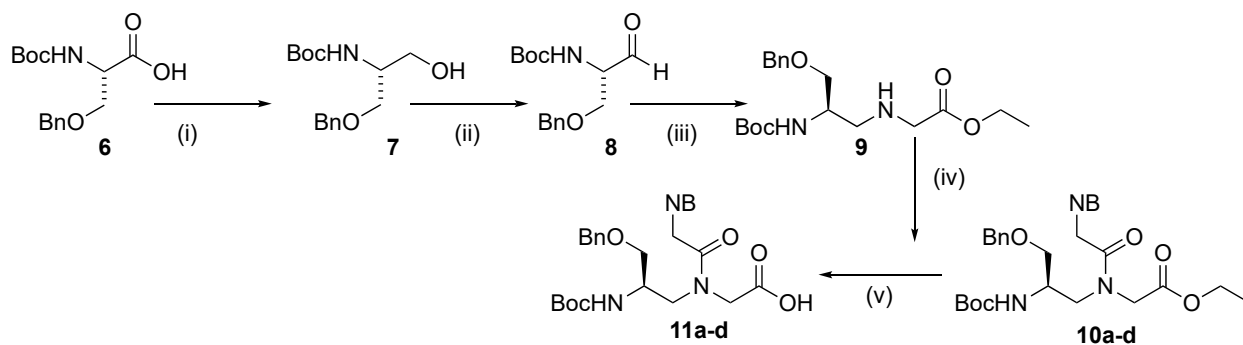
The thymidine 5-C2 amino linker was synthesized using a modified published procedure according to the general Scheme 1.⁶⁴ In step (i), commercially available iodouracil **1** was alkylated at N1 by α -ethyl bromoacetate in the presence of potassium carbonate in anhydrous DMF under nitrogen at room temperature for 24 h to give ethyl ester **2** in quantitative yield. In step (ii), the iodo group of **2** was exchanged with an acryloyl group via a Heck reaction with acrylic acid to give the carboxylic acid **3** in 60 % yield. In step (iii), coupling of the carboxylic acid **3** with Boc-protected ethylenediamine was accomplished by activation with HATU in the presence of DIEA in anhydrous DMF. Hydrolysis of the resulting ethyl ester to carboxylic acid using LiOH led to the final product **5** in 75% yield over last two steps. Details of the synthesis are given in the Supporting Information.



Scheme 3.1. (i) K_2CO_3 , DMF, α -bromo ethyl acetate, DMF, $0^\circ C$ to room temperature, 24 h, quantitative yield; (ii) $Pd(OAc)_2$, Bu_4NBr , DMF/DIE/ H_2O , acrylic acid, $80-90^\circ C$, 16h, 60%; (iii) $BocNH(CH_2)_2NH_2 \cdot HCl$, HATU, DIEA, DMF, $0^\circ C$ to room temperature, 12 h; (iv) $LiOH$, THF, $0^\circ C$ to rt, 12 h, 75%.

3.4.2 Synthesis of L S- γ PNA Monomers

Boc-protected L S- γ PNA monomers were synthesized by adapting the procedures described by Ly et al. (Scheme 2).¹⁸ In order to increase the reaction yield some modifications have been made on the first two steps and the last step of the reaction scheme. Specifically, instead of amidation of the Boc-protected L-serine **6** using *N,O*-dimethylhydroxylamine hydrochloride, the carboxylic end of compound **6** was reduced to its alcohol derivative **7** in the presence of *i*-butylchloroformate (IBCF), *N*-methyl morpholine (NMP), and sodium borohydride. The alcohol derivative **7** was converted to aldehyde **8** via Swern oxidation using oxalyl chloride, dimethylsulfoxide, and triethyl amine. The reaction yield was almost quantitative. The Swern oxidation provides the product monomers in higher purity than the previously published procedure and eliminates the use of the expensive reagent $CH_3NHOCH_3 \cdot HCl$. Reductive amination of intermediate **8** with ethyl ester glycine gave Aeg-backbone **9** with 40 % yield. Coupling of the aeg-backbone with the corresponding nucleobases followed by hydrolysis led the γ -modified monomers **10a-d**.



Scheme 3.2. Synthesis of γ -serine modified PNA monomers (i) NMM, ClCO₂i-Bu, DME, NaBH₄, quantitative Yield (ii) DMSO, (COCl)₂, Et₃N, DCM, N₂, -78°C, % 95 (iii) ethyl ester glycine, MeOH, 4 °C, 4 h, then AcOH, NaBH(OAc)₃, 30 min., % 40, (iv) carboxymethylnucleobase (B: A, G, C, T), DCC, DhbtOH, DMF, 40°C, 24 h, %39-63 (v) NaOH/THF (1:1), 30 min., 0°C. %76-96.

3.4.3 Synthesis of PNA Oligomers

Boc/Z-protected and Fmoc/Bhoc PNA monomers were purchased from PolyOrg Inc and ASM Research Chemicals and used without further purification. The oligomers were purified using reversed-phase HPLC and characterized by MALDI-TOF. All PNA solutions were prepared in nanopure water.

The PNA oligomers containing thymidine 5-C2 amino [T_(C2-NH₂)] were synthesized manually on Rink-amide AM resin purchased from Novabiochem following the standard Fmoc procedures of solid-phase peptide synthesis. T_(C2-NH₂) acetic acid linker was added on the N-end of a PNA oligomer as the side chain of the Boc-DAP(Fmoc)-OH (Boc-3-(Fmoc-amino)-L-alanine) amino acid which was purchased from Sigma-Aldrich. The PNA oligomers were cleaved from the resin using TFA/DCM/TIS (10:85:5) for 30 min. The deprotection of side chain was effected by 50% TFA-DCM (TIS used as scavenger) for 1 h.

The PNA oligomers containing a C-end thiol linker were synthesized using 2-chlorotriptyl resin downloaded with 3-Amino-1-propanethiol hydrochloride by a published protocol⁶⁵ using Fmoc strategy. The PNA oligomers with an N-end thiol linker were synthesized on MBHA resin (purchased from Peptides International) using a Boc strategy. The PNA was cleaved using

TFMSA/TFA/m-cresol/thioanisole (20:60:10:10) and TFA/triisopropylsilane/water (95:2.5:2.5) for Boc and Fmoc strategy, respectively.

^LS-PNA oligomers were synthesized manually on methyl benzhydryl amine (MBHA) resin by standard Boc-solid phase synthesis method. Further details and characterization of the oligomers are provided in the Supporting Information.

3.4.4 Preparation of Samples for Conductance Measurements

3.4.4.1 Nucleic Acid Duplexes

The DNA strands were purchased from Integrated DNA Technologies or Alpha DNA, and the PNA strands were synthesized by the aforementioned procedure. Duplexes were hybridized by heating a solution containing 20 μ M of each nucleic acid strand in a pH = 7.0 Tris-EDTA buffer and 50 mM NaCl. The solution was heated to 90 °C for 10 minutes and then allowed to cool back to room temperature over 2-3 hours. This procedure yields duplexes and was confirmed by absorbance and circular dichroism spectroscopy.

3.4.4.2 Gold Substrates

Ultraflat gold substrates were prepared using the template-stripping process.⁶⁶ 100 nm gold films were evaporated onto freshly-cleaved mica (AJA ATC-T Series Thermal Evaporation System). Piranha-cleaned glass slips (10 mm x 25 mm) were affixed to the gold films and peeled off to transfer the gold to the slips prior to each experiment. The atomically flat gold substrates were coated with the solution containing hybridized strands for roughly 10 seconds and then washed with water, washed with ethanol, and dried under an argon stream. The duplexes bind to the gold substrates via the terminal linker groups and remain on the substrate following washing and drying.

3.4.5 Conductance Measurements and Analysis

All measurements were performed using an Agilent 5500 Scanning Probe Microscope system equipped with an environmental chamber. The chamber was housed in a homemade acoustically isolated Faraday cage seated on an anti-vibrational system (Table Stable) that was mounted on an optical table. Data collection was performed using a modified version of the STM-controlled break junction method.³⁶⁻³⁷ An STM tip was repeatedly driven to the surface of the gold substrates and withdrawn at a constant speed of 10 nm s^{-1} . During the retraction period, molecular junctions can form as molecules bridge the gap between the gold substrate and the gold tip. Thousands of trajectories were collected for each duplex, requiring multiple substrates and STM tips to collect a full set. The gold STM tips (0.25 mm, 99.95% gold wire, Alfa Aesar) were freshly cut prior to each experiment. All experiments were performed under an argon atmosphere and the substrates were immersed in mesitylene. The applied bias was a triangular waveform with a modulation frequency of 500 Hz (Stanford Research Systems, DS345 Function Generator). A bias of $50 \pm 50 \text{ mV}$ was applied in the measurement of every duplex with the exception of the aeg-PNA/aeg-PNA duplex with amine linkers; for these measurements, the applied bias was $5 \pm 5 \text{ mV}$. All measurements were performed using a 10 nA/V preamplifier.

Data filtering and analysis were performed using a custom Matlab code. The current-distance trajectories were filtered to remove trajectories that did not display molecular junctions. The trajectories were partitioned into periods established by the applied bias and fit to current responses generated using a library of resistance values based on a previous protocol.³⁷ For certain duplexes, multiple bias ranges were used to ensure that the highest conductance mode was observable in each instance.

3.4.6 Molecular Dynamics

The initial structures of DNA are obtained with an x3DNA webserver⁶¹. PNA structures for this sequence were generated by a custom program. The γ -PNA structures were assembled by replacing the H2'' atom on the PNA structures backbone with a C atom. The CHARMM force field⁶⁷ was used and CGenFF⁶⁸ was used to find force field parameters for the amine linker. DNA/aeg-PNA was built in GaussView,⁶⁹ starting from PDB:1PDT.²³

For each structure, multiple MD simulations were performed and snapshots were taken at 1frame/ps. Two nucleobases (donor and acceptor bases in coupling calculations) are extracted from each snapshot. Backbones, solvent molecules, and counter-ions are removed. Hydrogen atoms are patched to dangling bonds.²⁶ Coupling calculations were performed with the block diagonalization method⁷⁰ based on the Fock matrix obtained from the ZINDO semi-empirical quantum method embedded in Gaussian 09.⁴⁹

3.4.7 Conductance Calculations

To explore the conductivity of the nucleic acids, we used a Büttiker-Landauer model,⁷¹ where the Büttiker probes perturb the coherence and introduce an incoherent charge transfer mechanism. The Büttiker-Landauer model is widely used to simulate molecular junction conductance.⁷²⁻⁷⁴ Because the measured conductance arises mainly from hole transfer in our experiments³²⁻³³ and hole transfer is dominantly mediated by purine bases, we only consider purine bases (guanine and adenine) in our model.

In our model, the site energy of guanine (HOMO) is 0.35 eV higher than the site energy of adenine (HOMO).⁹ The Fermi level of the Au electrodes was placed 0.8 eV higher in energy than the guanine HOMO.⁷⁵ The electronic coupling between nearest neighbor purine sites $V_{i,i+1}$ was

obtained from quantum calculations and averaged from 1000 MD snapshots. The coupling calculations for all species are given in Table B9 in the Supporting Information.

3.5 REFERENCES

1. Rothmund, P. W. K., *Nature* **2006**, *440*, 297-302.
2. Pinheiro, A. V.; Han, D.; Shih, W. M.; Yan, H., *Nat. Nanotechnol.* **2011**, *6*, 763-72.
3. Le, J. D.; Pinto, Y.; Seeman, N. C.; Musier-Forsyth, K.; Taton, T. A.; Kiehl, R. A., *Nano Lett.* **2004**, *4*, 2343-2347.
4. Renaud, N.; Harris, M. A.; Singh, A. P.; Berlin, Y. A.; Ratner, M. A.; Wasielewski, M. R.; Lewis, F. D.; Grozema, F. C., *Nat. Chem.* **2016**, *8*, 1015-1021.
5. Paul, A.; Watson, R. M.; Wierzbinski, E.; Davis, K. L.; Sha, A.; Achim, C.; Waldeck, D. H., *J. Phys. Chem. B* **2010**, *114*, 14140-14148.
6. Venkatramani, R.; Davis, K. L.; Wierzbinski, E.; Bezer, S.; Balaeff, A.; Keinan, S.; Paul, A.; Kocsis, L.; Beratan, D. N.; Achim, C.; Waldeck, D. H., *J. Am. Chem. Soc.* **2011**, *133*, 62-72.
7. Beratan, D. N.; Waldeck, D. H., *Nat. Chem.* **2016**, *8*, 992-993.
8. Lu, Q.; Liu, K.; Zhang, H.; Du, Z.; Wang, X.; Wang, F., *ACS Nano* **2009**, *3*, 3861-8.
9. Zhang, Y.; Liu, C.; Balaeff, A.; Skourtis, S. S.; Beratan, D. N., *Proc. Natl. Acad. Sci. U.S.A.* **2014**, *111*, 10049-10054.
10. Li, Y.; Artés, J. M.; Hihath, J., *Small* **2016**, *12*, 432-437.
11. Artes, J. M.; Li, Y.; Qi, J.; Anantram, M. P.; Hihath, J., *Nat. Commun.* **2015**, *6*, 8870.
12. Bag, S.; Mogurampelly, S.; Goddard Iii, W. A.; Maiti, P. K., *Nanoscale* **2016**, *8*, 16044-52.
13. Wang, K.; Hamill, J. M.; Wang, B.; Guo, C. L.; Jiang, S. B.; Huang, Z.; Xu, B. Q., *Chem. Sci.* **2014**, *5*, 3425-3431.
14. Guo, C.; Wang, K.; Zerah-Harush, E.; Hamill, J.; Wang, B.; Dubi, Y.; Xu, B., *Nat. Chem.* **2016**, *8*, 484-490.
15. Wierzbinski, E.; de Leon, A.; Davis, K. L.; Bezer, S.; Wolak, M. A.; Kofke, M. J.; Schlaf, R.; Achim, C.; Waldeck, D. H., *Langmuir* **2012**, *28*, 1971-1981.
16. Liu, S.; Clever, G. H.; Takezawa, Y.; Kaneko, M.; Tanaka, K.; Guo, X.; Shionoya, M., *Angew. Chem. Int. Ed.* **2011**, *50*, 8886-8890.
17. Egholm, M.; Buchardt, O.; Nielsen, P. E.; Berg, R. H., *J. Am. Chem. Soc.* **1992**, *114*, 1895-1897.
18. Dragulescu-Andrasi, A.; Rapireddy, S.; Frezza, B. M.; Gayathri, C.; Gil, R. R.; Ly, D. H., *J. Am. Chem. Soc.* **2006**, *128*, 10258-67.
19. Rasmussen, H.; Kastrop, J. S.; Nielsen, J. N.; Nielsen, J. M.; Nielsen, P. E., *Nat. Struct. Biol.* **1997**, *4*, 98-101.
20. He, W.; Crawford, M. J.; Rapireddy, S.; Madrid, M.; Gil, R. R.; Ly, D. H.; Achim, C., *Mol. Biosyst.* **2010**, *6*, 1619-29.
21. He, W.; Hatcher, E.; Balaeff, A.; Beratan, D. N.; Gil, R. R.; Madrid, M.; Achim, C., *J. Am. Chem. Soc.* **2008**, *130*, 13264-73.
22. Watson, J. D.; Crick, F. H., *Nature* **1953**, *171*, 737-8.
23. Eriksson, M.; Nielsen, P. E., *Nat. Struct. Mol. Biol.* **1996**, *3*, 410-413.

24. Yeh, J. I.; Shivachev, B.; Rapireddy, S.; Crawford, M. J.; Gil, R. R.; Du, S.; Madrid, M.; Ly, D. H., *J. Am. Chem. Soc.* **2010**, *132*, 10717-10727.
25. Brown, S.; Thomson, S.; Veal, J.; Davis, D., *Science* **1994**, *265*, 777-780.
26. Hatcher, E.; Balaeff, A.; Keinan, S.; Venkatramani, R.; Beratan, D. N., *J. Am. Chem. Soc.* **2008**, *130*, 11752-61.
27. Wierzbinski, E.; de Leon, A.; Yin, X.; Balaeff, A.; Davis, K. L.; Rapireddy, S.; Venkatramani, R.; Keinan, S.; Ly, D. H.; Madrid, M.; Beratan, D. N.; Achim, C.; Waldeck, D. H., *J. Am. Chem. Soc.* **2012**, *134*, 9335-9342.
28. O'Neill, M. A.; Barton, J. K., *J. Am. Chem. Soc.* **2004**, *126*, 11471-83.
29. Thazhathveetil, A. K.; Vura-Weis, J.; Trifonov, A.; Wasielewski, M. R.; Lewis, F. D., *J. Am. Chem. Soc.* **2012**, *134*, 16434-40.
30. O'Neill, M. A.; Barton, J. K., *J. Am. Chem. Soc.* **2004**, *126*, 13234-5.
31. Wierzbinski, E.; Venkatramani, R.; Davis, K. L.; Bezer, S.; Kong, J.; Xing, Y.; Borguet, E.; Achim, C.; Beratan, D. N.; Waldeck, D. H., *ACS Nano* **2013**, *7*, 5391-5401.
32. Xiang, L.; Palma, J. L.; Bruot, C.; Mujica, V.; Ratner, M. A.; Tao, N., *Nat. Chem.* **2015**, *7*, 221-226.
33. Liu, C.; Xiang, L.; Zhang, Y.; Zhang, P.; Beratan, D. N.; Li, Y.; Tao, N., *Nat. Chem.* **2016**, *8*, 941-945.
34. Yin, X.; Wierzbinski, E.; Lu, H.; Bezer, S.; de Leon, A. R.; Davis, K. L.; Achim, C.; Waldeck, D. H., *J. Phys. Chem. A* **2014**, *118*, 7579-89.
35. Beratan, D.; Betts, J.; Onuchic, J., *Science (Washington, DC, U. S.)* **1991**, *252*, 1285-1288.
36. Xu, B.; Tao, N. J., *Science (Washington, DC, U. S.)* **2003**, *301*, 1221-1223.
37. Beall, E.; Yin, X.; Waldeck, D. H.; Wierzbinski, E., *Nanoscale* **2015**, *7*, 14965-14973.
38. Li, C.; Pobelov, I.; Wandlowski, T.; Bagrets, A.; Arnold, A.; Evers, F., *J. Am. Chem. Soc.* **2008**, *130*, 318-326.
39. Wierzbinski, E.; Arndt, J.; Hammond, W.; Slowinski, K., *Langmuir* **2006**, *22*, 2426-2429.
40. Bruot, C.; Xiang, L.; Palma, J. L.; Tao, N., *ACS Nano* **2015**, *9*, 88-94.
41. Guo, X.; Gorodetsky, A. A.; Hone, J.; Barton, J. K.; Nuckolls, C., *Nat. Nanotechnol.* **2008**, *3*, 163-167.
42. Noguez, C.; Cohen, S. R.; Daube, S.; Apter, N.; Naaman, R., *J. Phys. Chem. B* **2006**, *110*, 8910-8913.
43. Haiss, W.; Martín, S.; Leary, E.; Zalinge, H. v.; Higgins, S. J.; Bouffier, L.; Nichols, R. J., *J. Phys. Chem. C* **2009**, *113*, 5823-5833.
44. van Wees, B. J.; van Houten, H.; Beenakker, C. W.; Williamson, J. G.; Kouwenhoven, L. P.; van der Marel, D.; Foxon, C. T., *Phys. Rev. Lett.* **1988**, *60*, 848-850.
45. Xu, B. Q.; Zhang, P. M.; Li, X. L.; Tao, N. J., *Nano Lett.* **2004**, *4*, 1105-1108.
46. van Zalinge, H.; Schiffrin, D. J.; Bates, A. D.; Haiss, W.; Ulstrup, J.; Nichols, R. J., *ChemPhysChem* **2006**, *7*, 94-98.
47. Chen, W.; Widawsky, J. R.; Vázquez, H.; Schneebeli, S. T.; Hybertsen, M. S.; Breslow, R.; Venkataraman, L., *J. Am. Chem. Soc.* **2011**, *133*, 17160-17163.
48. Yelin, T.; Korytar, R.; Sukenik, N.; Vardimon, R.; Kumar, B.; Nuckolls, C.; Evers, F.; Tal, O., *Nat. Mater.* **2016**, *15*, 444-449.
49. Frisch, M. J.; Trucks, G. W.; Schlegel, H. B.; Scuseria, G. E.; Robb, M. A.; Cheeseman, J. R.; Scalmani, G.; Barone, V.; Mennucci, B.; Petersson, G. A.; Nakatsuji, H.; Caricato, M.; Li, X.; Hratchian, H. P.; Izmaylov, A. F.; Bloino, J.; Zheng, G.; Sonnenberg, J. L.;

- Hada, M.; Ehara, M.; Toyota, K.; Fukuda, R.; Hasegawa, J.; Ishida, M.; Nakajima, T.; Honda, Y.; Kitao, O.; Nakai, H.; Vreven, T.; Montgomery, J. A.; Peralta, J. E.; Ogliaro, F.; Bearpark, M.; Heyd, J. J.; Brothers, E.; Kudin, K. N.; Staroverov, V. N.; Kobayashi, R.; Normand, J.; Raghavachari, K.; Rendell, A.; Burant, J. C.; Iyengar, S. S.; Tomasi, J.; Cossi, M.; Rega, N.; Millam, J. M.; Klene, M.; Knox, J. E.; Cross, J. B.; Bakken, V.; Adamo, C.; Jaramillo, J.; Gomperts, R.; Stratmann, R. E.; Yazyev, O.; Austin, A. J.; Cammi, R.; Pomelli, C.; Ochterski, J. W.; Martin, R. L.; Morokuma, K.; Zakrzewski, V. G.; Voth, G. A.; Salvador, P.; Dannenberg, J. J.; Dapprich, S.; Daniels, A. D.; Farkas, Foresman, J. B.; Ortiz, J. V.; Cioslowski, J.; Fox, D. J., Gaussian 09, Revision B.01. Wallingford CT, 2009.
50. Venkatramani, R.; Wierzbinski, E.; Waldeck, D. H.; Beratan, D. N., *Faraday Discuss.* **2014**, *174*, 57-78.
 51. Büttiker, M., *Phys. Rev. B* **1985**, *32*, 1846-1849.
 52. Büttiker, M., *Phys. Rev. B* **1986**, *33*, 3020-3026.
 53. Ashkenazi, G.; Kosloff, R.; Ratner, M. A., *J. Am. Chem. Soc.* **1999**, *121*, 3386-3395.
 54. Goldsmith, R. H.; Wasielewski, M. R.; Ratner, M. A., *J. Phys. Chem. B* **2006**, *110*, 20258-20262.
 55. Weiss, E. A.; Katz, G.; Goldsmith, R. H.; Wasielewski, M. R.; Ratner, M. A.; Kosloff, R.; Nitzan, A., *J. Chem. Phys.* **2006**, *124*, 074501.
 56. Chin, A. W.; Datta, A.; Caruso, F.; Huelga, S. F.; Plenio, M. B., *New J. Phys.* **2010**, *12*, 065002.
 57. Plenio, M. B.; Huelga, S. F., *New J. Phys.* **2008**, *10*, 113019.
 58. Patrick, R.; Masoud, M.; Ivan, K.; Seth, L.; Alán, A.-G., *New J. Phys.* **2009**, *11*, 033003.
 59. Liu, C.; Beratan, D. N.; Zhang, P., *J. Phys. Chem. B* **2016**, *120*, 3624-3633.
 60. Weiss, U., *Quantum Dissipative Systems*. World Scientific: Singapore, 1999.
 61. Lu, X.-J.; Olson, W. K., *Nucleic Acids Res.* **2003**, *31*, 5108-5121.
 62. Xing, Y.; Park, T.-H.; Venkatramani, R.; Keinan, S.; Beratan, D. N.; Therien, M. J.; Borguet, E., *J. Am. Chem. Soc.* **2010**, *132*, 7946-7956.
 63. Qvit, N.; Reuveni, H.; Gazal, S.; Zundevich, A.; Blum, G.; Niv, M. Y.; Feldstein, A.; Meushar, S.; Shalev, D. E.; Friedler, A.; Gilon, C., *J. Comb. Chem.* **2008**, *10*, 256-66.
 64. Oquare, B. Y.; Taylor, J. S., *Bioconjug. Chem.* **2008**, *19*, 2196-204.
 65. Mourtas, S.; Katakalous, C.; Nicolettou, A.; Tzavara, C.; Gatos, D.; Barlos, K., *Tetrahedron Lett.* **2003**, *44*, 179-182.
 66. Hegner, M.; Wagner, P.; Semenza, G., *Surf. Sci.* **1993**, *291*, 39-46.
 67. MacKerell, A. D.; Bashford, D.; Bellott, M.; Dunbrack, R. L.; Evanseck, J. D.; Field, M. J.; Fischer, S.; Gao, J.; Guo, H.; Ha, S.; Joseph-McCarthy, D.; Kuchnir, L.; Kuczera, K.; Lau, F. T. K.; Mattos, C.; Michnick, S.; Ngo, T.; Nguyen, D. T.; Prodhom, B.; Reiher, W. E.; Roux, B.; Schlenkrich, M.; Smith, J. C.; Stote, R.; Straub, J.; Watanabe, M.; Wiórkiewicz-Kuczera, J.; Yin, D.; Karplus, M., *J. Phys. Chem. C* **1998**, *102*, 3586-3616.
 68. Vanommeslaeghe, K.; Hatcher, E.; Acharya, C.; Kundu, S.; Zhong, S.; Shim, J.; Darian, E.; Guvench, O.; Lopes, P.; Vorobyov, I.; MacKerell, A. D., *J. Comput. Chem.* **2010**, *31*, 671-690.
 69. Dennington, R.; Keith, T. A.; Millam, J. M., GaussView, Version 6, Semichem Inc., Shawnee Mission, KS, **2016**.
 70. Scholes, G. D., *Annu. Rev. Phys. Chem.* **2003**, *54*, 57-87.
 71. Qi, J.; Edirisinghe, N.; Rabbani, M. G.; Anantram, M. P., *Phys. Rev. B* **2013**, *87*, 085404.

72. Korol, R.; Kilgour, M.; Segal, D., *J. Chem. Phys.* **2016**, *145*, 224702.
73. Kilgour, M.; Segal, D., *J. Phys. Chem. C* **2015**, *119*, 25291-25297.
74. Kilgour, M.; Segal, D., *J. Chem. Phys.* **2015**, *143*, 024111.
75. Paul, A.; Bezer, S.; Venkatramani, R.; Kocsis, L.; Wierzbinski, E.; Balaeff, A.; Keinan, S.; Beratan, D. N.; Achim, C.; Waldeck, D. H., *J. Am. Chem. Soc.* **2009**, *131*, 6498-6507.

4.0 THE MOLECULAR CONDUCTANCE OF NICKED NUCLEIC ACID DUPLEXES

This work was published as Beall, E.; Sargun, A.; Ulku, S.; Bae, Y.; Wierzbinski, E.; Clever, C.; Waldeck, D. H.; Achim, C., Molecular Conductance of Nicked Nucleic Acid Duplexes. *J. Phys. Chem. C* **2018**, *122*, 7533-7540. The author of the dissertation performed the conductance measurements, subsequent analyses, and prepared the manuscript. The author of the dissertation was the first author. The supporting information for this chapter can be found in Appendix C.

This work investigates how the conductance of a nucleic acid duplex with a ‘nick’ in its backbone compares with that of a duplex with a fully covalent backbone. Statistical analyses of the single-molecule conductance properties reveal that molecular junctions with a nicked duplex have an average conductance close to that found for non-nicked structures but exhibit greater variability in the molecular conductance. This effect is shown for both DNA homoduplexes and DNA/PNA heteroduplexes, with the heteroduplexes showing a greater average molecular conductance and a smaller degree of variability. The average molecular conductance of the heteroduplexes is also shown to be affected by their PNA content; the duplexes’ conductance increases as the ratio of PNA-to-DNA increases. These observations suggest that the charge transfer properties of nucleic acid-based assemblies can support complex functions.

4.1 INTRODUCTION

Since its inception,¹ molecular electronics has advanced to experimental realizations of molecules which display a current-voltage behavior similar to that in an electronic device, ranging from single molecule diodes to the use of a protein as a transistor.²⁻³ Driven by advancements in the fundamental understanding of charge transport through single molecules and larger biological systems,⁴⁻⁷ efforts are being directed to the construction of increasingly intricate, functional biomimetic structures.⁸⁻⁹ Moreover, the promise of nucleic acid-based architectures to affect biochemical transformations and to function as logic and circuit elements is progressively bridging the gap between concept and device realization.¹⁰⁻¹¹ Schemes for assembling conductive nucleic acid platforms capable of providing long-range electrical communication are emerging and being explored. Studies of the mechanism of charge transfer in these systems continues to challenge our understanding and require new models to account for the important roles of molecular flexibility and molecule-bath coupling.¹²⁻¹⁷

Self-assembly of DNA tiles and DNA origami into one-, two-, and three-dimensional structures rests on combining short and long oligonucleotides as building blocks.¹⁸⁻²⁰ Consequently, these structures contain nicks, i.e. breaks in the backbone of the DNA at the junction between different oligonucleotides. The question arises whether and how these nicks affect charge transport through DNA in nanostructures. This question has been partially addressed by electron transfer studies of DNA duplexes. In a study by Lewis et al., the photo-induced electron transfer from an electron donor to an electron acceptor via a nicked DNA duplex was measured and compared to a DNA duplex with an intact backbone.²¹ This study showed that the rate constant for charge separation was not appreciably affected by the nick in the backbone of the duplex. In another study, Barton et al. measured the electron transfer to a redox probe which was tethered to

an electrode by a nicked DNA duplex and found that its efficiency was indistinguishable from electron transfer through a full DNA duplex (i.e., without a ‘nick’ in the backbone of the same length).²² This behavior was observed even for duplexes that contained multiple nicks.

To understand the relationship between the electron transfer rate and the single-molecule conductance, researchers have compared the values of the electron transfer rate and molecular conductance for systems with different composition and molecular lengths.²³⁻²⁶ They determined that a power law correlates the electron transfer rate and single-molecule conductance for molecular bridges. Given this correlation and the fact that the electron transfer rate is not affected by the presence of a nick in the backbone of DNA duplexes, we anticipate that the molecular conductance of nucleic acid constructs should be independent of the presence of a nick.

In this paper, we report the results of a project that aimed to test the hypothesis that a single nick does not affect the molecular conductance significantly. We examined the effect of a nick on the single-molecule conductance of nucleic acid duplexes with different backbone composition, namely DNA homoduplexes and DNA/PNA heteroduplexes. PNA is a synthetic analogue of DNA that has a backbone based on N-(2-aminoethyl)glycine instead of the phosphodiester backbone of DNA.²⁷ The single-molecule conductance of the full and nicked nucleic acid duplexes were measured, and a statistical analysis was employed to assess the stability and variability of the molecular junctions between the STM tip and the substrate.

Figure 4.1 shows the architecture of the full and nicked duplexes that were studied. The full duplexes are formed by the hybridization of two 20-base nucleic acid strands. The nicked duplexes have two 10-base strands that are hybridized to a 20-base template strand. In previous work we showed that the molecular conductance of 10-base pair (bp) PNA duplexes is over ten times larger than that of DNA homoduplexes and DNA/PNA heteroduplexes with the same sequence.¹⁷ The

duplex sequence used in that study was GCATGTTTGA (and its complement). The same 10-bp sequence is used as the ‘a’ section of the 20-bp duplex sequence reported here (see Figure 4.1). We measure and compare the conductance for full and nicked versions of 20-bp DNA and PNA homoduplexes and 20-bp DNA/PNA heteroduplexes. In addition, these new data are compared with the earlier published data to ascertain how the conductance changes with the length of the duplexes.

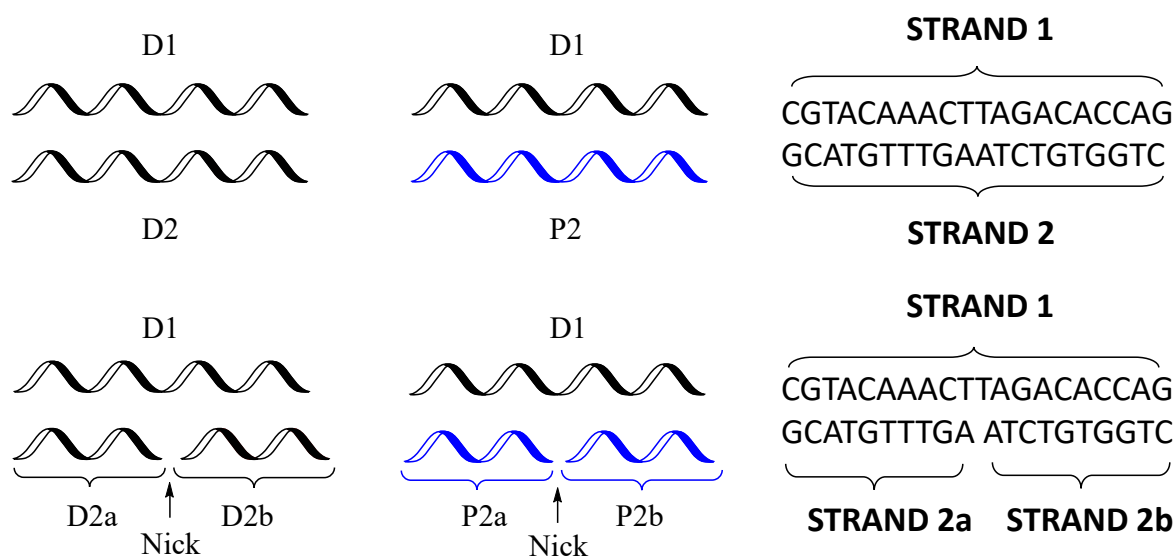


Figure 4.1. The architectures of the full and nicked DNA homoduplexes and DNA/PNA heteroduplexes. The sequence of the top strand of each duplex is written in the 5’-to-3’ direction for DNA and N-to-C direction for PNA. PNA strands (P) are shown in blue. DNA strands (D) are shown in black.

4.2 RESULTS

4.2.1 Characterization of the Nucleic Acids

The 10- and 20-bp homoduplexes of DNA and hetero-duplexes of DNA/PNA were characterized by UV-Vis absorbance, circular dichroism, and fluorescence spectroscopies. These measurements provide information on the thermal stability and chirality of the full and nicked

duplexes and allow us to conclude that both 10-base nucleic acid strands are present when templated with the 20-bp nucleic acid strand into a duplex.

4.2.1.1 Melting Curves

The ‘nick’ in the backbone significantly destabilizes the homo- DNA and hetero- DNA/PNA duplexes. Tables 4.1 and C.3 contain the T_m values for the full and nicked DNA and DNA/PNA duplexes, and Figure C.1 shows typical UV melting data. The data show that the ‘nicked’ DNA homoduplex (D1D2aD2b) and the ‘nicked’ DNA/PNA heteroduplex (D1P2aP2b) are significantly less stable than their full versions (D1D2 and D1P2), with ΔT_m being more than 18°C. The melting temperatures indicate that the PNA homoduplexes are more stable than the DNA/PNA heteroduplexes, which in turn are more stable than the DNA homoduplexes. These differences are consistent with previous reports.²⁸ The melting temperature of the nicked 20-bp DNA/PNA duplexes is higher than that of 10-bp DNA/PNA duplexes, as one would expect given the length of these duplexes.¹⁷

Table 4.1. Melting Temperatures (T_m) of Nucleic Acid Duplexes.

	Chemical Nature of Strands	$T_m/^\circ\text{C}$
Full duplex	P1/P2	>90
	D1/D2	45
	D1/P2	85
Nicked duplex	D1/D2a/D2b	21
	D1/P2a/P2b	67
	P1/P2a/D2b	68

4.2.1.2 Circular Dichroism Spectra

Figure 4.2 shows the circular dichroism (CD) spectra for the full and nicked DNA homoduplexes and DNA/PNA heteroduplexes. The spectra of the DNA/PNA heteroduplexes show the biphasic exciton coupling pattern characteristic of a right-handed helix. The signal intensity

for the nicked duplexes is similar to that of the full duplexes, which indicates that the nick does not affect the structure of the duplex.

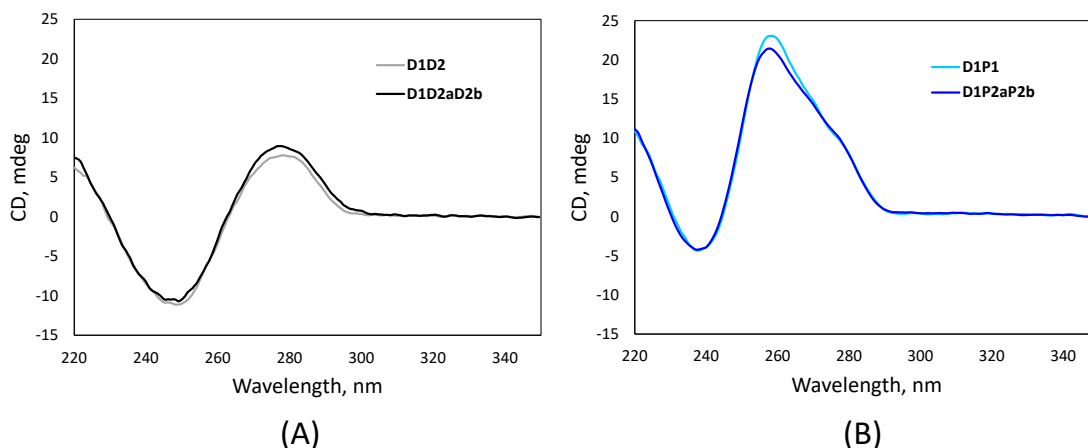


Figure 4.2. The circular dichroism spectra for the full and nicked DNA homoduplexes (A) and the full and nicked DNA/PNA heteroduplexes (B).

4.2.1.3 Fluorescence Spectra for the DNA/PNA Heteroduplexes

The ratio of the intensity of the excimer emission (PL₄₈₀) to the pyrene monomer emission intensity (PL₄₀₀) was used to assess whether both 10-base PNA strands are bound to the template in the nicked 20-bp DNA/PNA heteroduplex and 20-bp PNA homoduplex. This method is based on the fact that when two pyrene moieties are in close proximity of each other, π -stacking can occur and excimer emission can be observed at $\lambda_{\text{max}} = 480 \text{ nm}$.²⁹ Figure 4.3A shows the location of the pyrene in the nicked PNA/DNA duplexes. Figure 4.3B shows the fluorescence spectra for the three schemes of the DNA/PNA heteroduplexes. Based on the number of pairs of adjacent pyrenes and of isolated pyrenes in the different motifs, the PL₄₈₀/PL₄₀₀ ratio should decrease in the order Scheme 1 > Scheme 2 ~ Scheme 3. Indeed, this trend is displayed by the fluorescence spectra (see Figure 4.3B), which show a PL₄₈₀/PL₄₀₀ ratio of 5.3, 1.6, and 2.4 for Schemes 1, 2, and 3,

respectively. This result substantiates the presence of the three strands D1, P2a, and P2b in the nicked DNA/PNA heteroduplexes.

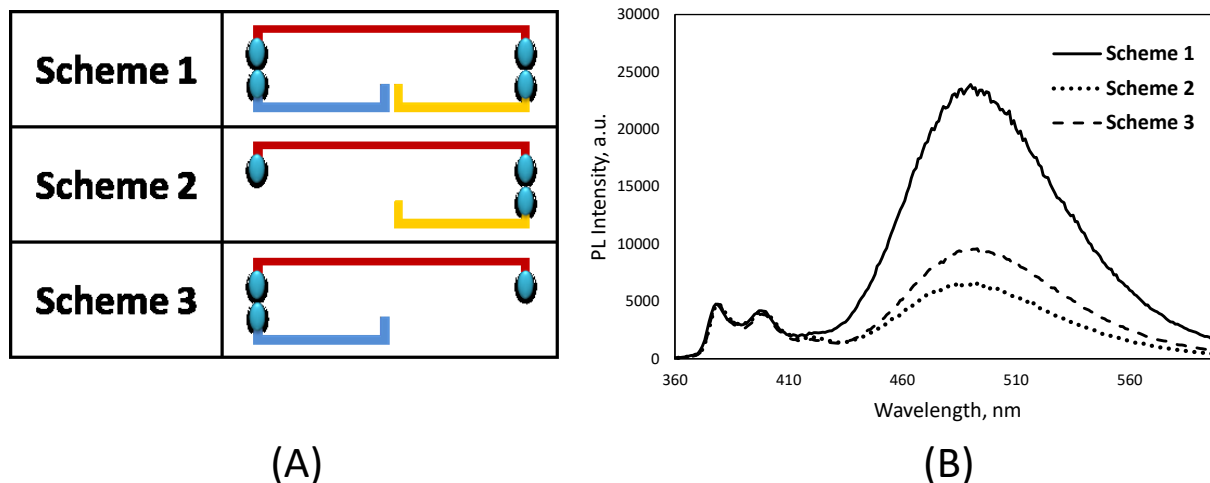


Figure 4.3. (A) Three pyrene labeling schemes for the duplexes. The red lines represent the 20-base DNA template strand. The blue and yellow lines represent the 10-base PNA strands. The blue ellipses represent the pyrenes. (B) The fluorescence spectra for pyrene-labelled DNA/PNA heteroduplexes. The solid, dotted, and dashed lines correspond to Schemes 1, 2, and 3, respectively. The data have been scaled to have equivalent intensity at $\lambda = 400$ nm.

4.2.2 The Effect of the Nick on the Conductance of the Duplexes

Single molecule conductance measurements were performed on 20-bp duplexes using the scanning tunneling microscope break junction (STM-BJ) method with a continuous bias modulation.^{17, 30-31} Propylthiol (PT) units were introduced at the two termini of the DNA and DNA/PNA duplexes to facilitate the formation of thiol linkages to the Au surfaces. In the conductance measurement, a gold STM tip is driven to the surface of a gold substrate, which is covered by a diffuse layer of the nucleic acid duplexes. Molecular junctions can form between the gold substrate and STM tip via thiol linkers on opposing strands of a duplex. As the STM tip is retracted from the surface, a triangular waveform bias voltage is applied across the gap and the

current between the substrate and the tip is measured. This process provides a time profile of the current, which is converted to a distance.

Thousands of current responses, or trajectories, are collected for each duplex type and filtered to remove trajectories that do not contain a molecular junction. The filtered set provides a distribution of current responses that is analyzed and converted into conductance histograms. The discretized manner in which the bias is applied causes the current responses to be discretized. An example of the discretization of a current-time response for a DNA homoduplex is shown in Figure 4.4A. The trajectories are partitioned by the periods of the modulated current response and each period is indexed. The periods in the current response are fitted and every fitted period has an associated conductance value, $G(n)$, where the index, n , identifies the period number.

Panels B and E of Figure 4.4 show conductance histograms for the full DNA homoduplex, the full DNA/PNA heteroduplex, the nicked DNA duplex, and the nicked DNA/PNA duplex. On the abscissa, the conductance is scaled by $G_0 = 2e^2/h = 77.5 \mu\text{S}$, the quantum of conductance.³² Each duplex shows a peak corresponding to the most probable molecular conductance and a smaller, second peak at a conductance of twice the value of the first peak. In each case, the histogram was fit by two gaussian functions to extract the most probable conductance (see Figure C.3). The peak at twice the conductance value was assigned to molecular junctions involving two molecules bound across the gap. Figures 4.4C through 4.4G show conductance histograms as a function of the period number of the trajectory. The conductance for the full DNA duplex remains the same for more periods (Figure 4.4C), as compared to the nicked version (Figure 4.4D). The heteroduplexes show less of a difference in conductance and have a behavior more like that of the full DNA duplex (Figures 4.4F and 4.4G), implying that their integrity is better preserved.

The full 20-bp DNA homoduplex has a most probable conductance of $5.5 \times 10^{-5} G_0$ and the full DNA/PNA heteroduplex has a value of $7.4 \times 10^{-5} G_0$. The conductance of the 20-bp DNA/PNA duplex is roughly five times smaller than that found for 10-bp DNA/PNA heteroduplexes.¹⁷ Both nicked duplexes have most probable conductance values that are slightly larger than those for the full versions of each duplex. The nicked 20-bp DNA homoduplex has a most probable conductance value of $8.4 \times 10^{-5} G_0$; and the nicked DNA/PNA heteroduplex has a most probable value of $7.9 \times 10^{-5} G_0$. These increases, albeit small, over the full 20-bp duplexes (see Table 4.2) can be rationalized by a larger backbone flexibility of the nicked duplexes,¹⁷ which may allow for improved couplings between π -orbitals in the base stack. This supposition is supported by the observation that the histograms for the nicked duplexes have a broader distribution, reflected by the larger standard deviations of the Gaussian functions used to fit the histograms, than the corresponding full duplexes. The standard deviations for both nicked duplexes are approximately twice those for the full DNA and DNA/PNA duplexes (Table 4.2). The increase in the flexibility can also be quantitatively evaluated through a statistical analysis of the individual trajectories (*vide infra*). The fact that the conductance of the 20-bp DNA/PNA full or nicked heteroduplex is slightly larger than that of the 20-bp DNA full or nicked duplex with the same sequence is similar to the relationship observed between the conductance of 10-bp DNA homoduplexes and DNA/PNA heteroduplexes.¹⁷ This modest enhancement of the conductance was attributed to a greater flexibility for the DNA/PNA heteroduplex compared to the DNA homoduplex.

In the spirit of recent correlation analyses,³³⁻³⁶ a conductance correlation treatment was employed to evaluate the differences in the conductance of full and nicked duplexes for various periods. Figure 4.5 shows the two-dimensional correlation plots for the full DNA, full DNA/PNA, and their nicked versions. Within each trajectory, the fitted conductance value for a given period,

n, was correlated to the fitted conductance value for another period, k. The correlation parameters between periods were averaged over the set of collected trajectories for each duplex. Similarity between conductance values results in a high degree of correlation and a greater correlation parameter, while variations between the conductance values of periods n and k result in a lower correlation parameter. Thus, fluctuations of the conductance within a trajectory lead to a loss in correlation. For example, Figure 4.5A shows a high degree of correlation between periods 2 and 3, suggesting these periods will have a high degree of similarity in the fitted conductance value, on average. However, periods 2 and 10 have very little correlation, indicating that the fitted conductance values are significantly different between these periods, on average. The two-dimensional correlation plots are symmetric about the diagonal because the correlation between periods n and k is equivalent to the correlation between periods k and n. The correlation equals one along the diagonal, when $n = k$.

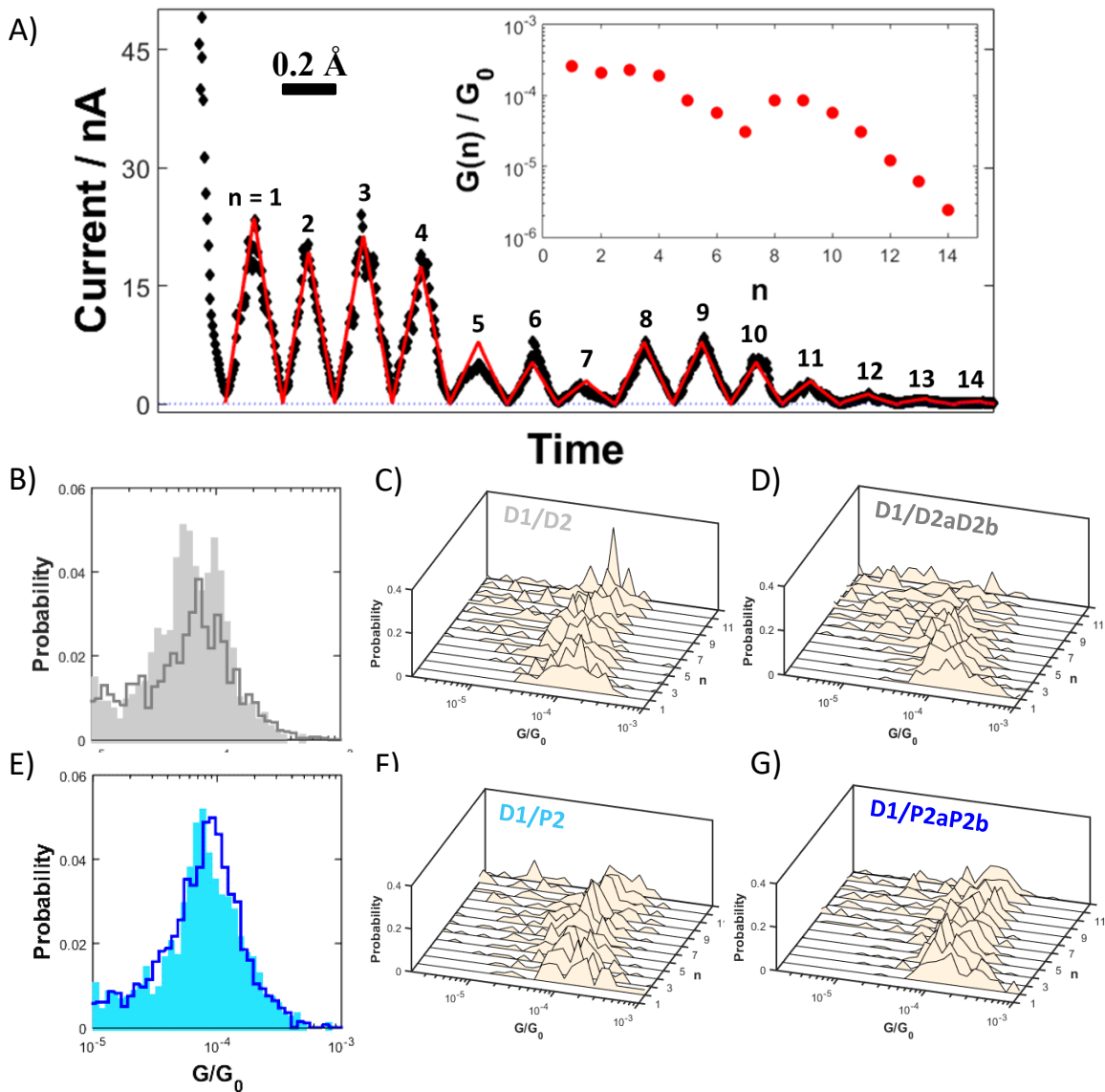


Figure 4.4. (A) An example current-time $I(t)$ trajectory of a full DNA molecular junction is shown (black) with the fitted current response overlaid (red). The STM tip retracts 0.2 \AA during each current response period. The inset shows the fitted conductance, $G(n)$, for each period in the current response. Conductance histograms are shown for the full DNA duplex (shaded cells) with the nicked analogue (unfilled cells) overlaid (B) and the full DNA/PNA duplex (shaded cells) with the nicked analogue (unfilled cells) overlaid (E). Three dimensional plots of conductance histograms for specific periods of the current responses are shown for all four duplexes (C), (D), (F), and (G).

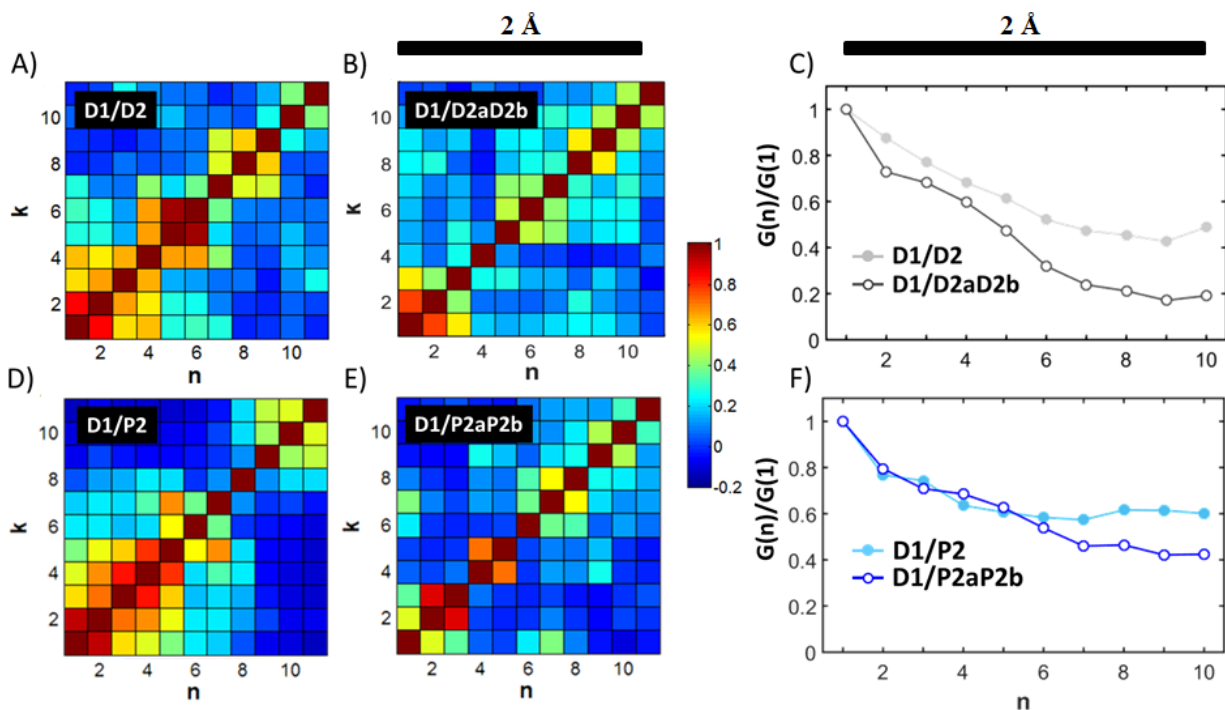


Figure 4.5. Two-dimensional correlation plots for the full DNA (A), full DNA/PNA (D), and nicked duplexes (B) and (E). Each square represents the correlation between the conductance values for given periods n and k . By nature, the correlation has a value of one along the diagonal, when $n = k$. Panels C and F show the average ratio of the fitted conductance for period n to the fitted conductance for period 1. The total displacement over ten current response periods is 2 Å.

Figures 4.5A and 4.5B show the two-dimensional correlation plots for the full and nicked DNA duplexes. Figures 4.5D and 4.5E show the plots for the full and nicked heteroduplexes. In both cases, the plots show noticeably less correlation for the nicked duplexes, indicating that the fitted conductance values vary more for the nicked duplexes. This lessened correlation is represented by the lower correlation parameters adjacent to the diagonal for the nicked duplexes, suggesting that the fitted conductance values are more variable between proximal current response periods. This analysis supports the supposition that the nicked duplexes are more flexible than their full counterparts.

The ratio of the conductance value for each period in the current response to the conductance value of the first period was calculated and averaged over the entire set of trajectories.

The results of this analysis are shown in Figure 4.5C and 4.5F. The ratios show that the correlation for the full duplexes (D1/D2 and D1/P2) extend to longer periods; i.e., the full version of the nucleic acid duplex has a higher conductance value at later periods relative to the first current response period. As the molecular junctions transition to lower conductance modes in later periods of the trajectory,³⁷⁻³⁸ the correlation in the conductance decreases to a greater extent for the nicked duplexes than for the full duplexes. Thus, the nicked duplexes form less stable molecular junctions than the full duplexes.

4.2.3 Effect of PNA Content on Conductance

Figure 4.6 compares conductance histograms for the 20-bp DNA/PNA heteroduplex, a 20-bp PNA homoduplex (P1/P2), and a nicked PNA/PNA:DNA heteroduplex (P1/P2a/D2b). The latter two duplexes are different from the ones shown in Figure 4.4. The PNA homoduplex has 20 PNA/PNA base pairs. The nicked PNA/PNA:DNA duplex has ten PNA/PNA base pair hybridization and ten DNA/PNA base pairs. In each case, the histograms are fit by Gaussian functions to best identify the most probable conductance. For the PNA/PNA:DNA heteroduplex shown in Figure 4.6, the thiol linkers are present on the PNA strands. However, the conductance of a duplex linked through a thiol on the 10-base DNA strand was measured; and the observed conductance histogram is similar to that observed for the duplexes with the thiol on the 10-base PNA strand (see Supporting Information). Note that the fits for the PNA homoduplex and the nicked heteroduplex include multiple conductance modes, referred to as high and medium modes. Such modes have been attributed to different binding motifs for the thiol on the Au surface.³⁸ The most probable value for the high conductance mode of the duplexes are reported in Table 4.2. The PNA homoduplex displays a most probable conductance value that is approximately ten times larger than the DNA homoduplex and the nicked DNA/PNA heteroduplex but only three times

larger than the most probable conductance for the nicked PNA/PNA:DNA heteroduplex. These increases are consistent with previous findings for 10-bp DNA and PNA homoduplexes and DNA/PNA heteroduplexes.^{17, 25, 39} Note that the ratio between the values of the high-conductance mode and medium-conductance mode for the data shown in Figure 4.6 is similar to the previously reported ratio for thiol-terminated molecules, suggesting that the interaction between the duplex and electrode is exclusively through the thiol-Au linkage rather than also through the duplex itself.³⁷⁻³⁸ The values of the molecular conductance of the duplexes shown in Table 4.2 show that the molecular conductance increases as the number of PNA nucleobase pairs in the duplex increases. This relationship could allow the conductance of a duplex of a given length to be tuned by its PNA content.

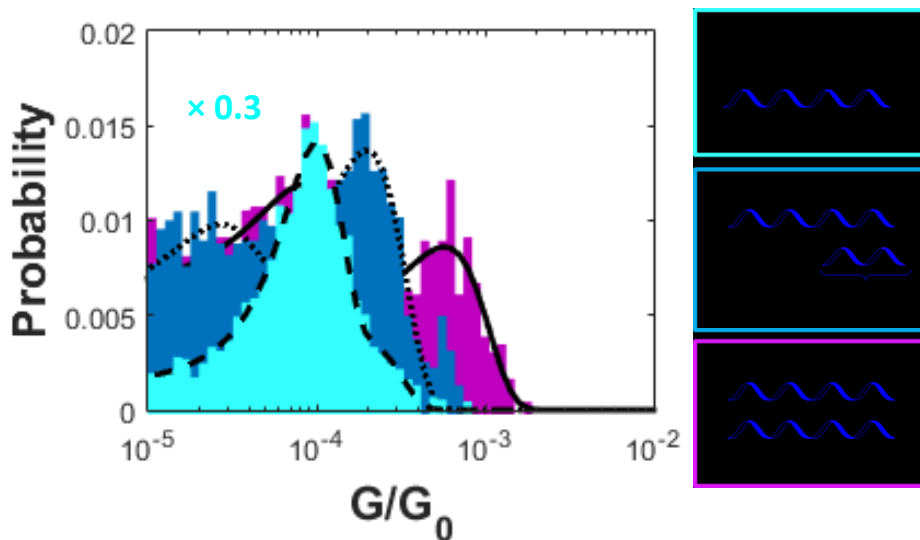


Figure 4.6. The conductance histograms for the full DNA/PNA heteroduplex (turquoise), the full PNA homoduplex (magenta), and the nicked PNA/PNA:DNA heteroduplex (blue). The black curves in each case are fits by a sum of two Gaussian functions. For the purposes of comparison, the height of the histogram for the full DNA/PNA heteroduplex is scaled by a factor of 0.3.

The fact that the conductance of the 20-bp PNA duplex is one order of magnitude greater than that of the DNA 20-bp duplex is consistent with the previous finding of a 12-fold increase in the conductance of a PNA 10-bp duplex over that of a DNA duplex of the same sequence.¹⁷ The

nicked versions of the DNA and DNA/PNA show slightly larger conductance than the full duplexes; however, the distribution of the conductance values for the nicked duplexes is broader than that of full duplexes. The nicked PNA/PNA:DNA heteroduplex shows a greater conductance than both the nicked and full DNA/PNA heteroduplex. Multiple correlation analyses of the trajectories for the full DNA and DNA/PNA duplexes versus their nicked analogues show that the current responses vary more and the number of periods in a trajectory is smaller, on average, for the nicked duplexes, suggesting that the conductance through the nicked systems is less stable.

Table 4.2. Summary of the single molecule conductance, G , and its standard deviation, σ_G , for the nucleic acid duplexes.

Duplex	G ($\times 10^{-5} G_0$)	σ_G ($\times 10^{-5} G_0$)
DNA	5.5	1.9
Nicked DNA	8.4	3.6
DNA/PNA	7.4	1.4
Nicked DNA/PNA	7.9	4.1
Nicked PNA/PNA:DNA	20	12
PNA/PNA	57	41

4.3 DISCUSSION

An investigation of the effect of a backbone nick on the single-molecule conductance of DNA and PNA duplexes indicates that the conductance values of the nicked duplexes are similar to that of full duplexes despite the fact that both the thermal stability of the nicked duplexes and the stability for the molecular junctions are lower. Conductance ratios for trajectory periods

relative to the first period show that the nicked duplexes experience a drop in the conductance at earlier periods of the trajectory, implying a lower integrity (Figure 4.5). Further, the standard deviations of the fitted gaussian functions of the conductance histograms for the nicked DNA homoduplex and DNA/PNA heteroduplex are greater than the standard deviations for their full analogues (see Table 4.2). These observations indicate that the presence of a nick in the backbone of the molecular bridge reduces the stability of the molecular junction and increases the variability of its single-molecule conductance.

The influence of the PNA content on the conductance of the duplex was examined. The single-molecule conductance varies over a range of almost an order of magnitude depending on the relative amount of DNA and PNA strands comprising a duplex of given length and with a specific linker. The conductance decreased from the duplex with the greatest PNA content to that of the nicked PNA/PNA:DNA heteroduplex to that of the duplex with lowest PNA content.

The measured conductance of the 20-bp duplexes is approximately five times smaller than that reported for shorter, 10-bp DNA duplexes with similar mixed nucleobase sequence.¹⁷ This decrease in conductance with the length of the duplex is consistent with that expected by extrapolating the dependence on bridge length of the DNA molecular conductance determined in earlier studies.^{25, 39} Figure 4.7 shows a plot of the logarithm of recently reported highest conductance values measured for 6 to 26 base pair DNA duplexes versus the number of A/T base pairs in the duplexes.^{17, 39-44} This analysis assumes that the G/C base pairs do not contribute to the ‘effective’ tunneling length and that the number of A/T pairs dictates the conductance. This assumption is based on the conclusion of recent studies indicating that G/C pairs are much less resistive than A/T pairs.^{43,45} The data are reasonably fit by an exponential decay function $G/G_0 = 9.0 \times 10^{-4} \exp(-0.50 \cdot l)$ where l is the number of A/T base pairs. The preexponential term

indicates the conductance of a strand with an effective length of zero base pairs, which corresponds to two linker lengths or one hexanedithiol. This value lies between the high conductance mode value of $1.3 \times 10^{-3} G_0$ and the medium conductance mode value of $3.4 \times 10^{-4} G_0$ reported for hexanedithiol.⁴⁶ The shaded region in the plot of Figure 4.7 shows a 95% confidence interval for the best fit. Omission of the apparent outlier with four A/T base pairs results in an exponential fit with a similar decay constant and preexponential term, still falling within the aforementioned conductance values for hexanedithiol. Using a pitch of 0.33 Å per base pair, one calculates a characteristic decay length parameter of 1.5 per Å for the A/T base pairs. A plot of these conductance data versus the total number of base pairs shows that the exponential dependence is lost when G/C base pairs are included in the length count; see Supporting Information.

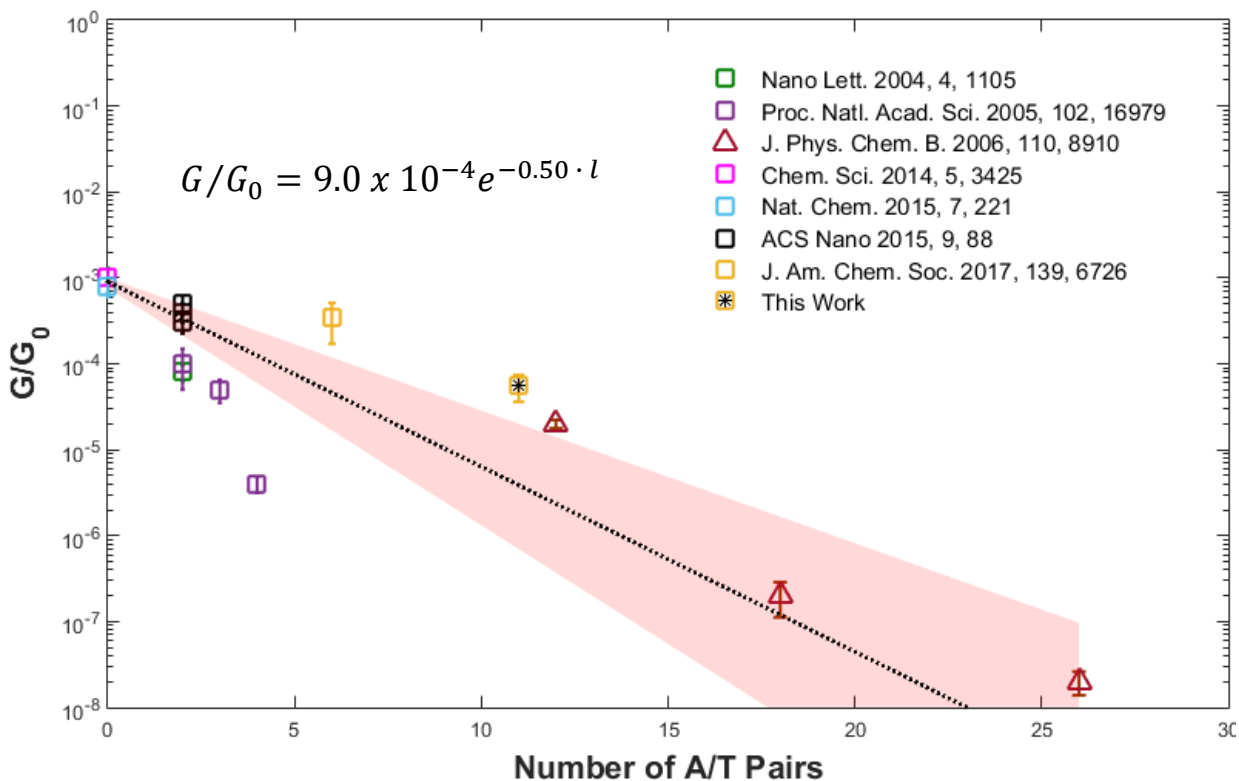


Figure 4.7. Conductance values for DNA duplexes as a function of the A/T content of the duplex measured by various methods. In the conductance measurements, the DNA was attached to the surface by three-carbon (C3) thiol linkers. Squares identify the conductance measured by the scanning tunneling microscope break junction method. Triangles identify values measured by atomic force microscopy conductance utilizing a gold nanoparticle. The dashed line indicates the best fit function; and the shaded region shows a 95% confidence interval for the best fit.

4.4 CONCLUSION

A comparison of full and nicked versions of DNA homoduplexes and DNA/PNA heteroduplexes has shown that the presence of a ‘nick’ in the backbone of the duplex results in a lowered thermal stability and a greater variability in the molecular conductance compared to duplexes without the ‘nick’ in the backbone. The melting temperature of the nicked nucleic acid duplex is considerably lower than its full analogue in both cases. While the nicked duplexes exhibit an average molecular conductance that matches that for the full version in each case, the conductance values of the nicked duplexes show increased variability over the lifetime of the molecular junction, suggesting the ‘nick’ affects the integrity of the duplex. One can therefore expect the conductance of supramolecular assemblies comprising smaller, nicked components to maintain the conductance of structures composed of larger strands, but suffer from increased variability in molecular conductance.

4.5 METHODS

4.5.1 PNA Synthesis

All reagents were purchased from commercial suppliers and used as received. Boc/Z and Fmoc/Bhoc PNA monomers were purchased from PolyOrg Inc. and ASM Research Chemicals and used without further purification. The synthesis of the pyrene PNA monomer ester by a modified published procedure is outlined in the SI. Characterization of the oligomers was performed by MALDI-TOF mass spectrometry on an Applied Biosystems Voyager Biospectrometry Workstation with Delayed Extraction. All reactions were performed under

ambient atmosphere unless otherwise noted. Anaerobic reactions were performed in Schlenk tubes under N₂ atmosphere.

Melting temperature experiments were performed in 10-mm path length quartz cells on a Varian Cary 300 spectrophotometer equipped with a programmable temperature block. PNA stock solutions were prepared in deionized water and were stored at -25 °C. The PNA solutions for UV and CD experiments were performed in 10 mM, pH 7.0 phosphate buffer. PNA concentrations were determined by UV-Vis spectrophotometry assuming $\epsilon(260) = 8600, 6600, 13700,$ and $11700 \text{ cm}^{-1} \text{ M}^{-1}$ for each T, C, A, and G monomer, respectively.⁴⁷ The extinction coefficients for pyrene at 90 °C were measured: $\epsilon(260) = 12711$ and $\epsilon(345) = 28319 \text{ cm}^{-1} \text{ M}^{-1}$. All CD data were recorded at room temperature; and the spectra represent an average of 10 scans, recorded from 350 to 220 nm at the rate of 50 nm/min. A 1-cm path length cuvette was used. Excitation and emission spectra were obtained using a Cary Eclipse fluorimeter. Emission spectra were recorded with 0.2 ms delay time and 5 ms gate time in the range 360-600 nm with selective irradiation at 345 nm ($\lambda_{\text{ex}} = 345 \text{ nm}$).

More details about the synthesis of the Pyrene PNA monomer and of the PNA oligomers as well as their characterization are included in the SI.

4.5.2 Conductance Measurements

4.5.2.1 Substrate Fabrication

Template-stripped⁴⁸ Au substrates were created by evaporating 100 nm gold films onto freshly cleaved mica (AJA ATC-T Series Thermal Evaporation System). The gold films were transferred to Piranha-cleaned glass slips (10 mm × 25 mm) prior to each experiment. 50 μL of 20 μM duplex solutions were deposited and the terminal thiols were allowed to bind to the gold

substrates for less than 20 s. The substrates were washed with DI water, washed with ethanol (200 proof), and dried under a stream of argon.

4.5.2.2 Data Collection

All conductance measurements were performed using an Agilent 5500 scanning probe microscope system. An environmental chamber was housed in a homemade acoustically isolated Faraday cage seated on an anti-vibrational system (Table Stable). The gold STM tips (0.25 mm, 99.95% gold wire, Alfa Aesar) were freshly cut prior to each experiment. All experiments were performed under an argon atmosphere, and the gold substrates were immersed in mesitylene. A triangular, 0.3 ± 0.3 V bias with a modulation frequency of 500 Hz was applied across the substrate/STM tip gap (Stanford Research Systems, DS345 Function Generator). All measurements were performed using a 10 nA/V preamplifier.

4.5.2.3 Data Analysis

Data filtering and analysis were performed using a custom Matlab code. The current-time trajectories were filtered to remove trajectories that did not display molecular junctions (i.e. ‘empty’ trajectories). Each trajectory is partitioned into periods through a fit to the modulated applied bias. The employed correlation treatment was adopted from previous studies,²⁶⁻²⁹ but modified to correlate the fitted conductance value from each conductance period.

4.6 REFERENCES

1. Aviram, A.; Ratner, M. A., Molecular Rectifiers. *Chem. Phys. Lett.* **1974**, *29*, 277-283.
2. Perrin, M. L.; Galan, E.; Eelkema, R.; Thijssen, J. M.; Grozema, F.; van der Zant, H. S. J., A Gate-Tunable Single-Molecule Diode. *Nanoscale* **2016**, *8*, 8919-8923.
3. Chen, Y.-S.; Hong, M.-Y.; Huang, G. S., A Protein Transistor Made of an Antibody Molecule and Two Gold Nanoparticles. *Nat. Nanotechnol.* **2012**, *7*, 197-203.
4. McCreery, R. L.; Yan, H.; Bergren, A. J., A Critical Perspective on Molecular Electronic Junctions: There Is Plenty of Room in the Middle. *Phys. Chem. Chem. Phys.* **2013**, *15*, 1065-1081.

5. Amdursky, N.; Marchak, D.; Sepunaru, L.; Pecht, I.; Sheves, M.; Cahen, D., Electronic Transport Via Proteins. *Adv. Mater.* **2014**, *26*, 7142-7161.
6. Guldi, D. M.; Nishihara, H.; Venkataraman, L., Special Issue: Molecular Wires. *Chem. Soc. Rev.* **2015**, *44*, 842-1027.
7. Alessandrini, A.; Facci, P., Electron Transfer in Nanobiodevices. *Eur. Polym. J.* **2016**, *83*, 450-466.
8. Facci, P., *Biomolecular Electronics: Bioelectronics and the Electrical Control of Biological Systems and Reactions*; Elsevier: Waltham, MA, 2014.
9. *Molecular Electronics: An Experimental and Theoretical Approach*; Baldea, I., Ed.; Pan Stanford: Singapore, 2016.
10. Pearson, A. C.; Liu, J.; Pound, E.; Uprety, B.; Woolley, A. T.; Davis, R. C.; Harb, J. N., DNA Origami Metallized Site Specifically to Form Electrically Conductive Nanowires. *J. Phys. Chem. B* **2012**, *116*, 10551-10560.
11. Hong, F.; Zhang, F.; Liu, Y.; Yan, H., DNA Origami: Scaffolds for Creating Higher Order Structures. *Chem. Rev.* **2017**, *117*, 12584-12640.
12. Lu, Q.; Liu, K.; Zhang, H.; Du, Z.; Wang, X.; Wang, F., From Tunneling to Hopping: A Comprehensive Investigation of Charge Transport Mechanism in Molecular Junctions Based on Oligo(P-Phenylene Ethynylene)S. *ACS Nano* **2009**, *3*, 3861-3868.
13. Venkatramani, R.; Keinan, S.; Balaeff, A.; Beratan, D. N., Nucleic Acid Charge Transfer: Black, White and Gray. *Coord. Chem. Rev.* **2011**, *255*, 635-648.
14. Wierzbinski, E., et al., Effect of Backbone Flexibility on Charge Transfer Rates in Peptide Nucleic Acid Duplexes. *J. Am. Chem. Soc.* **2012**, *134*, 9335-9342.
15. Zhang, Y.; Liu, C.; Balaeff, A.; Skourtis, S. S.; Beratan, D. N., Biological Charge Transfer Via Flickering Resonance. *Proc. Natl. Acad. Sci. U.S.A.* **2014**, *111*, 10049-10054.
16. Li, G.; Govind, N.; Ratner, M. A.; Cramer, C. J.; Gagliardi, L., Influence of Coherent Tunneling and Incoherent Hopping on the Charge Transfer Mechanism in Linear Donor-Bridge-Acceptor Systems. *J. Phys. Chem. Lett.* **2015**, *6*, 4889-4897.
17. Beall, E.; Ulku, S.; Liu, C.; Wierzbinski, E.; Zhang, Y.; Bae, Y.; Zhang, P.; Achim, C.; Beratan, D. N.; Waldeck, D. H., Effects of the Backbone and Chemical Linker on the Molecular Conductance of Nucleic Acid Duplexes. *J. Am. Chem. Soc.* **2017**, *139*, 6726-6735.
18. Strano, M. S., Functional DNA Origami Devices. *Science* **2012**, *338*, 890-891.
19. Pinheiro, A. V.; Han, D.; Shih, W. M.; Yan, H., Challenges and Opportunities for Structural DNA Nanotechnology. *Nat. Nanotechnol.* **2011**, *6*, 763-772.
20. Seeman, N. C., *Structural DNA Nanotechnology*; Cambridge University Press: Cambridge, U.K., 2016.
21. Lewis, F. D.; Wu, Y.; Zhang, L.; Zuo, X.; Hayes, R. T.; Wasielewski, M. R., DNA-Mediated Exciton Coupling and Electron Transfer between Donor and Acceptor Stilbenes Separated by a Variable Number of Base Pairs. *J. Am. Chem. Soc.* **2004**, *126*, 8206-8215.
22. Liu, T.; Barton, J. K., DNA Electrochemistry through the Base Pairs Not the Sugar-Phosphate Backbone. *J. Am. Chem. Soc.* **2005**, *127*, 10160-10161.
23. Traub, M. C.; Brunschwig, B. S.; Lewis, N. S., Relationships between Nonadiabatic Bridged Intramolecular, Electrochemical, and Electrical Electron-Transfer Processes. *J. Phys. Chem. B* **2007**, *111*, 6676-6683.

24. Zhou, X.-S.; Liu, L.; Fortgang, P.; Lefevre, A.-S.; Serra-Muns, A.; Raouafi, N.; Amatore, C.; Mao, B.-W.; Maisonhaute, E.; Schöllhorn, B., Do Molecular Conductances Correlate with Electrochemical Rate Constants? Experimental Insights. *J. Am. Chem. Soc.* **2011**, *133*, 7509-7516.
25. Wierzbinski, E.; Venkatramani, R.; Davis, K. L.; Bezer, S.; Kong, J.; Xing, Y.; Borguet, E.; Achim, C.; Beratan, D. N.; Waldeck, D. H., The Single-Molecule Conductance and Electrochemical Electron-Transfer Rate Are Related by a Power Law. *ACS Nano* **2013**, *7*, 5391-5401.
26. Nitzan, A., The Relationship between Electron Transfer Rate and Molecular Conduction 2. The Sequential Hopping Case. *Isr. J. Chem.* **2002**, *42*, 163-166.
27. Egholm, M.; Buchardt, O.; Nielsen, P. E.; Berg, R. H., Peptide Nucleic Acids (PNA). Oligonucleotide Analogs with an Achiral Peptide Backbone. *J. Am. Chem. Soc.* **1992**, *114*, 1895-1897.
28. Ratilainen, T.; Holmén, A.; Tuite, E.; Haaima, G.; Christensen, L.; Nielsen, P. E.; Nordén, B., Hybridization of Peptide Nucleic Acid. *Biochemistry* **1998**, *37*, 12331-12342.
29. Birks, J. B., *Photophysics of Aromatic Molecules*; Wiley: London, 1970.
30. Beall, E.; Yin, X.; Waldeck, D. H.; Wierzbinski, E., A Scanning Tunneling Microscope Break Junction Method with Continuous Bias Modulation. *Nanoscale* **2015**, *7*, 14965-14973.
31. Xu, B.; Tao, N. J., Measurement of Single-Molecule Resistance by Repeated Formation of Molecular Junctions. *Science* **2003**, *301*, 1221-1223.
32. van Wees, B. J.; van Houten, H.; Beenakker, C. W.; Williamson, J. G.; Kouwenhoven, L. P.; van der Marel, D.; Foxon, C. T., Quantized Conductance of Point Contacts in a Two-Dimensional Electron Gas. *Phys. Rev. Lett.* **1988**, *60*, 848-850.
33. Halbritter, A.; Makk, P.; Mackowiak, S.; Csonka, S.; Wawrzyniak, M.; Martinek, J., Regular Atomic Narrowing of Ni, Fe, and V Nanowires Resolved by Two-Dimensional Correlation Analysis. *Phys. Rev. Lett.* **2010**, *105*, 266805.
34. Makk, P.; Tomaszewski, D.; Martinek, J.; Balogh, Z.; Csonka, S.; Wawrzyniak, M.; Frei, M.; Venkataraman, L.; Halbritter, A., Correlation Analysis of Atomic and Single-Molecule Junction Conductance. *ACS Nano* **2012**, *6*, 3411-3423.
35. Aradhya, S. V.; Frei, M.; Halbritter, A.; Venkataraman, L., Correlating Structure, Conductance, and Mechanics of Silver Atomic-Scale Contacts. *ACS Nano* **2013**, *7*, 3706-3712.
36. Wang, K.; Hamill, J. M.; Zhou, J.; Xu, B., Mapping the Details of Contact Effect of Modulated Au-Octanedithiol-Au Break Junction by Force-Conductance Cross-Correlation. *J. Am. Chem. Soc.* **2014**, *136*, 17406-17409.
37. Haiss, W.; Martín, S.; Leary, E.; Zalinge, H. v.; Higgins, S. J.; Bouffier, L.; Nichols, R. J., Impact of Junction Formation Method and Surface Roughness on Single Molecule Conductance. *J. Phys. Chem. C* **2009**, *113*, 5823-5833.
38. Li, C.; Pobelov, I.; Wandlowski, T.; Bagrets, A.; Arnold, A.; Evers, F., Charge Transport in Single Au | Alkanedithiol | Au Junctions: Coordination Geometries and Conformational Degrees of Freedom. *J. Am. Chem. Soc.* **2008**, *130*, 318-326.
39. Xu, B. Q.; Zhang, P. M.; Li, X. L.; Tao, N. J., Direct Conductance Measurement of Single DNA Molecules in Aqueous Solution. *Nano Lett.* **2004**, *4*, 1105-1108.

40. Hihath, J.; Xu, B.; Zhang, P.; Tao, N., Study of Single-Nucleotide Polymorphisms by Means of Electrical Conductance Measurements. *Proc. Natl. Acad. Sci. U.S.A.* **2005**, *102*, 16979-16983.
41. Nogues, C.; Cohen, S. R.; Daube, S.; Apter, N.; Naaman, R., Sequence Dependence of Charge Transport Properties of DNA. *J. Phys. Chem. B* **2006**, *110*, 8910-8913.
42. Wang, K.; Hamill, J. M.; Wang, B.; Guo, C. L.; Jiang, S. B.; Huang, Z.; Xu, B. Q., Structure Determined Charge Transport in Single DNA Molecule Break Junctions. *Chem. Sci.* **2014**, *5*, 3425-3431.
43. Xiang, L.; Palma, J. L.; Bruot, C.; Mujica, V.; Ratner, M. A.; Tao, N., Intermediate Tunnelling–Hopping Regime in DNA Charge Transport. *Nat. Chem.* **2015**, *7*, 221-226.
44. Bruot, C.; Xiang, L.; Palma, J. L.; Tao, N., Effect of Mechanical Stretching on DNA Conductance. *ACS Nano* **2015**, *9*, 88-94.
45. Di Felice, R.; Calzolari, A.; Molinari, E.; Garbesi, A., Ab Initio Study of Model Guanine Assemblies: The Role of Π – Π Coupling and Band Transport. *Phys. Rev. B* **2001**, *65*, 045104.
46. Nishikawa, A.; Tobita, J.; Kato, Y.; Fujii, S.; Suzuki, M.; Fujihira, M., Accurate Determination of Multiple Sets of Single Molecular Conductance of Au/1,6-Hexanedithiol/Au Break Junctions by Ultra-High Vacuum-Scanning Tunneling Microscope and Analyses of Individual Current–Separation Curves. *Nanotechnology* **2007**, *18*, 424005.
47. *Peptide Nucleic Acids: Protocols and Applications*; Nielsen, P. E., Ed.; Horizon Bioscience: Wymondham, U.K., 2004.
48. Hegner, M.; Wagner, P.; Semenza, G., Ultralarge Atomically Flat Template-Stripped Au Surfaces for Scanning Probe Microscopy. *Surf. Sci.* **1993**, *291*, 39-46.

5.0 EFFECT OF FLEXIBILITY ON THE INTERPLAY OF COHERENCE AND INCOHERENCE IN NUCLEIC ACID CONDUCTANCE

5.1 INTRODUCTION

Investigations into the molecular conductance of nucleic acids are beginning to uncover new features of the fundamental mechanism that governs charge transfer on the nanoscale.¹⁻² The interplay between coherent tunneling and incoherent charge hopping has been the subject of numerous experimental³⁻⁷ and theoretical⁸⁻¹⁰ studies on nucleic acid duplexes, with short charge-transfer distances following coherent models and longer distances following a hopping mechanism. Charge hopping, slowed by the occupation of hopping sites,¹¹ is dominated by the more efficient tunneling mechanism for shorter barrier widths ($< 30 \text{ \AA}$).¹² However, the exponential distance dependence of tunneling results in a hopping behavior being dominant at longer distances ($> 30 \text{ \AA}$), for which the distance dependence is a much shallower inverse proportionality. The dichotomous relationship between these mechanisms includes the coexistence of coherence and incoherence for intermediate distances where neither mechanism is dominant.¹³⁻¹⁴ It is here that the effects of base couplings and charge delocalization can be amplified and conductance values can vary greatly for duplexes of the same length.

The single molecule conductance values of DNA duplexes with alternating cytosine (C) and guanine (G) bases were recently compared to those for duplexes of the same length with the G bases separated into blocks.¹⁴ The single molecule conductance measured for duplexes with alternating bases displayed a simple linear decrease, while that for the duplexes with the G blocks exhibited an oscillatory behavior. Oscillatory behavior has been observed in other systems, ranging from metal atom to carbon chains.¹⁵⁻¹⁸ The linear trend for the alternating sequences was

interpreted in terms of incoherent transport; however, the deviations from the charge hopping model for the G block duplexes suggest that a coherent contribution may also be present.¹⁹ It was concluded that charge delocalization over the highly-coupled, adjacent G bases allowed for partial coherence in the charge transport.

Further investigations of these DNA systems have sought to determine the effect of charge directionality in the duplexes.²⁰ For G block duplexes, it was shown that positioning the molecular linkers on the 3' termini causes an order of magnitude increase in the single molecule conductance relative to duplexes with molecular linkers on the 5' termini. The enhancement for 3' systems is rationalized by a geometrically-improved coupling between opposite strand G bases at the center of the duplex. As charge moves through the base stack via G mediation,²¹ there is a cross-strand step whose rate is strongly dependent on the alignment and coupling of the G bases.²² The much larger coupling for the 3' duplexes not only enhances the conductance, but also dampens the oscillatory effect associated with the coherent contribution to the charge transfer. For these systems, the cross-strand step dominates the coherent mechanism or delocalization effects.

The importance of flexibility as a modulator for conformation and local electronics has also been explored for nucleic acid duplexes.²³⁻²⁶ For duplexes with greater flexibility, average single molecule conductance values are greater than less flexible duplexes of the same length.²⁶ This can be rationalized by an increase in the accessible conformational space and a broadening of the local energies along the base stack. Therefore, the role of the backbone in the interplay of coherence and incoherence in nucleic acid systems will hinge on the degree to which the conformational freedom and energetic broadening is modulated. It is not yet clear how the emergence of a dominant mechanism will be affected by molecular flexibility and the extent of bath coupling.

In this paper, the effect of backbone flexibility on the relationship between coherent and incoherent charge transfer mechanisms is investigated. The hypothesis that a more flexible nucleic acid duplex will reduce the directional dependence observed in DNA systems is tested for duplexes composed of peptide nucleic acid (PNA) oligomers.²⁷ The single molecule conductance of PNA is measured for duplexes of varying lengths and with the molecular linkers positioned at the opposing termini. Conductance comparisons between duplexes with molecular linkers on the N and C termini indicate that the cross-strand coupling effects in the more rigid DNA systems are effectively washed out by the more flexible backbone's ability to occupy advantageous geometries that maximize electronic couplings between G bases.

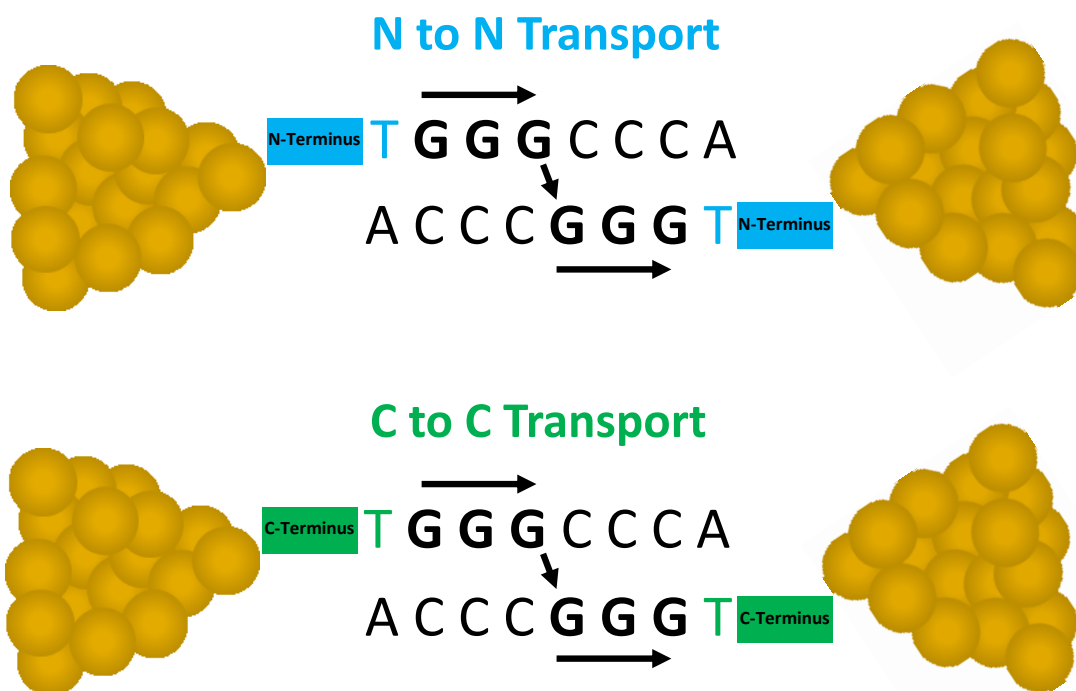


Figure 5.1. The opposing termini orientations are shown for N to N transport and C to C transport for $n = 3$. In both cases, the duplexes are anchored to the gold electrodes via amine modifications on the terminal thymine nucleobase. The arrows indicate the path of charge transport through the duplex via a hopping mechanism, including a cross-strand step at the center of the duplex.

Figure 1 shows the two opposing termini orientations for the N linker PNA and C linker PNA. For the N linker PNA, the amine-modified thymine nucleobase is positioned at the N-terminus of the PNA oligomer. When the self-complementary oligomers hybridize, amine modifications are positioned at opposite ends of the PNA duplex at each N-terminus. Therefore, as charge moves through the duplex, the direction of the transport is from the N-terminus of one oligomer to the N-terminus of the complementary oligomer in the duplex, resulting in N to N transport. For the C linker PNA, the amine modification is on the C-terminus, so the resulting charge transport is C to C. Based on the positions and spacings of the nucleobases, the N terminus is analogous to the 5' terminus of DNA and the C terminus is analogous to the 3' terminus of DNA.²⁸ The geometry of the duplex results in unique transport characteristics for these two transport cases.

5.2 RESULTS

Single molecule conductance measurements were performed on PNA duplexes of varying lengths and with opposing termini orientations. A diffuse monolayer of duplexes with amine linkers on the terminal thymine nucleobases was formed on a gold substrate. Following a modified version of the scanning tunneling microscope break junction (STM-BJ) procedure,²⁹⁻³⁰ an STM tip was driven to the surface of the gold substrate and then withdrawn, allowing molecular junctions to form between the substrate and the tip. Under a continuously modulated bias, current-time trajectories were collected for the molecular junctions and then compiled to create conductance histograms. The conductance in each histogram is scaled relative to the conductance quantum, $G_0 = 2e^2/h = 77.5 \mu\text{S}$.³¹

Figure 2 shows the conductance histograms for the N linker PNA duplexes with the sequence $\text{TG}_n\text{C}_n\text{A}$, for $n = 3-7$. For the histograms that present with multiple peaks, the peaks

associated with both modes are fit to a sum of two Gaussian functions to determine the most probable conductance value for each peak. These peaks can be attributed to multiple conductance modes.³²⁻³³ For the purposes of comparison, only the highest observable mode is considered. In some instances, there is an appearance of a shoulder or second peak at twice the conductance value of the most probable peak. This is attributed to two or more molecules forming molecular junctions simultaneously.

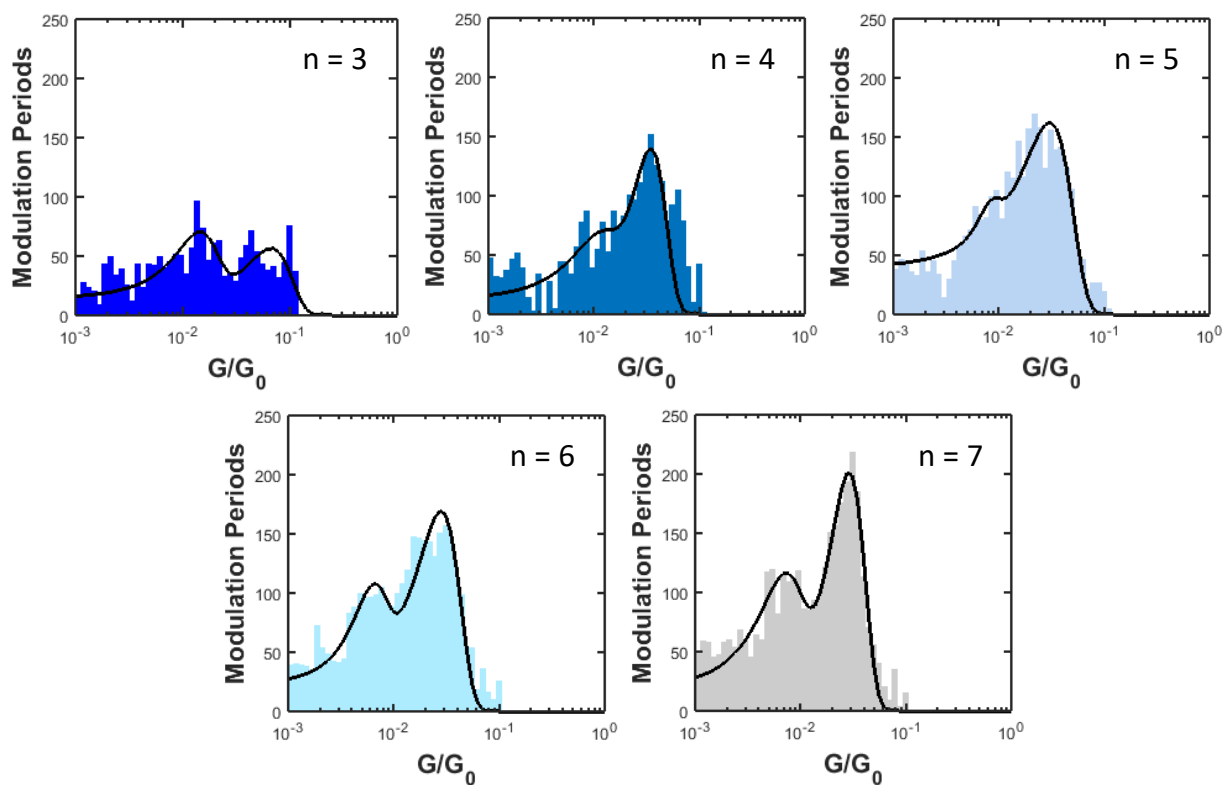


Figure 5.2. Conductance histograms are shown for the N linker PNA for $n = 3-7$. The black curve overlaid is a fit to two Gaussian functions. The histograms shown are total counts after subtraction of the background counts collected over the same number of experiments for each duplex (see Appendix D).

The average single molecule conductance values for the highest observable mode for each duplex is shown in the plot in Figure 3. For the N linker PNA, the average conductance value is roughly $3 \times 10^{-2} G/G_0$. The weak distance dependence observed for the strands agrees with an

effective length treatment that ignores GC pairs.³⁴ The magnitudes of the average conductance values for the PNA duplexes is roughly an order of magnitude greater than the DNA duplexes of the same length. This is consistent with what has been observed in duplexes of a mixed sequences and similar lengths.^{26, 34}

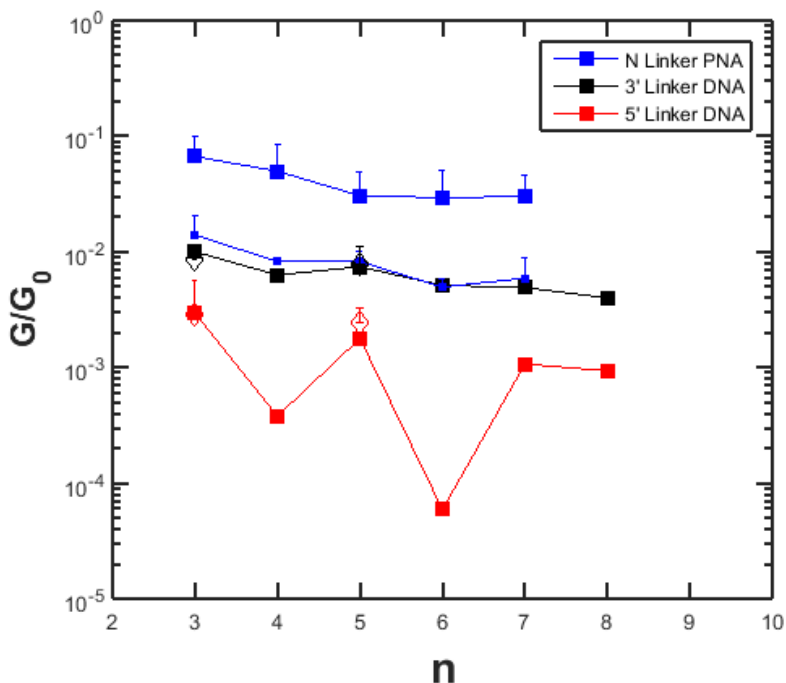


Figure 5.3. The results for the N linker PNA are presented with data for 3' linker DNA and 5' linker DNA from a previous study.²⁰ The open symbols are measurements performed to confirm the results taken from ref. 20. The smaller symbols are the medium modes observed for the N linker PNA. Error bars are shown for the duplexes studied here representing a single standard deviation of the fitted Gaussian function for the highest observable mode.

Conductance measurements were performed without PNA molecules to establish a background histogram. The details of the control experiments are discussed in Appendix D.

5.3 DISCUSSION

In previous work, the oscillatory effect observed for DNA duplexes of varying lengths was concluded to occur because of coherent contributions to the charge transfer mechanism.¹⁴ However, this effect is considerably diminished when the molecular linker groups are positioned on the opposing termini. In this case, the observed molecular conductance is much greater as well.

The diminished oscillations and increased conductance are attributed to the geometric differences between the charge directionality manifesting in differing G-base coupling values at the center duplex position.²⁰ Thus, for the 3' linker DNA, the cross-strand step dominates the coherent contribution to the charge transport.

The results for the N linker PNA duplexes shows an order of magnitude increase in the molecular conductance compared to the analogous 5' linker DNA. This is consistent with the relationship between DNA and PNA duplexes observed in previous studies.^{26, 33} The oscillatory effect that was observed in the 5' linker DNA system has been dampened or eliminated for the measured duplexes. However, additional experiments are being conducted to improve the signal-to-noise ratio for the shown histograms. It will be interesting to determine the molecular conductance for C linker PNA, for which the structure is analogous to the 3' linker DNA. Whether the C linker PNA shows a further increase in the molecular conductance or the C linker PNA is comparable to the N linker PNA will establish the importance of the cross-strand step in the electron transfer through the duplex.

5.4 METHODS

5.4.1 PNA Synthesis

PNA strands were synthesized and purified following previously reported techniques.²⁶

5.4.2 PNA Characterization

The PNA solutions used for characterization were prepared in 10 mM phosphate buffer (pH 7.0). The melting temperatures of the PNA oligomers were measured using 10 mm path length quartz cells and a Varian Cary 300 spectrophotometer utilizing a temperature block. The concentrations of the solutions were determined by UV-vis absorption following reported procedures.³⁵

5.4.3 Substrate Preparation

100 nm gold films were evaporated onto freshly cleaved mica using an AJA ATC-T Series Thermal Evaporation System. Piranha-cleaned glass slips (10mm x 22mm) were affixed to the gold films (EPO-TEK). Prior to each experiment, a glass slip was peeled from the gold film transferring the film to the glass.³⁶ 50 μ L of 20 μ M PNA duplex solutions were deposited on the gold substrates and allowed to form a diffuse monolayer under a DI water atmosphere for 30 min. The substrates were subsequently rinsed with DI water, rinsed with ethanol, and dried under an Argon stream.

5.4.4 Conductance Measurements

The conductance measurements were performed in an Agilent 5500 scanning probe microscope system using a PicoView interface. The substrates were immersed in 800 μ L of mesitylene (Extra-pure, 99%, Acros Organics). Gold STM tips (0.25 mm, 99.95%, Alfa Aesar) were freshly cut prior to each experiment. The experimental cell was under an argon atmosphere and contained within an environmental chamber. The environmental chamber was housed in a custom-made Faraday cage seated on an anti-vibrational platform (Table Stable). The 50 ± 50 mV modulated bias waveform applied across the tip-substrate gap had a modulation frequency of 500 Hz (DS345 Function Generator, Stanford Research Systems). Currents in the range of 5-1000 nA were sampled using a 100 nA/V preamplifier. The withdrawn speed of the STM tip was 10 nm/sec.

5.4.5 Data Analysis

Conductance data were analyzed following reported procedures utilizing a custom MATLAB script.³⁰ Currents below 5 nA were excluded from the analysis. Current-time trajectories that did not display molecular junctions were removed.

5.5 REFERENCES

1. Genereux, J. C.; Barton, J. K., Mechanisms for DNA Charge Transport. *Chem. Rev.* **2010**, *110* (3), 1642-1662.
2. Korol, R.; Segal, D., From Exhaustive Simulations to Key Principles in DNA Nanoelectronics. *J. Phys. Chem. C* **2018**, *122* (8), 4206-4216.
3. Lewis, F. D.; Wu, T.; Zhang, Y.; Letsinger, R. L.; Greenfield, S. R.; Wasielewski, M. R., Distance-Dependent Electron Transfer in DNA Hairpins. *Science* **1997**, *277* (5326), 673-676.
4. Fink, H.-W.; Schönenberger, C., Electrical conduction through DNA molecules. *Nature* **1999**, *398*, 407.
5. O., K. S.; M., J. N.; G., H. M.; K., B. J., Long-Range Electron Transfer through DNA Films. *Angew. Chem. Int. Ed.* **1999**, *38* (7), 941-945.
6. Giese, B.; Amaudrut, J.; Köhler, A.-K.; Spormann, M.; Wessely, S., Direct observation of hole transfer through DNA by hopping between adenine bases and by tunnelling. *Nature* **2001**, *412*, 318.
7. Xu, B. Q.; Zhang, P. M.; Li, X. L.; Tao, N. J., Direct conductance measurement of single DNA molecules in aqueous solution. *Nano Lett.* **2004**, *4* (6), 1105-1108.
8. Risser, S. M.; Beratan, D. N.; Meade, T. J., Electron transfer in DNA: predictions of exponential growth and decay of coupling with donor-acceptor distance. *J. Am. Chem. Soc.* **1993**, *115* (6), 2508-2510.
9. Jortner, J.; Bixon, M.; Langenbacher, T.; Michel-Beyerle, M. E., Charge transfer and transport in DNA. *Proc. Natl. Acad. Sci. U S A* **1998**, *95* (22), 12759-65.
10. Renaud, N.; Berlin, Y. A.; Lewis, F. D.; Ratner, M. A., Between Superexchange and Hopping: An Intermediate Charge-Transfer Mechanism in Poly(A)-Poly(T) DNA Hairpins. *J. Am. Chem. Soc.* **2013**, *135* (10), 3953-3963.
11. Berlin, Y. A.; Burin, A. L.; Ratner, M. A., Charge Hopping in DNA. *J. Am. Chem. Soc.* **2001**, *123* (2), 260-268.
12. Kilgour, M.; Segal, D., Charge transport in molecular junctions: From tunneling to hopping with the probe technique. *J. Chem. Phys.* **2015**, *143* (2), 024111.
13. Venkatramani, R.; Davis, K. L.; Wierzbinski, E.; Bezer, S.; Balaeff, A.; Keinan, S.; Paul, A.; Kocsis, L.; Beratan, D. N.; Achim, C.; Waldeck, D. H., Evidence for a Near-Resonant Charge Transfer Mechanism for Double-Stranded Peptide Nucleic Acid. *J. Am. Chem. Soc.* **2011**, *133* (1), 62-72.
14. Xiang, L.; Palma, J. L.; Bruot, C.; Mujica, V.; Ratner, M. A.; Tao, N., Intermediate tunnelling–hopping regime in DNA charge transport. *Nat. Chem.* **2015**, *7* (3), 221-226.
15. Smit, R. H. M.; Untiedt, C.; Rubio-Bollinger, G.; Segers, R. C.; van Ruitenbeek, J. M., Observation of a Parity Oscillation in the Conductance of Atomic Wires. *Phys. Rev. Lett.* **2003**, *91* (7), 076805.
16. Tada, T.; Nozaki, D.; Kondo, M.; Hamayama, S.; Yoshizawa, K., Oscillation of Conductance in Molecular Junctions of Carbon Ladder Compounds. *J. Am. Chem. Soc.* **2004**, *126* (43), 14182-14189.
17. Qiu, M.; Liew, K. M., Odd–Even Effects of Electronic Transport in Carbon-Chain-Based Molecular Devices. *J. Phys. Chem. C* **2012**, *116* (21), 11709-11713.
18. Baghbanzadeh, M.; Simeone, F. C.; Bowers, C. M.; Liao, K.-C.; Thuo, M.; Baghbanzadeh, M.; Miller, M. S.; Carmichael, T. B.; Whitesides, G. M., Odd–Even

- Effects in Charge Transport across n-Alkanethiolate-Based SAMs. *J. Am. Chem. Soc.* **2014**, *136* (48), 16919-16925.
19. Buttiker, M., Coherent and sequential tunneling in series barriers. *IBM J. Res. Dev.* **1988**, *32* (1), 63-75.
 20. Liu, C.; Xiang, L.; Zhang, Y.; Zhang, P.; Beratan, D. N.; Li, Y.; Tao, N., Engineering nanometre-scale coherence in soft matter. *Nat. Chem.* **2016**, *8* (10), 941-945.
 21. Di Felice, R.; Calzolari, A.; Molinari, E.; Garbesi, A., Ab initio study of model guanine assemblies: The role of π - π coupling and band transport. *Phys. Rev. B* **2001**, *65* (4), 045104.
 22. Šponer, J.; Leszczyński, J.; Hobza, P., Nature of Nucleic Acid–Base Stacking: Nonempirical ab Initio and Empirical Potential Characterization of 10 Stacked Base Dimers. Comparison of Stacked and H-Bonded Base Pairs. *J. Phys. Chem.* **1996**, *100* (13), 5590-5596.
 23. Hatcher, E.; Balaeff, A.; Keinan, S.; Venkatramani, R.; Beratan, D. N., PNA versus DNA: effects of structural fluctuations on electronic structure and hole-transport mechanisms. *J. Am. Chem. Soc.* **2008**, *130* (35), 11752-61.
 24. Venkatramani, R.; Keinan, S.; Balaeff, A.; Beratan, D. N., Nucleic acid charge transfer: Black, white and gray. *Coord. Chem. Rev.* **2011**, *255* (7-8), 635-648.
 25. Wierzbinski, E.; de Leon, A.; Yin, X.; Balaeff, A.; Davis, K. L.; Rapireddy, S.; Venkatramani, R.; Keinan, S.; Ly, D. H.; Madrid, M.; Beratan, D. N.; Achim, C.; Waldeck, D. H., Effect of Backbone Flexibility on Charge Transfer Rates in Peptide Nucleic Acid Duplexes. *J. Am. Chem. Soc.* **2012**, *134* (22), 9335-9342.
 26. Beall, E.; Ulku, S.; Liu, C.; Wierzbinski, E.; Zhang, Y.; Bae, Y.; Zhang, P.; Achim, C.; Beratan, D. N.; Waldeck, D. H., Effects of the Backbone and Chemical Linker on the Molecular Conductance of Nucleic Acid Duplexes. *J. Am. Chem. Soc.* **2017**, *139* (19), 6726-6735.
 27. Egholm, M.; Buchardt, O.; Nielsen, P. E.; Berg, R. H., Peptide nucleic acids (PNA). Oligonucleotide analogs with an achiral peptide backbone. *J. Am. Chem. Soc.* **1992**, *114* (5), 1895-1897.
 28. Egholm, M.; Buchardt, O.; Christensen, L.; Behrens, C.; Freier, S. M.; Driver, D. A.; Berg, R. H.; Kim, S. K.; Norden, B.; Nielsen, P. E., PNA hybridizes to complementary oligonucleotides obeying the Watson–Crick hydrogen-bonding rules. *Nature* **1993**, *365* (6446), 566-568.
 29. Xu, B.; Tao, N. J., Measurement of Single-Molecule Resistance by Repeated Formation of Molecular Junctions. *Science (Washington, DC, U. S.)* **2003**, *301* (5637), 1221-1223.
 30. Beall, E.; Yin, X.; Waldeck, D. H.; Wierzbinski, E., A scanning tunneling microscope break junction method with continuous bias modulation. *Nanoscale* **2015**, *7* (36), 14965-14973.
 31. van Wees, B. J.; van Houten, H.; Beenakker, C. W.; Williamson, J. G.; Kouwenhoven, L. P.; van der Marel, D.; Foxon, C. T., Quantized conductance of point contacts in a two-dimensional electron gas. *Phys. Rev. Lett.* **1988**, *60* (9), 848-850.
 32. Li, C.; Pobelov, I.; Wandlowski, T.; Bagrets, A.; Arnold, A.; Evers, F., Charge Transport in Single Au | Alkanedithiol | Au Junctions: Coordination Geometries and Conformational Degrees of Freedom. *J. Am. Chem. Soc.* **2008**, *130* (1), 318-326.

33. Haiss, W.; Martín, S.; Leary, E.; Zalinge, H. v.; Higgins, S. J.; Bouffier, L.; Nichols, R. J., Impact of Junction Formation Method and Surface Roughness on Single Molecule Conductance. *J. Phys. Chem. C* **2009**, *113* (14), 5823-5833.
34. Beall, E.; Sargun, A.; Ulku, S.; Bae, Y.; Wierzbinski, E.; Clever, C.; Waldeck, D. H.; Achim, C., Molecular Conductance of Nicked Nucleic Acid Duplexes. *J. Phys. Chem. C* **2018**, *122* (13), 7533-7540.
35. *Peptide Nucleic Acids: Protocols and Applications*. Horizon Bioscience: Wymondham, U.K., 2004.
36. Hegner, M.; Wagner, P.; Semenza, G., Ultralarge atomically flat template-stripped Au surfaces for scanning probe microscopy. *Surf. Sci.* **1993**, *291* (1-2), 39-46.

6.0 CONCLUDING REMARKS

The work presented in this dissertation represents fundamental research towards functional bioelectronics. Advancement of the molecular electronics field depends on elucidation of the central charge transfer mechanisms and the underlying factors affecting charge transport on the nanoscale. The projects described here have uncovered the important role played by the molecular flexibility, the electrode-molecule contact, and the nucleobase energetic order on charge transport and advances the field towards the realization of molecular electronics comprising biomolecules.

Chapter 2 presented a technique that modifies the existing methods to measure single molecule conductance through the use of a modulated bias. The application of a triangular voltage waveform and DC bias allows for the current-voltage characteristics of molecules to be measured to a statistical degree during a single experiment. For the test molecule, octanedithiol, this method was shown to replicate the conductance characteristics found for the constant bias method but benefit from better sampling of the lowest observable conductance mode. Because of the modulated bias, a clear distinction between the current response arising from the molecule and that of the solvent is often present. The current responses were fit to a model RC circuit and the solvent contribution was excluded. The nature of the current responses also allowed them to be easily partitioned by the modulation periods for use in subsequent analyses. The use of a modulated bias allows for a broader range of potential analyses of single molecule conductance and represents a step towards molecular circuits functioning under alternating current.

Chapter 3 discussed a study showing the effect of molecular flexibility of nucleic acid duplexes on their single molecule conductance. A series of nucleic acid duplexes with varying degrees of backbone flexibility were measured using the method presented in Chapter 2. The results showed that increasing the flexibility of the nucleic acid backbone increased the single

molecule conductance. A hypothesis regarding conformational fluctuations was presented and a computational study of duplex parameters was performed to offer an explanation for the increased conductance. The trend in the standard deviations of the average structural parameters was consistent with the trend in the measured single molecule conductance. The effect of molecular linkers was also shown, with linkers that inject charges directly into the nucleic acid backbone showing a larger conductance than those that only inject charge into the backbone. The elucidation of the role of flexibility on the single molecule conductance has far-reaching implications on not only the field of molecular electronics, but any molecular systems where conformational gating can affect charge transport.

Chapter 4 expanded on the work shown in Chapter 3, where the effect of a nick in the backbone of a nucleic acid duplex was studied. DNA homoduplexes and DNA/PNA heteroduplexes were compared to respective versions with a nick in the backbone. The average single molecule conductance was shown to be unaffected by the presence of the nick; however, the conductance was shown to be more variable between periods of the same current response trajectory. The longevity of the molecular junction was also shown to be compromised by the nick in the duplex. Further, a comparison of reported DNA conductance values involving a treatment of the effective length was presented. The single molecule conductance of DNA duplexes was shown to have an exponential dependence with the number of AT base pairs in the duplex, disregarding the number of GC base pairs. The effect of the nick supports the prospect of constructing complex molecular circuits from smaller nucleic acid components; however, mitigating variability and lessened longevity are issues that future efforts will need to address.

Chapter 5 presented ongoing work to elucidate the relationship between coherence and incoherence in nucleic acid charge transfer. The single molecule conductance of PNA duplexes of

varying lengths were measured and the length dependence was compared to previous studies on DNA duplexes. The oscillatory effect observed for DNA duplexes was shown to be considerably dampened for the more flexible nucleic acids. This suggests that the charge delocalization that caused the oscillations in the DNA systems is dominated by the cross-strand hopping event at the midpoint of the PNA duplex.

The work presented in this dissertation has established the effects of several parameters governing charge transport in single molecule systems. While central studies such as these lay the groundwork for molecular circuitry, there is still much that needs to be revealed. A unifying mechanism for charge transport is still being sought and experimental conditions are being explored that create stable, long-lived molecular junctions. The existence of multiple conductance modes and a possible voltage-dependent resistance have complicated the picture of single molecules as circuit components. There have been significant accomplishments in achieving molecular platforms that can replicate the electrical behavior of macroscopic circuit components; however, the field of functional bioelectronics is still in its infancy. Progress in this milieu will utilize the work presented here and the fundamental studies therein to advance the capability of molecular constructs and lead to the realization of molecular electronics.

APPENDIX A:
SUPPORTING INFORMATION FOR CHAPTER 2

**A.1 CURRENT RESPONSE OF THE SOLVENTS ON THE BIAS APPLIED WITH
VARIOUS MODULATION FREQUENCIES**

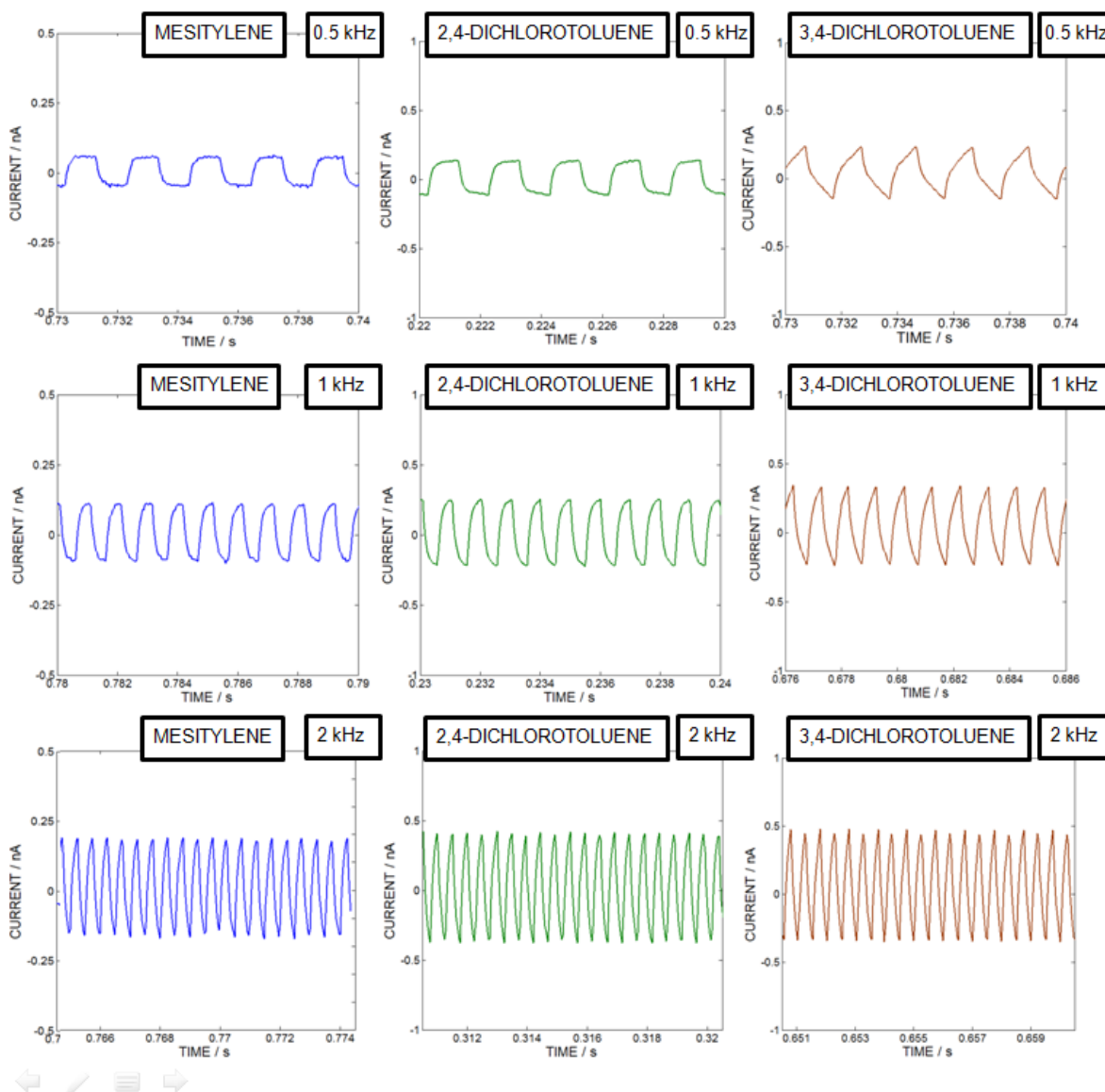


Figure A.1. Current-time traces in the solvent regime recorded for mesitylene, 2,4-dichlorotoluene, and 3,4-dichlorotoluene at 0.5, 1, and 2 kHz frequency of the 0.3 ± 0.3 V bias modulation.

Figure A.2 shows the capacitance values associated with the solvent in the model electrical circuit (Figure 2.4) used for the simulation of the current responses for the data shown in Figure A.1. We note that the current response of the solvent, and therefore its capacitance, is highly dependent on the purity of the solvent. The mesitylene and 2,4-dichlorotoluene were used as received. The 3,4-dichlorotoluene was purified by fractional distillation under argon. Using unpurified 3,4-dichlorotoluene resulted in about a two-fold increase in the amplitude of the current oscillations and 2.5 higher capacitance (data not shown). Similarly, the amplitude of the current response of the mesitylene saturated intentionally with deionized water (data not shown) was over fifty percent higher than that of pure (99+ %) solvent.

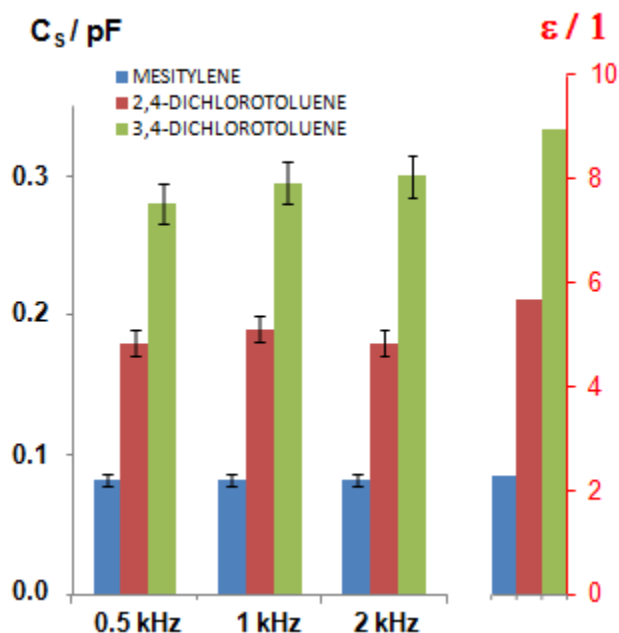


Figure A.2. Dependence of the solvents capacitance simulated using the model electrical circuit (Figure 4 in manuscript) on the bias modulation frequency. The error is estimated as 5%. The data is compared to the dielectric constant values adapted from refs 1 and 2.

For our experimental setup, we determined RC time constants of $\sim 75 \mu\text{s}$ for mesitylene, $90 \mu\text{s}$ for 2,4-dichlorotoluene, and $225 \mu\text{s}$ for 3,4-dichlorotoluene. These values correspond to

frequency cutoffs of ~ 2.15 kHz for mesitylene, 1.75 kHz for 2,4-dichlorotoluene, and 0.7 kHz for 3,4-dichlorotoluene.

A.2 INFLUENCE OF MACROSCOPIC GEOMETRICAL FACTORS ON THE CAPACITIVE CURRENT WAVEFORMS

The capacitor formed between the scanner holding the STM tip and the substrate is macroscopic in comparison to the junction itself; therefore, small changes in the tip-substrate separation in comparison to the dimensions of the electrodes have no effect on the capacitive current waveform. The influence of major geometrical factors on the capacitive current waveform is given in figures A.3-A.5.

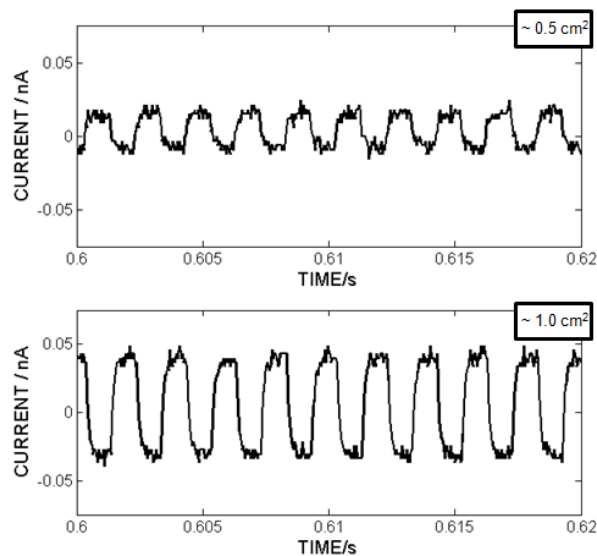


Figure A.3. Current-time traces recorded in air above the gold substrates with different geometrical surface areas. The traces were recorded at 0.5 kHz frequency of the 0.3 ± 0.3 V bias modulation. The STM tip – substrate separation was of about 300 μm .

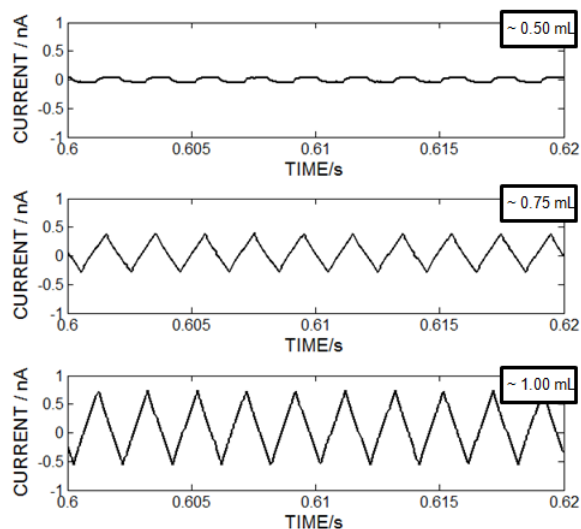


Figure A.4. Current-time traces recorded in the cell filled with different volumes of the 3,4-dichlorotoluene. The traces were recorded at 0.5 kHz frequency of the 0.3 ± 0.3 V bias modulation, with the STM tip – substrate separation of about 300 μm . Subsequent additions of the 0.25 mL of the solvent were made to cell. Note that first additions with total solvent volume below 0.75 mL were not sufficient to cover the surface of the gold substrate with solvent.

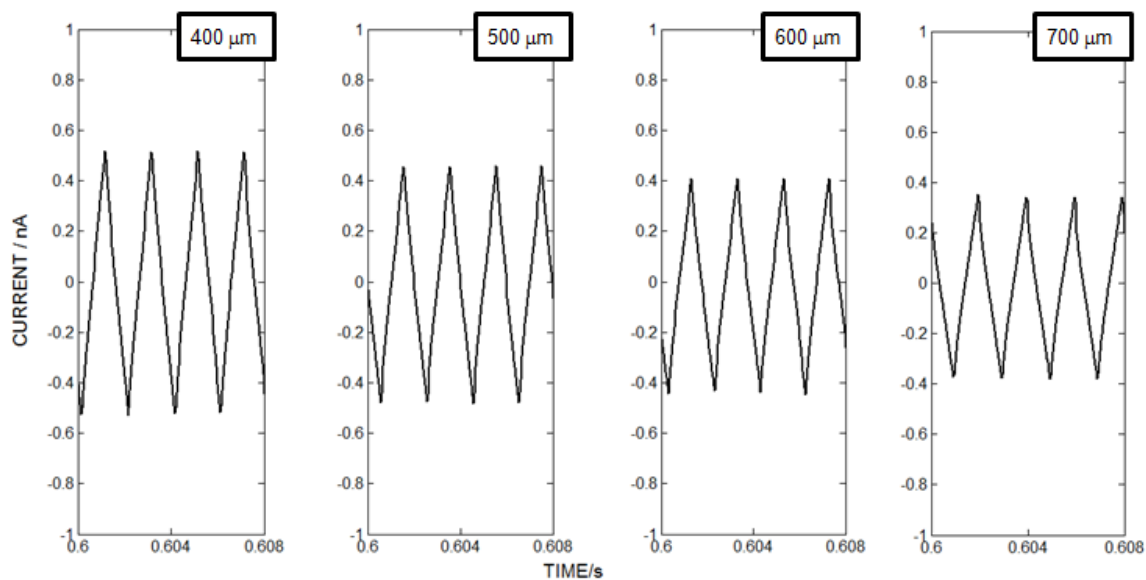


Figure A.5. The current-time traces recorded at different STM tip – substrate separations. The traces were recorded at 0.5 kHz frequency of the 0.3 ± 0.3 V bias modulation, in the cell filled with 1 mL of 3,4-dichlorotoluene. Note that the separation is micrometers in length scale, thus a decrease in the current waveform amplitude originates from the decrease of the amount of the gold wire forming the tip that was immersed in the solvent.

A.3 REFERENCES

1. *CRC Handbook of Chemistry and Physics 84th Ed.*, CRC Press, Boca Raton, FL, 2003.
2. R. R. Dreisbach, in *Physical Properties of Chemical Compounds*, American Chemical Society, 1961, vol. 15, ch. 1, pp. 3-523.

APPENDIX B:
SUPPORTING INFORMATION FOR CHAPTER 3

B.1 SOLID-PHASE PNA SYNTHESIS

Table B.1. PNA sequences and MALDI data.

N to C end Sequence of PNA oligomers			
<u>Thiol on the C end Lys on the N end</u>		Cal. MW	Obs. MW
<u>PNA4_{N-Lys+C-SH}</u>	H-Lys AGT TTG TAC G-SH	2959.98	2983.81
<u>PNA5_{N-Lys+C-SH}</u>	H-Lys CGT ACA AAC T-SH	2921.33	2921.63
<u>Thiol on the C end</u>			
<u>PNA4_{C-SH}</u>	Ac AGT TTG TAC G-SH	2874.67	2875.25
<u>PNA5_{C-SH}</u>	Ac CGT ACA AAC T-SH	2814.65	2814.78
<u>Thiol on the N end</u>			
<u>PNA4_{N-SH}</u>	SH-AGT TTG TAC G NH ₂	2860.67	2858.00
<u>PNA5_{N-SH}</u>	SH-CGT ACA AAC T NH ₂	2798.65	2797.03
<u>Thiol on the N end (gamma modified)</u>			
<u>γPNA4_{N-SH}</u>	SH-AGT TTG TAC G-NH ₂	3160.67	3159.71
<u>γPNA5_{N-SH}</u>	SH-CGT ACA AAC T-NH ₂	3098.65	3098.34
<u>Amino linker on the N end</u>			
<u>PNA4_{N-T-C2-NH2}</u>	H-T _(C2-NH2) (dap) AGT TTG TAC G A-NH ₂	3384.38	3381.43
<u>PNA5_{N-T-C2-NH2}</u>	H-T _(C2-NH2) (dap) CGT ACA AAC T A-NH ₂	3322.26	3319.62

- * Ac shows N-end acetylation
- ** Underlined letters shows γ -modified PNA monomers
- ***SH stands for propylthiol linker
- **** Dap= 3-amino-L-Alanine

PT stands for propylthiol linker used to anchor the PNA to the gold surface. This linker was introduced at either the N-end or C-end of the PNA.

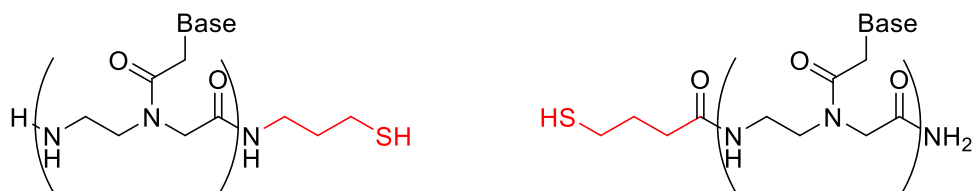


Figure B.1. C-end (a) and N-end (b) thiol-modified PNA. The propylthiol is used to anchor the PNA to the Au surface is shown in red.

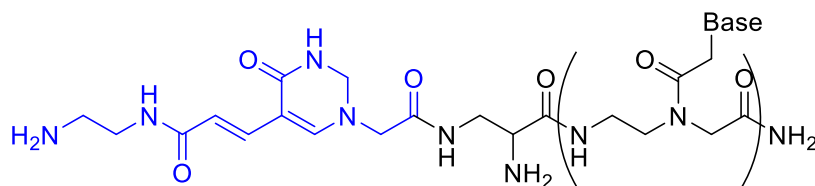


Figure B.2. N-end $T_{(C2-NH_2)}$ modified PNA. The thymidine 5-C2 amino linker is used to anchor the PNA to the gold surface is shown in blue.

$T_{(C2-NH_2)}$ stands for thymidine 5-C2 amino linker used to anchor the PNA to the gold surface. Acetic acid of $T_{(C2-NH_2)}$ linker, **10** could be introduced at either the N-end or C-end of the PNA as the side chain of (**Boc-3-(Fmoc-amino)-L-alanine**).

B.1.1 General Procedures

All reactions were performed under nitrogen atmosphere unless otherwise stated. All commercially available materials were used without further purification unless otherwise specified. Anhydrous solvents, purchased from EMD Millipore, such as DMF, DCM and THF, were dried by standard methods and freshly distilled prior to use. All anhydrous reagents were purchased from Aldrich. Common reagents were purchased from either Chem-Impex or Alfa Aesar. $^1\text{H-NMR}$ and $^{13}\text{C-NMR}$ spectra were acquired on a Bruker Avance AV-300 or 500 MHz NMR spectrometer using standard Bruker software.

Boc/Z and Fmoc/Bhoc PNA monomers were purchased from PolyOrg Inc. and ASM Research Chemicals and used without further purification. PNA strands were purified by reverse-phase HPLC using a C18 column (5 μ m; 19 \times 100 mm; Waters Corporation, Milford, MA) and were subsequently lyophilized for long-term storage. Characterization of the oligomers was performed by MALDI-TOF on an Applied Biosystems Voyager Biospectrometry Workstation using R-cyano-4-hydroxycinnamic acid matrix (10 mg/mL in 1:1 water/acetonitrile, 0.1% TFA).

B.1.2 Synthesis of Propyl Thiol Linker Containing PNAs

4-(Tritylthio)butyric acid, which was necessary for the N-end modification of PNA with the thiol linker, was synthesized using a published procedure.¹ The PNA oligomers with N-end propyl thiol were synthesized using the Boc strategy; the PNA oligomers with C-end propyl thiol were synthesized by the Fmoc strategy. A p-methyl-benzhydrylamine (MBHA) resin purchased from Peptide International was used for the Boc strategy and PNA oligomers were synthesized manually by standard solid phase peptide synthesis methods. The MBHA resin (1.0 g) was downloaded to 0.1 mmol/g with the first monomer.

The PT modification at the C-end of PNA was afforded by using 2-chlorotrityl resin purchased from AnaSpec, and this resin was downloaded with 3-Amino-1-propanethiol hydrochloride purchased from Sigma Aldrich as described in a published protocol (Figure B.3).² 3-Amino-1-propanethiol hydrochloride (2 eq.) and DIPEA (2 eq.) dissolved in anhydrous (DCM/DMF 1:1) (10 ml per gram of resin) were added to 2-chlorotrityl resin. The suspension was stirred at RT for 5 h. At the end of the reaction, the resin was filtered and washed with 3xDCM. To ensure that 3-Amino-1-propanethiol was not attached to the resin through its amino group, the resin was treated with a mixture of acetic acid AcOH/trifluoroethanol (TFE)/DCM (1:2:7) for 30 min at rt. This mixture cleaves the aminotrityl bond effectively. Unreacted remaining trityl

chlorides were converted to the corresponding inert tritylmethyl ethers by washing resin with DCM/MeOH/DIPEA (80:15:5). A qualitative positive Kaiser test [in a 1.5 mL centrifuge tube, added a few beads of resin 1 drop of Monitor 1 (8g of phenol dissolved in 2 mL EtOH) and 2 drops of Monitor 2 (13 mg KCN/20 mL water. Dilute 200 μ L of KCN aqueous solution with 9800 μ L L pyridine)] and 1 drops Monitor 3 (1 g ninhydrin in 20 mL ethanol) was used to confirm the presence of free amines on the 2-chlorotrityl resin. In order to check the loading of the 2-chlorotrityl resin with the PT linker, PT downloaded resin was coupled with Boc-Lys(Fmoc)-OH. After, deprotection of the Fmoc- group on an accurately weighed sample, amount of released Fmoc- was measured by UV-vis spectrometry photometrically.

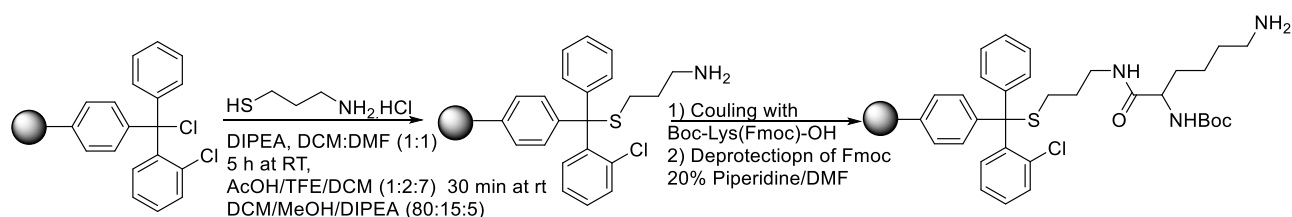


Figure B.3. Loading of the 2-chlorotrityl resin with the PT linker.

The PNA was cleaved using TFMSA/TFA/m-cresol/thioanisole (20:60:10:10) and TFA/triisopropylsilane/water (95:2.5:2.5) for the Boc and Fmoc strategies, respectively. Cleaved PNA was precipitated with cold diethyl ether. PNA strands were purified by reverse-phase HPLC and were lyophilized. Characterization of the oligomers was performed by MALDI-TOF using an R-cyano-4-hydroxycinnamic acid matrix (10 mg/mL in 1:1 water/acetonitrile, 0.1% TFA).

B.1.3 Synthesis of 4-(Tritylthio)Butyric Acid

In order to make a thiol linker on the N end of a PNA oligomer, compound **3** had to be made. Synthesis of compound **3** could be accomplished using a published procedure.¹ S-alkylation of commercially available trityl mercaptan **1** with 4-bromo butyric acid **2** in the presence of NaH in DMF gave compound **3** in high 91 % yield.

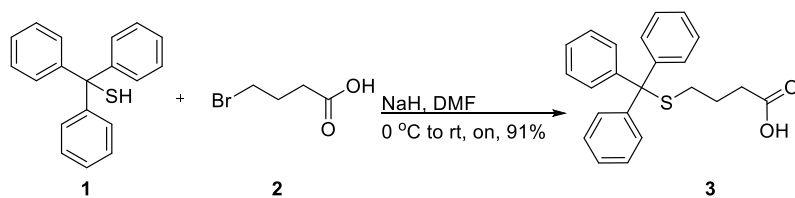


Figure B.4. S-alkylation of trityl mercaptan **1**.

Trityl mercaptan **1** (1) 93.3 g, 11.97 mmol) was added stepwise to a suspension of NaH (1.05 g, 26.33 mmol) in 10 mL DMF under a nitrogen atmosphere at 0 °C. After completion of the addition, the reaction mixture was stirred for 30 min. A solution of a 4-bromo butyric acid **2** in 15 mL DMF was added slowly. After addition was completed, the reaction mixture was stirred for 30 minutes before the temperature was gradually increased to room temperature and then stirred overnight. Then, 200 mL chloroform was added to the reaction mixture and the reaction mixture was washed with 4x(100 mL) NaHSO₄ and 4x(100 mL) H₂O. The organic layer was evaporated and the remaining oil was precipitated by addition of distilled water and solid product was collected by suction filtration. The crude powder then stirred in petroleum ether for a few minutes. The solid was collected by filtration to give a white powder **3** (3.95 g, 10.91 mmol, 91%). ¹H NMR (300 MHz, CDCl₃) δ(ppm) 7.5-7.2(m, 15 H), 2. (t, 2 H, *J*= 7.2 Hz), 2.2 (t, 2 H, *J*=7.2 Hz), 1.67 (quint, 2 H, *J*=7.2 Hz); ¹³C NMR (500 MHz, DMSO-*d*₆) δ (ppm) 173.7, 140.2, 125.0, 123.2, 121.9, 62.0, 28.2, 26.6, 18.9. ESI-MS (positive ion mode) calcd for C₂₃H₂₂O₂S [M+H]⁺ 362; found 362.

B.1.4 Synthesis of T_(C2-NH2) Linker Containing PNAs

The T_(C2-NH₂) functionalized PNA oligomers were synthesized manually on Rink-amide AM resin purchased from Novabiochem following the standard Fmoc procedures of solid-phase peptide synthesis. T_(C2-NH₂) acedic acid linker was added on the N-end of a PNA oligomer as the side chain of the Boc-DAP(Fmoc)-OH (**Boc-3-(Fmoc-amino)-L-alanine**) amino acid which was purchased from Sigma-Aldrich.

Upon completion of the oligomer synthesis, the oligomers were cleaved from the resin by immersing the resin in a cocktail containing TFA/DCM/TIS (10:85:5) for 30 min and the deprotection of side chain was effected by 50% TFA-DCM (TIS used as scavenger) for 1 h. Cleaved PNA was precipitated with cold diethyl ether. PNA strands were purified by reverse-phase HPLC and were lyophilized. Characterization of the oligomers was performed by MALDI-TOF using R-cyano-4-hydroxycinnamic acid matrix (10 mg/mL in 1:1 water/acetonitrile, 0.1% TFA).

B.1.5 Synthesis of Thymidine 5-C2 Amino Linker

Thymidine 5-C2 amino linker was synthesized using a modified published procedure.³ Commercially available iodouracil **4** was alkylated at N1 with ethyl bromoacetate **5** in the presence of potassium carbonate in anhydrous DMF under nitrogen at room temperature for 24 h to give ethyl ester **6** in quantitative yield. The iodo group of **6** was exchanged with an acryloyl group via the Heck reaction with acrylic acid **7** to give the carboxylic acid **8** in 60 % yield. Next, coupling of carboxylic acid **8** with Boc-protected ethylenediamine **9** by activation with HATU in the presence of DIEA in anhydrous DMF, and hydrolysis of resulting ethyl ester to carboxylic acid using LiOH led to the final product **10** in 75 % yield over last two steps (Figure B.5).

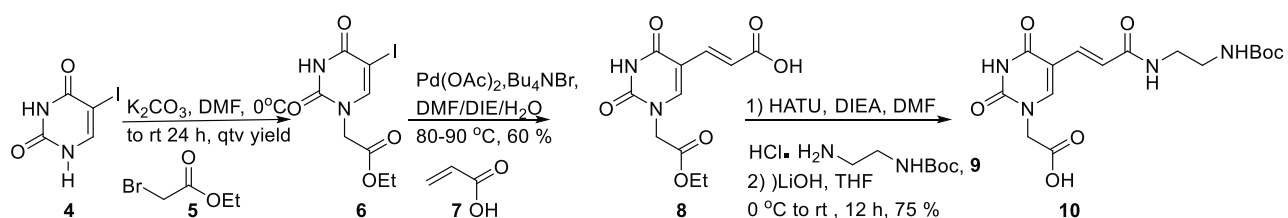


Figure B.5. Synthesis of Thymidine 5-C2 Amino Linker.

Ethyl 2-(5-iodo-2,4-dioxo-3,4-dihydropyrimidin-1(2H)-yl)acetate **6**: Ethyl bromoacetate **5** (0.83 g, 5 mmol) in anhydrous DMF (2.5 mL) was slowly added via syringe under a nitrogen

atmosphere to a suspension of iodouracil (1.9 g, 5 mmol) and anhydrous K₂CO₃ (0.76 g, 55 mmol) in anhydrous DMF (17.5 mL) at 0°C in an oven-dried round bottom flask. The resulting reaction mixture was gradually warmed up to rt and vigorously stirred for 24 h. The reaction progress was monitored by TLC (5% DCM/MeOH). The byproduct precipitate of KBr salt was filtered under vacuum and washed with 2 mL of DMF. The solvent was evaporated under vacuum, and diluted with EtOAc (20 mL) and washed with water (3 × 100 mL). The aqueous phase was back extracted with EtOAc (3 × 100 mL). The combined organic layers dried over Na₂SO₄, and concentrated to 10 mL on rotovap. To this solution a few drops of hexane was added and as a result a pale yellow solid formed. The solid was then filtered over vacuum and washed with water and cold diethyl ether. Yielding product **6** (1.7 g, 5.2 mmol) was dried over vacuum and used for the next step without further purification. ¹H NMR (500 MHz, DMSO-*d*₆) δ (ppm): 11.8 (s, 1 H), 8.2 (s, 1 H), 4.5 (s, 2 H), 4.2 (q, 2 H, *J* = 7.1 Hz), 1.2 (t, 3 H, *J* = 7.1 Hz); ¹³C NMR (500 MHz, DMSO-*d*₆) δ (ppm) 168.4, 161.4, 151.1, 150.5, 68.8, 61.9, 49.2, 14.4. ESI-HRMS (positive ion mode) calcd for C₈H₉IN₂O 324.07; found 324.96.

(E)-3-(1-(2-ethoxy-2-oxoethyl)-2,4-dioxo-1,2,3,4-tetrahydropyrimidin-5-yl)acrylic acid **8**

To a clean, dry 100 mL round-bottom flask was added ethyl 2-(5-iodo-2,4-dioxo-3,4-dihydropyrimidin-1(2H)-yl)acetate **6** (1.0 g, 3.1 mmol) and N-tetrabutylammonium bromide (1.2 g, 3.7 mmol), and dissolved in anhydrous DMF (13 mL). The flask was evacuated and kept under nitrogen atmosphere. Then, the Pd(OAc)₂ catalyst (0.21 g, 0.94 mmol), was added under nitrogen. A mixture of DMF/H₂O/DIEA (10:10:10 mL) was added via syringe, and the reaction was evacuated (freed of any oxygen gas) and stirred at rt under nitrogen. Last, acrylic acid **7** (2.16 g, 30 mmol) in dry DMF (10 mL) was slowly added to the reaction mixture via a stainless steel syringe under nitrogen. The reaction mixture was then heated to 80-90 °C in an oil bath for 16 h.

The reaction mixture turned black for the first few hours, and then palladium particles precipitated while the solution turned yellow. The black particles were filtered under vacuum, and the DMF was evaporated under vacuum at 45°C. The reaction mixture was then dissolved in water (5 mL) and extracted with diethyl ether (5 × 50 mL). The organics were combined, dried over Na₂SO₄, and evaporated to give the crude product as yellow oil. The product was then precipitated by adding a few drops of hexane in an ice bath. The pale yellow powder **8** (0.5 g, 1.9 mmol, 60 %) was collected by vacuum filtration in a sintered glass funnel and dried under vacuum. ¹H NMR (500 MHz, DMSO-*d*₆) δ (ppm): 12.2 (s, 1 H); 11.8 (s, 1 H), 8.2 (s, 1 H), 7.2 (d, 2 H, *J*= 15.9 Hz), 6.7 (d, 2 H, *J*= 15.9 Hz), 4.6 (s, 2 H), 4.2 (q, 2 H, *J*= 7.1 Hz), 1.2 (t, 3 H, *J*= 7.1 Hz); ¹³C NMR (500 MHz, DMSO-*d*₆) δ (ppm) 168.3, 162.9, 150.4, 149.0, 137.0, 118.6, 108.5, 61.8, 49.6, 14.5. ESI-HRMS (negative ion mode) calcd for C₁₁H₁₂N₂O₆ 268.23; found 267.04.

(E)-2-(5-(3-((2-((tert-butoxycarbonyl)amino)ethyl)amino)-3-oxoprop-1-en-1-yl)-2,4-dioxo-3,4-dihydropyrimidin-1(2H)-yl)acetic acid **10**: To a stirred solution of (E)-3-(1-(2-ethoxy-2-oxoethyl)-2,4-dioxo-1,2,3,4-tetrahydropyrimidin-5-yl)acrylic acid **8** (0.70 g, 2.6 mmol) in anhydrous DMF (10 mL) were added DIEA (0.74 g, 5.7 mmol) HATU (1.18 g, 3.12 mmol) under nitrogen atmosphere. Reaction mixture was stirred at 0 °C for 30 min. Then, hydrochloric acid salt of tert-butyl (2-aminoethyl) carbamate **9** (0.43 g, 2.2 mmol) in dry DMF (2 mL) was slowly added to the reaction mixture via a stainless steel syringe under nitrogen. The reaction mixture was warmed up to rt and stirred for 12 h. The reaction completion was checked by TLC. The DMF was evaporated at 45°C under vacuum. The crude product was dissolved in water and extracted with ethyl acetate (5x 100 mL). The organics were combined, dried over Na₂SO₄, and evaporated to give the crude product **10** as yellow oil. The product was used for the next step without further purification.

LiOH (0.39 g) in 8 mL H₂O at 0 °C was added dropwise to a stirred solution of crude product **10** obtained from earlier step (0.57 g, 1.90 mmol) in THF (8 mL). After stirring 30 min at the same temperature, the reaction mixture was warmed up to rt and stirred overnight. Then, water (2.5 mL) was added and the pH was adjusted to 4, at which point, a precipitate was formed. The precipitate was filtered and washed with hexane (3x5 mL) and diethyl ether (3x5 mL), respectively. The product obtained was dried under vacuum (0.54g, 1.42 mmol, 75 %). ¹H NMR (500 MHz, DMSO-*d*₆) δ (ppm): 11.5 (s, 1 H), 8.1 (t, 1 H, *J*= 5.8 Hz), 8.0 (s, 1 H), 7.0 (d, 1 H, *J*= 15.5 Hz), 6.9 (d, 1 H, *J*= 15.4 Hz), 6.8(t, 1 H, *J*= 5.0 Hz), 4.2 (s, 2 H), 3.0 (t, 2 H, *J*= 6.3 Hz), 3.2 (d, 2 H, *J*= 6.2 Hz), 1.4 (s, 9 H). ¹³C NMR (500 MHz, DMSO-*d*₆) δ (ppm) 169.6, 166.3, 162.8, 156.1, 150.4, 149.2, 132.4, 121.4, 108.3, 78.1, 50.4, 40.3, 39.3, 28.7. ESI-MS (positive ion mode) calcd for C₁₆H₂₂N₄O₇ 382.3; found 382.7.

B.2 CONDUCTANCE MEASUREMENTS

B.2.1 Equipment

All measurements were performed with an Agilent 5500 Scanning Probe Microscope system. An environmental chamber was housed in a homemade acoustically isolated Faraday cage and mounted on an anti-vibrational table (Table Stable). All measurements were performed using a Stanford Research Systems DS345 function generator and a 10 nA/V preamplifier.

B.2.2 Nucleic Acid Duplexes

The DNA oligomers were purchased from Integrated DNA Technologies or Alpha DNA, and the PNA strands were synthesized by the procedures described above. Solutions containing 20 μM of each nucleic acid strand in pH=7.0 Tris-EDTA buffer were heated to 90°C for 10 minutes and then allowed to cool to room temperature over 2-3 hours. Duplex formation was confirmed through absorbance and circular dichroism spectroscopy.

B.2.3 Gold Substrates

The ultraflat gold substrates were prepared using the template-stripping process.⁴ 100 nm gold films were evaporated onto freshly-cleaved mica using an AJA ATC-T Series Thermal Evaporation System. Piranha-cleaned glass slips (10 mm x 25 mm) were glued to the gold films using epoxy resin (Epo-Tek). The glass slips were peeled off the gold film prior to each experiment and the film was transferred to the glass to expose an atomically flat gold surface. 50 μ L of the hybridized nucleic acid solution is deposited on the gold surface and the terminal linkers on the nucleic acid duplexes are allowed to bond to the gold surface for approximately 10 seconds. The gold substrates are then washed once with water and washed once with ethanol before complete drying under a stream of argon. Prolonged incubation of the substrate with the nucleic acid solution was shown to increase the coverage of the deposited duplexes and more commonly result in current-distance trajectories that included multiple molecules in the junction.

B.2.4 Conductance Measurements

All experiments were performed using freshly cut gold tips (0.25 mm, 99.95%, Alfa Aesar). The substrates were immersed in a mesitylene solution and the sample chamber was under an argon atmosphere. A typical set of measurements for a duplex involved the use of several tips and substrates. The biases utilized for the conductance measurements are shown in the following table. The current-distance characteristics were monitored between 0.09 nA and 100 nA. Currents below 0.09 nA were attributed to the solvent capacitance and not analyzed.

Table B.2. The applied bias for each measured duplex.

Duplex	Applied Bias (mV)
DNA/DNA (thiol)	50 ± 50
DNA/aeg-PNA (thiol)	50 ± 50
γ -PNA/ γ -PNA (thiol)	50 ± 50
aeg-PNA/aeg-PNA (thiol)	50 ± 50
DNA/DNA (amine)	50 ± 50
aeg-PNA/aeg-PNA (amine)	5 ± 5

B.2.5 Data Analysis

Data sets for each duplex included several thousand current-distance trajectories. The data sets were manually filtered to exclude trajectories that did not have molecular junctions or did not have an exponential decay with distance. The procedure for fitting the current-distance trajectories can be found in Ref. 5.

B.2.6 Thiol Location Control

To exclude any effect of the location of the thiol linker used in the conductance measurements, a control was performed in which the aeg-PNA/aeg-PNA duplex was measured with the thiol linker attached on both the C-end and N-end (see Table B1). Sample current-distance trajectories are shown in Figure B6.

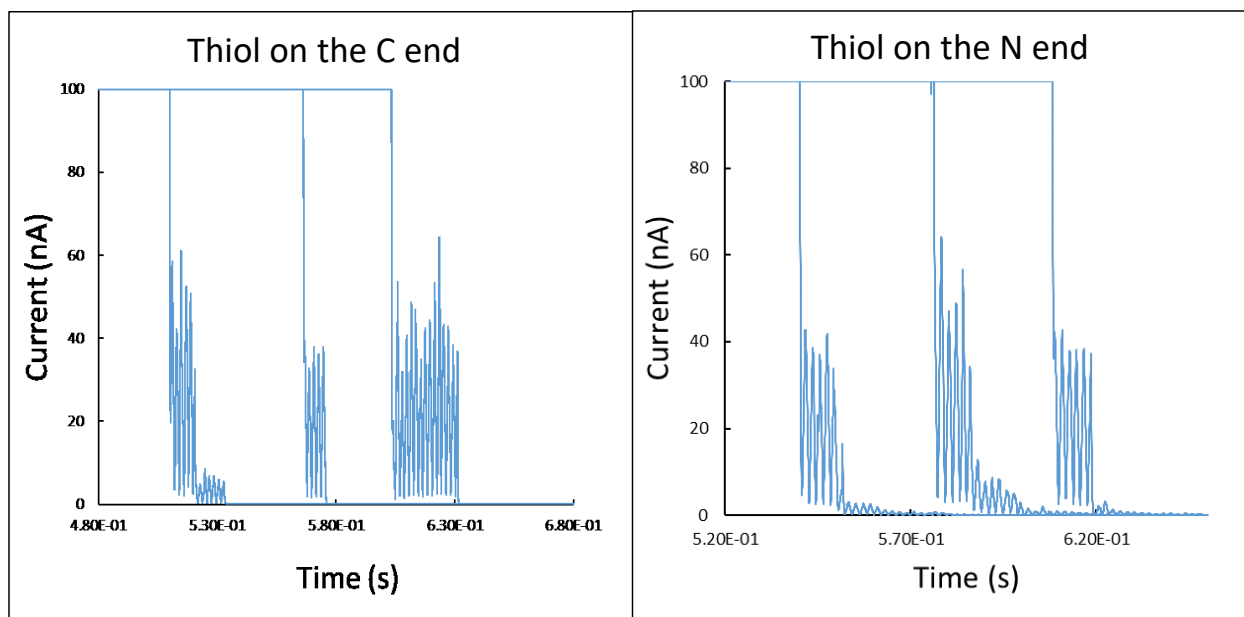


Figure B.6. Current-distance trajectories for aeg-PNA/aeg-PNA duplexes with thiol linkers on the C end and N terminus.

The results of the control showed equivalent current-distance characteristics for both duplexes. For this reason, differences observed between the aeg-PNA/aeg-PNA and γ -PNA/ γ -PNA can be attributed to the backbone composition and not the position of the thiol linker.

B.2.7 Mode Analysis

Analysis of the probability of the high conductance mode shows relative agreement among the studied duplexes (see Table B3). The absolute counts are totaled for each conductance mode based on the fitted Gaussian functions and the fraction of the counts corresponding to the high mode are given relative to the total counts. With the exception of the DNA/aeg-PNA duplex, the thiol linkers appear to have roughly an even probability of occupying the high mode and medium mode. For the amine linkers, the relative probability of the high mode appears to be lower.

Table B.3. The relative fraction of the high conductance mode calculated for the studied duplexes using the fitted Gaussian functions.

Duplex	High Mode Fraction
DNA/DNA (thiol)	0.47
DNA/aeg-PNA (thiol)	0.33
γ -PNA/ γ -PNA (thiol)	0.52
aeg-PNA/aeg-PNA (thiol)	0.53
DNA/DNA (amine)	0.31
aeg-PNA/aeg-PNA (amine)	0.39

B.2.8 Mode Fitting in aeg-PNA

The aeg-PNA conductance histogram displays three modes: high, medium, and low. However, for the purposes of comparison with the other studied duplexes, the analysis only focuses on the high and medium modes. Figure B7 shows a comparison of the aeg-PNA conductance histogram with both 2 and 3 fitted Gaussian functions. The calculated high and medium Gaussian functions shown in Figure B7B represent the same as those calculated for the fit to three Gaussians, but the fit to the low conductance mode is simply omitted.

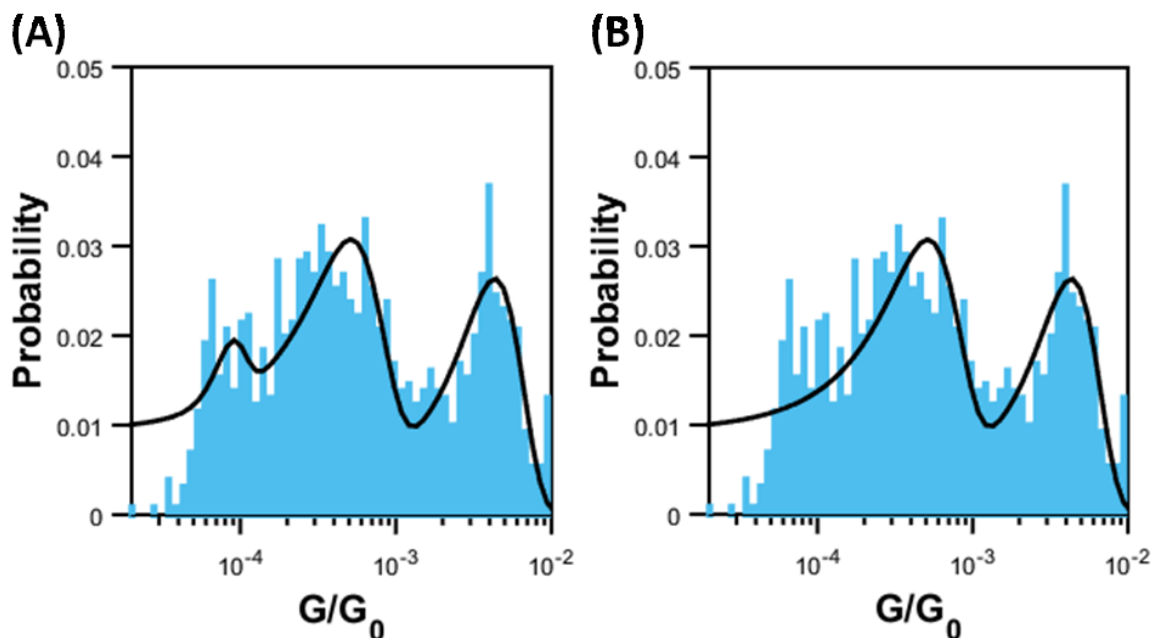


Figure B.7. The aeg-PNA conductance histograms with three Gaussian fits (A) and two Gaussian fits (B).

B.3 COMPUTATIONAL RESULTS

Computations were performed on the central part (six base pairs) of the nucleic acid duplex studied experimentally, see marked in blue in **Figure B.8**.

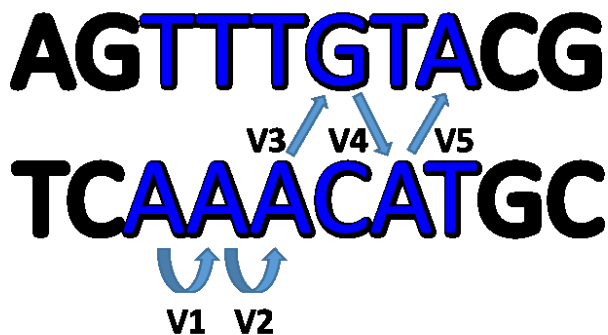


Figure B.8. Nucleic acid sequence and numbering scheme for the couplings between nearest neighbor purine bases.

B.3.1 The Electronic Coupling Strength Between Nearest Neighbor Purine Sites

The definitions of V1-V5 are shown in **Figure B.8**.

Table B.4: Root-mean-square of coupling strengths (in front of \pm) and found for the nucleic acid duplexes in eV.

	aeg-PNA	DNA	DNA/aeg-PNA	γ-PNA
V1	0.092 \pm 0.103	0.11 \pm 0.134	0.086 \pm 0.106	0.103 \pm 0.126
V2	0.087 \pm 0.104	0.11 \pm 0.136	0.089 \pm 0.112	0.0981 \pm 0.120
V3	0.055 \pm 0.055	0.034 \pm 0.040	0.037 \pm 0.053	0.0463 \pm 0.048
V4	0.013 \pm 0.022	0.016 \pm 0.021	0.012 \pm 0.019	0.0161 \pm 0.022
V5	0.072 \pm 0.073	0.043 \pm 0.051	0.066 \pm 0.070	0.0767 \pm 0.077

B.3.2 Simulation Results of Helical Parameter Thermal Fluctuations

Table B.5: Mean values and standard deviations of DNA helical parameters (from 10,000 MD snapshots).

DNA/DNA	T-A	T-A	T-A	G-C	T-A	A-T
Buckle (deg.)	2.08 \pm 9.83	-1.72 \pm 9.34	-6.05 \pm 10.28	-12.58 \pm 11.75	-2.35 \pm 11.28	0.44 \pm 10.89
Inclination (deg.)	6.59 \pm 11.29	6.8 \pm 8.38	8.22 \pm 8.59	19.61 \pm 11.65	8.04 \pm 10.37	6.18 \pm 10.34
Opening (deg.)	0.61 \pm 5.86	2.01 \pm 5.68	0.16 \pm 5.6	0.88 \pm 4.7	-0.3 \pm 6.02	-0.29 \pm 6.1
Rise (Å)	3.18 \pm 0.38	3.34 \pm 0.28	3.39 \pm 0.28	3.53 \pm 0.35	3.16 \pm 0.31	3.3 \pm 0.29
Roll (deg.)	3.26 \pm 6.06	4.28 \pm 5.41	5.04 \pm 5.32	11.79 \pm 6.83	3.86 \pm 5.05	3.94 \pm 6.87
Shear (Å)	0.03 \pm 0.28	0.08 \pm 0.27	0.1 \pm 0.28	-0.14 \pm 0.39	0.01 \pm 0.28	-0.01 \pm 0.28
Shift (Å)	-0.36 \pm 0.65	0.33 \pm 0.49	0.21 \pm 0.46	0.46 \pm 0.53	-0.57 \pm 0.59	-0.06 \pm 0.73
Slide (Å)	0.05 \pm 0.64	-0.06 \pm 0.46	-0.08 \pm 0.43	-0.06 \pm 0.6	-0.23 \pm 0.47	0.4 \pm 0.62
Stagger (Å)	-0.05 \pm 0.39	-0.33 \pm 0.38	-0.4 \pm 0.42	-0.11 \pm 0.43	0.09 \pm 0.39	0.11 \pm 0.38
Stretch (Å)	-0.06 \pm 0.12	-0.1 \pm 0.13	-0.12 \pm 0.13	0 \pm 0.17	-0.07 \pm 0.12	-0.07 \pm 0.12
Tilt (deg.)	-1.35 \pm 5.78	4.26 \pm 3.83	2.19 \pm 3.91	-0.86 \pm 4.98	-1.24 \pm 4.62	-0.1 \pm 4.82
Tip (deg.)	3.1 \pm 10.36	-6.5 \pm 5.87	-3.53 \pm 6.38	1.56 \pm 8.33	2.71 \pm 9.16	0.13 \pm 7.22
Twist (deg.)	32.36 \pm 5.95	37.22 \pm 4.09	35.63 \pm 4.15	33.77 \pm 5.32	29.96 \pm 5.37	38.85 \pm 4.14
X Disp. (deg.)	-0.59 \pm 1.71	-0.71 \pm 1.07	-0.9 \pm 1.08	-1.93 \pm 1.71	-1.29 \pm 1.45	0.01 \pm 1.46
Y Disp. (deg.)	0.38 \pm 1.25	0.04 \pm 0.88	-0.04 \pm 0.94	-0.87 \pm 1.1	0.8 \pm 1.37	0.08 \pm 1.14

Table B.6: Mean values and standard deviations of aeg-PNA helical parameters (from 10,000 MD snapshots).

aeg-PNA/aeg-PNA	T-A	T-A	T-A	G-C	T-A	A-T
Buckle (deg.)	-1.93 ± 9.09	0.79 ± 8.86	-0.18 ± 8.83	-3.07 ± 9.45	11.26 ± 8.9	4.96 ± 11.19
Inclination (deg.)	5.79 ± 15.47	1.94 ± 11.77	4.41 ± 10.46	16.79 ± 12.98	2.88 ± 11.32	28.79 ± 14.5
Opening (deg.)	-2.11 ± 7.56	-2.75 ± 7.09	-0.4 ± 6.48	-2.33 ± 4.14	1.86 ± 6.03	0.32 ± 5.81
Rise (Å)	3.35 ± 0.53	3.22 ± 0.31	3.31 ± 0.3	3.31 ± 0.36	3.09 ± 0.23	3.48 ± 0.38
Roll (deg.)	1.84 ± 5.3	0.7 ± 5.03	1.95 ± 4.83	7.26 ± 5.6	1.08 ± 4.39	10.23 ± 5.45
Shear (Å)	0 ± 0.3	0.01 ± 0.29	0.03 ± 0.28	0.04 ± 0.37	0.17 ± 0.29	0.01 ± 0.28
Shift (Å)	-0.34 ± 0.72	0.01 ± 0.49	0.09 ± 0.49	-0.07 ± 0.46	0.21 ± 0.6	-0.06 ± 0.45
Slide (Å)	-1.31 ± 0.77	-1.51 ± 0.51	-1.45 ± 0.47	-1.43 ± 0.43	-1.02 ± 0.53	-1.54 ± 0.52
Stagger (Å)	0.35 ± 0.49	0.15 ± 0.39	0 ± 0.4	0.57 ± 0.45	0.38 ± 0.42	-0.4 ± 0.47
Stretch (Å)	-0.08 ± 0.14	-0.05 ± 0.14	-0.05 ± 0.13	-0.11 ± 0.16	-0.09 ± 0.14	-0.1 ± 0.14
Tilt (deg.)	1.34 ± 5.31	1.8 ± 4.54	1.9 ± 4.29	-5.22 ± 5.13	0.36 ± 4.39	3.6 ± 5.48
Tip (deg.)	-3.17 ± 15.97	-3.99 ± 10.61	-4.1 ± 9.35	11.88 ± 11.79	-0.92 ± 11.12	-10.13 ± 15.8
Twist (deg.)	21.91 ± 7.37	25.2 ± 4.63	26.99 ± 4.53	23.58 ± 4.23	22.86 ± 4.38	17.36 ± 3.76
X Disp. (deg.)	-4.29 ± 4.21	-3.73 ± 2.52	-3.62 ± 2	-5.13 ± 2.11	-3.01 ± 2.65	-7.94 ± 2.84
Y Disp. (deg.)	1.36 ± 3.65	0.39 ± 1.54	0.26 ± 1.4	-1.17 ± 1.63	-0.34 ± 2.13	1.48 ± 2.5

Table B.7: Mean values and standard deviations of γ -PNA helical parameters (from 10,000 MD snapshots).

γ -PNA/ γ -PNA	T-A	T-A	T-A	G-C	T-A	A-T
Buckle (deg.)	-0.36 ± 8.8	0.25 ± 9.27	0.35 ± 9.06	-8.14 ± 9.82	2.01 ± 10.22	3.73 ± 9.86
Inclination (deg.)	3.01 ± 12.72	0.25 ± 10.92	2.26 ± 10.45	18.16 ± 12.52	4.96 ± 11.02	14.31 ± 14.43
Opening (deg.)	-1.44 ± 6.35	-0.77 ± 6.35	0.25 ± 6.46	-1.58 ± 4.18	0.93 ± 6.18	-0.05 ± 5.99
Rise (Å)	3.41 ± 0.3	3.32 ± 0.31	3.32 ± 0.31	3.48 ± 0.39	3.16 ± 0.25	3.21 ± 0.33
Roll (deg.)	0.93 ± 4.39	-0.04 ± 4.49	0.87 ± 4.43	7.3 ± 5.09	1.91 ± 4.35	5.09 ± 5.24
Shear (Å)	0.05 ± 0.29	0.06 ± 0.28	0.04 ± 0.28	-0.08 ± 0.37	0.13 ± 0.28	-0.04 ± 0.28
Shift (Å)	-0.17 ± 0.62	0.06 ± 0.47	0.05 ± 0.47	-0.06 ± 0.47	-0.19 ± 0.54	0.02 ± 0.51
Slide (Å)	-1.4 ± 0.75	-1.47 ± 0.45	-1.34 ± 0.46	-1.37 ± 0.44	-0.87 ± 0.53	-1.15 ± 0.48
Stagger (Å)	0.13 ± 0.47	0.06 ± 0.4	-0.09 ± 0.41	0.4 ± 0.45	0.38 ± 0.41	0.21 ± 0.44
Stretch (Å)	-0.09 ± 0.13	-0.06 ± 0.13	-0.05 ± 0.13	-0.09 ± 0.16	-0.1 ± 0.14	-0.08 ± 0.13
Tilt (deg.)	0.4 ± 4.19	1.02 ± 4.39	1.69 ± 4.43	-3.93 ± 5.14	0.06 ± 4.22	0.98 ± 4.95
Tip (deg.)	-0.76 ± 12.48	-2.31 ± 10.75	-3.96 ± 10.47	9.62 ± 12.67	-0.15 ± 10.63	-2.79 ± 13.72
Twist (deg.)	21.72 ± 5.73	23.76 ± 4.53	24.67 ± 4.39	21.75 ± 4.03	22.95 ± 4.32	19.81 ± 3.84
X Disp. (deg.)	-4.23 ± 3.8	-3.66 ± 2.37	-3.44 ± 2.14	-5.66 ± 2.24	-2.81 ± 2.1	-5.06 ± 2.61
Y Disp. (deg.)	0.57 ± 2.71	0.1 ± 1.73	0.35 ± 1.61	-1.08 ± 1.91	0.51 ± 1.91	0.36 ± 2.37

Table B.8: Mean values and standard deviations of aeg-PNA-DNA helical parameters (from 10,000 MD snapshots).

DNA/aeg-PNA	T-A	T-A	T-A	G-C	T-A	A-T
Buckle (deg.)	8.63 ± 9.45	10.06 ± 9.39	6.05 ± 9.96	-4.11 ± 9.94	10.75 ± 10.16	16.02 ± 11.13
Inclination (deg.)	7.16 ± 10.96	6.45 ± 10.15	8.17 ± 9.76	15.26 ± 11.66	8.25 ± 10.93	3.13 ± 13.91
Opening (deg.)	-1.44 ± 6.02	1.01 ± 6.21	1.81 ± 6.57	-0.77 ± 4	0.15 ± 5.89	2.14 ± 7.04
Rise (Å)	3.29 ± 0.29	3.32 ± 0.31	3.46 ± 0.33	3.5 ± 0.38	3.07 ± 0.25	3.2 ± 0.29
Roll (deg.)	3.38 ± 5.33	3.17 ± 5.15	4.21 ± 5.06	8.12 ± 6.1	3.38 ± 4.54	1.1 ± 7.06
Shear (Å)	0.09 ± 0.28	0.11 ± 0.28	0.1 ± 0.28	-0.13 ± 0.34	-0.01 ± 0.28	-0.05 ± 0.28
Shift (Å)	-0.96 ± 0.53	-0.33 ± 0.49	-0.46 ± 0.47	-0.93 ± 0.55	-0.96 ± 0.48	-1.01 ± 0.67
Slide (Å)	-0.94 ± 0.49	-1.01 ± 0.41	-1.11 ± 0.45	-1.16 ± 0.41	-0.61 ± 0.38	0.17 ± 0.65
Stagger (Å)	-0.03 ± 0.43	-0.23 ± 0.43	-0.24 ± 0.45	0.4 ± 0.39	0.29 ± 0.38	0.09 ± 0.42
Stretch (Å)	-0.08 ± 0.13	-0.04 ± 0.14	-0.05 ± 0.14	-0.08 ± 0.15	-0.07 ± 0.13	-0.06 ± 0.14
Tilt (deg.)	0.56 ± 4.16	0.11 ± 4.43	-0.94 ± 4.43	-7.57 ± 5.27	-0.02 ± 4.14	1.03 ± 5.08
Tip (deg.)	-1.31 ± 8.66	-0.36 ± 8.76	1.72 ± 8.54	13.57 ± 9.18	-0.25 ± 9.88	-2.4 ± 10.02
Twist (deg.)	27.87 ± 4.34	29.26 ± 4.13	29.93 ± 4.01	29.86 ± 4.77	24.3 ± 4.37	29.78 ± 5.12
X Disp. (deg.)	-2.69 ± 1.73	-2.69 ± 1.53	-2.99 ± 1.51	-3.65 ± 1.58	-2.38 ± 1.64	-0.19 ± 2.29
Y Disp. (deg.)	2.11 ± 1.52	0.65 ± 1.38	0.63 ± 1.29	0.26 ± 1.33	2.25 ± 1.74	2.12 ± 1.5

B.3.3 Linker Study

We examined the effect of the linker group on the overall conductance by examining the average contact distance between the heteroatom of the linker (the thymidine N atom and the thiol S atom) that is believed to bind to the Au and the nearest guanine base; see Figure 3.2. Molecular dynamics (MD) simulations were run and the distribution of through space distances for the atom linked to Au (S in thiol linker and N in amino linker) and the center of the closest guanine base were calculated and are presented in Figure B9. The center of the closest guanine base was defined as the geometric center of the heavy atoms (C, N and O) on the guanine ring. Because the electronic coupling is known to change exponentially with distance through saturated bonds and the saturated groups are similar for the two linkers, the through space distance calculated here is presumed to reflect the difference in coupling strengths qualitatively. A more rigorous treatment would evaluate the through space and through bond contributions explicitly, however it is not clear that the data warrant such a treatment, as the junction geometry is likely to change from measurement to measurement.

The distance distributions shown in Figure B9 reveal significant differences among the three different duplexes: the DNA homoduplex, aeg-PNA homoduplex, and γ -PNA homoduplex. The aeg-PNA and γ -PNA display a multi-mode distance distribution between the S atom and the center of the guanine, whereas the DNA duplex shows one dominant mode. For the PNA duplexes, the distributions display a short distance mode at around 4 Å and another somewhat longer one at ~about 8 Å. In addition, the PNAs have significant population in the distance range from 9 to 13 angstroms, which encompasses the unimodal distance distribution peaking at ~11 Å for the DNA. In general, the PNA duplexes have significant population in which the G base is closer to the metal (thiol as surrogate).

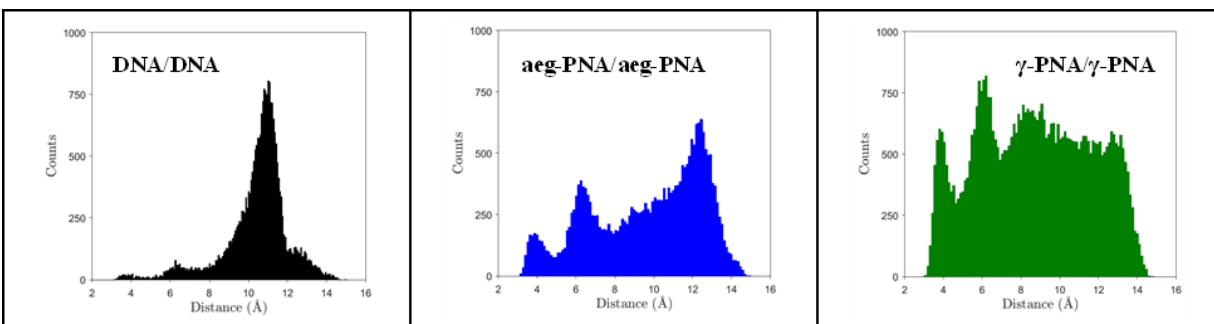


Figure B.9. The contact distance distributions for DNA/DNA (left), aeg-PNA/aeg-PNA (middle) and γ -PNA/ γ -PNA (right).

The PNA and γ -PNA can access a van der Waals contact regime (~4 Å) and a typical snapshot showing this interaction is shown in Figure B10. We recorded the time evolution of the contact distance and found that the lifetime of each mode is on the time scale of several nanoseconds.

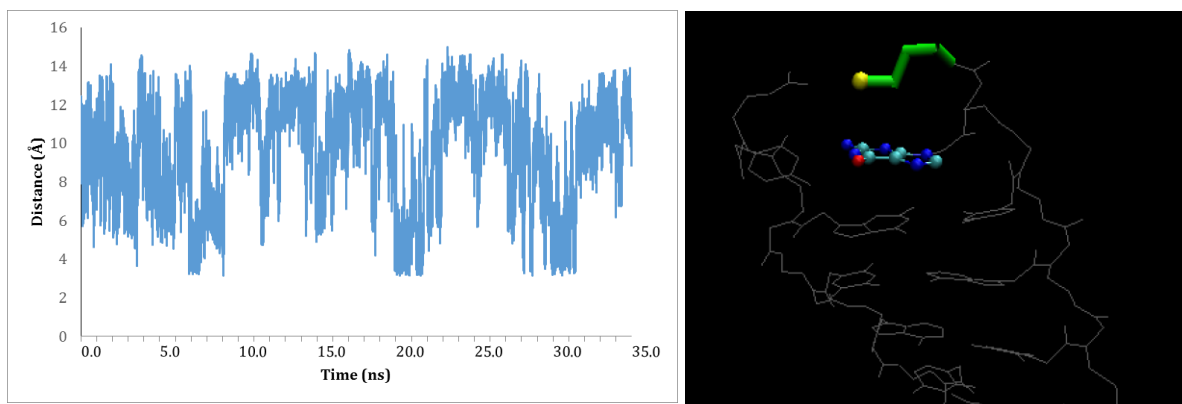


Figure B.10. Time evolution of the contact distance (left); A typical snapshot of the vDW contact between the S atom (colored in yellow) on the thiol linker (green) and the guanine (colored as atom type) (right).

For the amine linked PNA and DNA duplexes the molecular dynamics simulations gave a unimodal distribution for the contact distance (Figure B11) with average contact distances of $9.2 \text{ \AA} \pm 1.4 \text{ \AA}$ for DNA and $9.0 \text{ \AA} \pm 1.2 \text{ \AA}$ for PNA. Both are shorter than the average contact distance in the thiol modified structures. Note also that the effective injection coupling between the STM tip and the guanine for the amine modified structures is mediated by a thymine base, which should enhance the effective coupling as compared to the thiol modified structures.

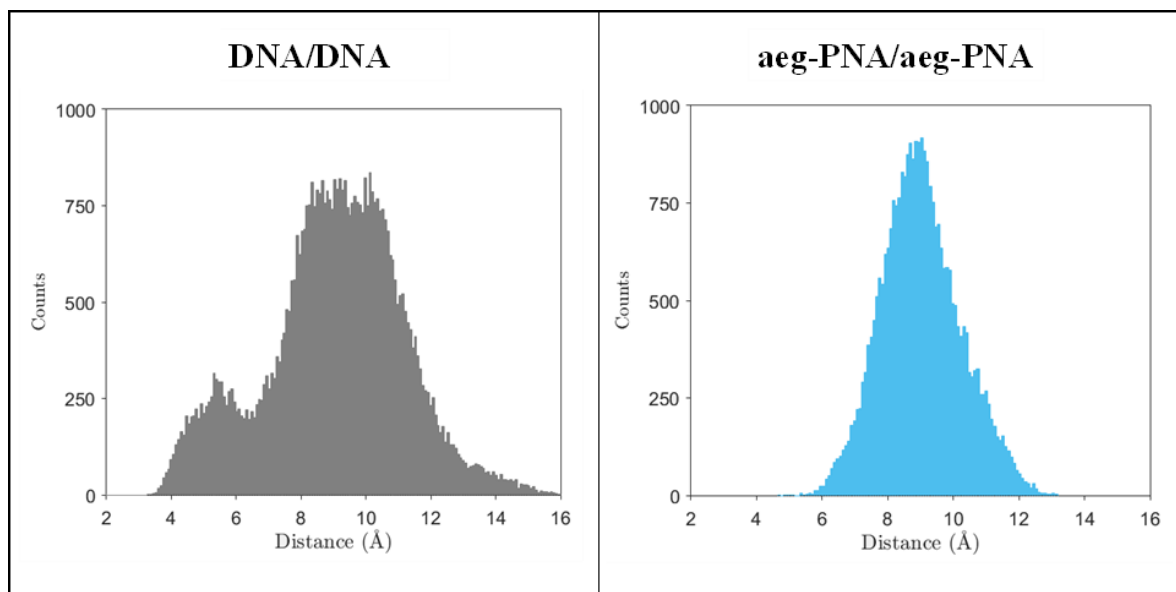


Figure B.11. Contact distance distributions for amine modified DNA (top) and PNA (bottom).

These findings suggest that the amino linker structures have a stronger effective injection coupling with the Au because of their closer average proximity to the electrode; however, the thiol modified PNA and γ -PNA can access conformations that place the G base in van der Waals contact with the Au tip.

Table B.9. Summary of the contact distance calculations for the measured duplexes.

System	Average contact distance	Distribution mode	Coupling type	Number of snapshots
Thiol modified DNA	10.4 Å ± 1.7 Å	Unimodal	Through space	25,000
Thiol modified PNA	9.6 Å ± 2.8 Å	Multiple peaks	Through space	35,000
Thiol modified γ -PNA	8.7 Å ± 2.9 Å	Multiple peaks	Through space	49,000
Amine modified DNA	9.2 Å ± 1.4 Å	Unimodal	Base mediated	52,000
Amine modified PNA	9.0 Å ± 1.2 Å	Unimodal	Base mediated	30,000

B.4 REFERENCES

1. Qvit, N.; Reuveni, H.; Gazal, S.; Zundeleovich, A.; Blum, G.; Niv, M. Y.; Feldstein, A.; Meushar, S.; Shalev, D. E.; Friedler, A.; Gilon, C.. *J. Comb. Chem.* **2008**, *10* (2), 256-66.
2. Mourtas, S.; Katakalous, C.; Nicolettou, A.; Tzavara, C.; Gatos, D.; Barlos, K. *Tetrahedron Lett.* **2003**, *44* (1), 179-182.
3. Oquare, B. Y.; Taylor, J. S. *Bioconjug. Chem.* **2008**, *19* (11), 2196-204.
4. Hegner, M.; Wagner, P.; Semenza, G. *Surf. Sci.* **1993**, *291* (1-2), 39-46.
5. Beall, E.; Yin, X.; Waldeck, D. H.; Wierzbinski, E. *Nanoscale* **2015**, *7* (36), 14965-14973.

APPENDIX C:
SUPPORTING INFORMATION FOR CHAPTER 4

C.1 NUCLEIC ACID SEQUENCES

The sequences for the nucleic acid oligomers which were studied are listed in Table C.1. Note that a (CH₂)₃SH linker group was used for the strands involved in the conductance measurements to bind the duplexes to the electrodes. The strands used for the fluorescence measurements have pyrene modifications (indicated by “*pyr*”) and these oligomers do not have thiol modifications.

Table C.1. Sequence of oligonucleotides^a

PNA Sequences	
P1	H-CGTACAAACTTAGACACCAG Lys ₃ -(CH ₂) ₃ SH
P2	H-CTGGTGTCTAAGTTTGTACG Lys ₃ -(CH ₂) ₃ SH
P2a	H-AGTTTGTACG Lys-(CH ₂) ₃ SH
P2a(p)	H-AGTTTGTACG Lys(<i>pyr</i>)Lys-NH ₂
PT-PNA	Ac-AGTTTGTACG-(CH ₂) ₃ SH
P2b	H-Lys-CTGGTGTCTA-NH ₂
P2b(p)	H-Lys Lys(<i>pyr</i>)CTGGTGTCTA-NH ₂
DNA Sequences	
D1	CGTACAAACTTAGACACCAG-(CH ₂) ₃ SH
D2	CTGGTGTCTAAGTTTGTACG-(CH ₂) ₃ SH
D1(2p)	(<i>pyr</i>)CGTACAAACTTAGACACCAG(<i>pyr</i>)
D2a	AGTTTGTACG-(CH ₂) ₃ SH
D2a(p)	AGTTTGTACG(<i>pyr</i>)
D2b	CTGGTGTCTA
D2b(p)	(<i>pyr</i>)CTGGTGTCTA

(p) = one terminal pyrene; (2p) = two terminal pyrenes; PT = propylthiol

C.2 MATERIALS AND METHODS

C.2.1 Synthesis of PNA Oligomers

The PNA oligomers were synthesized on 10% *L*-lysine-downloaded MBHA resin (0.45 meq. NH₂/g, Peptides International). The oligomers were cleaved from the resin using a mixture containing *m*-cresol/thioanisole/TFA/TFMSA (150/150/900/300 μL per 100 mg of resin). The crude mixture was eluted and precipitated with diethyl ether, dissolved in water, and purified by reversed-phase HPLC using a C18 silica column. All oligomers were characterized by MALDI-ToF mass spectrometry (Table S2. Oligomer Sequences and MALDI MS Data) on an Applied Biosystems Voyager Biospectrometry Workstation using α-cyano-4-hydroxycinnamic acid matrix (10 mg/mL in 1:1 water/acetonitrile, 0.1% TFA).

C.2.2 Attachment of Pyrene to the C-End Of PNA

Pyrene can be used as a fluorescent marker that makes it possible to measure the distances between, or within biomolecules. Pyrene can be inserted in PNA oligomers either as part of a PNA monomer, or as a side chain of an amino acid.¹⁻² In this study, pyrene was coupled to the side chain of a C- or N-terminal lysine.

Attachment of the pyrene moiety to the C-end of PNA was carried out using a combined Fmoc/Boc strategy. First, the MBHA resin was downloaded with Boc-Lys(2-Cl-Z)-OH, followed by the removal of the Boc group (95% TFA: 5% *m*-cresol) and the addition of Fmoc-Lys(Boc)-OH. Then, the Boc protection of the side-chain was removed (95% TFA: 5% *m*-cresol) and 1-pyreneacetic acid was coupled to the free NH₂ group in the presence of HBTU and DIPEA. After capping with 5% acetic anhydride and 6% lutidine in DMF, the Fmoc group from the N-terminus of lysine was removed using 20% piperidine in DMF; the solid-phase synthesis was continued applying the Boc protection strategy.

C.2.3 Attachment of Pyrene to the N-end of PNA

Fmoc-Lys(Boc)-OH was added to the growing oligomer after the last PNA monomer. The Boc group of this terminal lysine was removed using a mixture of 95% TFA : 5% *m*-cresol, followed by the HBTU/DIPEA activated coupling of 1-pyreneacetic acid. Then, the Fmoc group was removed with 20% piperidine in DMF, and the cleavage of the PNA oligomer was carried out using the mixture consisting of *m*-cresol/thioanisole/TFA/TFMSA (150/150/900/300 μ L per 100 mg of resin).

Table C.2. Oligomer Sequences and MALDI MS Data

Oligomer	Oligomer sequence N to C	Calc.	Obs.
P1	H-CGTACAAACTTAGACACCAG Lys ₃ -(CH ₂) ₃ SH	5783.55	5782.34
P2	H-CTGGTGTCTAAGTTTGTACG Lys ₃ -(CH ₂) ₃ SH	5858.83	5859.84
P2a	H-AGTTTGTACG Lys-(CH ₂) ₃ SH	2885.85	2886.86
P2a(p)	H-AGTTTGTACG Lys(<i>pyr</i>)Lys-NH ₂	3257.03	3257.15
PT-PNA	Ac-AGTTTGTACG-(CH ₂) ₃ SH	2874.67	2875.25
P2b	H-Lys-CTGGTGTCTA-NH ₂	2861.83	2861.13
P2b(p)	H-Lys Lys(<i>pyr</i>) CTGGTGTCTA-NH ₂	3233.29	3233.14

C.2.4 Thermal Stability

UV melting curves were recorded in the temperature range 5°C to 95°C. The rate of both cooling and heating was 1°C/min. Prior to the measurement of the melting profiles, the solutions were kept at 95°C for 20 min. The melting temperature T_m was taken at the inflection point of the Boltzmann sigmoidal fit function, which assumes a two-state model.

Table C.3. Summary of Thermal Stabilities for DNA/DNA and PNA/PNA Homo-duplexes(T_m [°C]), and DNA/PNA Hetero-duplexes(T_m [°C])

Homo-DNA duplex	T_m [°C]	Homo-PNA/PNA Duplex	T_m [°C]	Hetero- DNA/PNA Duplex	T_m [°C]
D1(2p)D2a(p)D2b(p)	30	P1P2	>90	P1P2aD2b	68
D1(2p)D2a(p)	25			D1(2p)P2a(p)P2b(p)	66
D1(2p)D2b(p)	31			D1(2p)P2a(gRH)P2b(p)	73
				D1(2p)P2a(p)	65
				D1(2p)P2b(p)	66

T_m are known within 2 °C. T_m were obtained from the curve-fitting data or estimated from the first derivative of the melting curves. The T_m values are an average of at least two experiments.

Figure C.1 shows melting curves for the full and nicked versions of the DNA/DNA and DNA/PNA duplexes. The effect of the nick is demonstrated by a shift in the melting temperature to smaller values for the nicked versions of the duplexes.

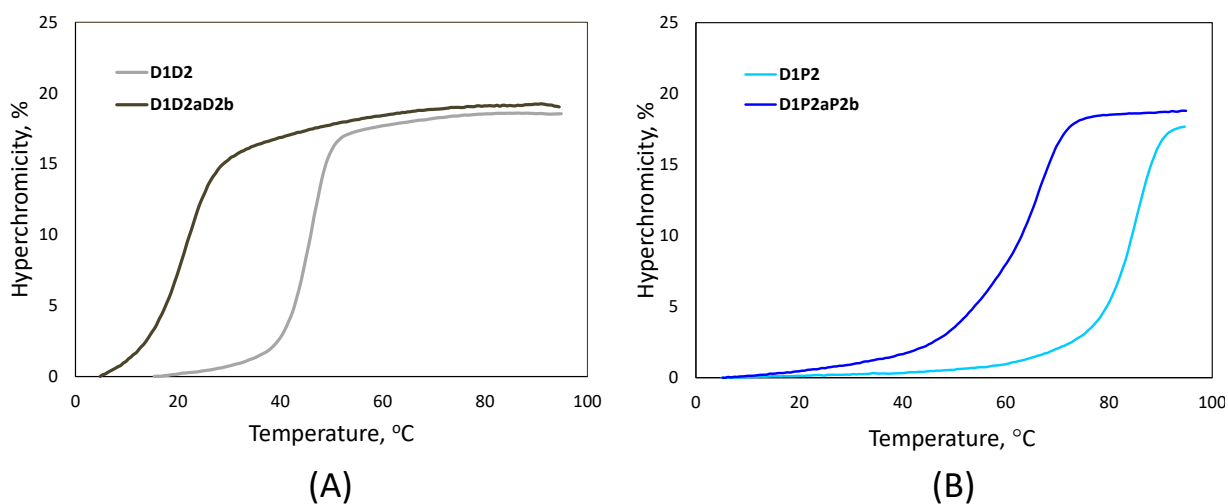


Figure C.1. (A) The melting curves for the full DNA and nicked DNA. (B) The melting curves for the full DNA/PNA and nicked DNA/PNA.

C.2.5 Chirality of the Nicked Homo- and Heteroduplexes

The handedness of the nicked PNA/PNA:DNA and DNA duplexes was determined by circular dichroism (CD) spectroscopy. Figure S2 shows the CD spectra for both duplexes. While

the spectra show exciton coupling patterns consistent with literature findings for DNA and DNA/PNA duplexes,⁵ the CD responses are markedly different for the nicked nucleic acid duplexes. The spectrum for the PNA/PNA:DNA heteroduplex has an additional point of inflection compared to the spectrum for the nicked DNA duplex, resulting in an additional negative peak in the spectrum at ~ 290 nm.

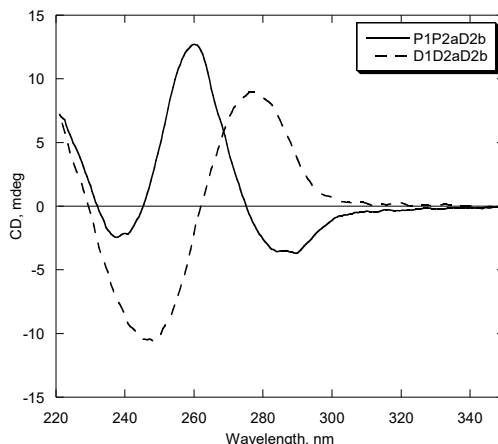


Figure C.2. CD spectra of nicked PNA/PNA:DNA and DNA duplexes. Samples containing stoichiometric amounts of oligonucleotides at 3 μ M strand concentration were prepared in 10 mM sodium phosphate buffer.

C.2.6 Fluorescence Studies

Excitation and emission spectra were obtained using a Cary Eclipse fluorimeter. Emission spectra were recorded with 0.2 ms delay time and 5 ms gate time in the range 350-600 nm with selective irradiation at 345 nm ($\lambda_{\text{ex}} = 345$ nm).

C.2.7 Conductance Measurements

C.2.7.1 Equipment

All conductance measurements were performed using an Agilent 5500 Scanning Probe Microscope system with a Stanford Research Systems DS345 function generator. Experiments were performed in an environmental chamber housed in an acoustically isolated Faraday cage. The

Faraday cage was mounted on an anti-vibrational table (Table Stable). The current was collected using a 10 nA/V preamplifier.

C.2.7.2 Nucleic Acid Duplexes

DNA oligomers were purchased from Integrated DNA Technologies and the PNA strands were synthesized following procedures detailed above. Hybridization of the strands was achieved by heating solutions containing 20 μ M of each nucleic acid strand in pH=7.0 Tris-EDTA buffer to 95 °C for 10 minutes and allowing them to cool to room temperature over several hours. The characterization of the nicked duplexes was performed as detailed above.

C.2.7.3 Substrate Fabrication

The gold substrates were fabricated using the template-stripping technique.⁶ A 100 nm Au film was evaporated onto freshly-cleaved mica sheets using an AJA ATC-T Series Thermal Evaporation System. Glass slips (10 mm x 25 mm) were cleaned in a piranha solution and affixed to the gold surface using an epoxy resin (Epo-Tek). Prior to each experiment, a glass slip was peeled from the mica sheet; and the gold film was transferred to the glass slip.

C.2.7.4 Substrate Preparation

50 μ L of the hybridized nucleic acid solution was deposited on the gold surface for 10 seconds to allow for a diffuse monolayer to form via the thiol linkers. The substrates were then washed with water, washed with ethanol, and dried under a stream of inert gas.

C.2.7.5 Conductance Measurements

All conductance measurements were performed using freshly cut gold wire (0.25 mm, 99.95%, Alfa Aesar). The prepared substrates were immersed in a mesitylene solution in an inert atmosphere. The current-distance characteristics were monitored between 0.09 nA and 100 nA with current below 0.09 nA attributed to the solvent and removed.

C.2.7.6 Data Analysis

Thousands of current-distance trajectories were collected for each duplex. Data sets were manually filtered to remove trajectories without molecular junctions. The procedure for fitting the trajectories is detailed in Ref. 7.⁷ The resulting conductance histograms were fit using Gaussian functions, as shown in Figure C.3.

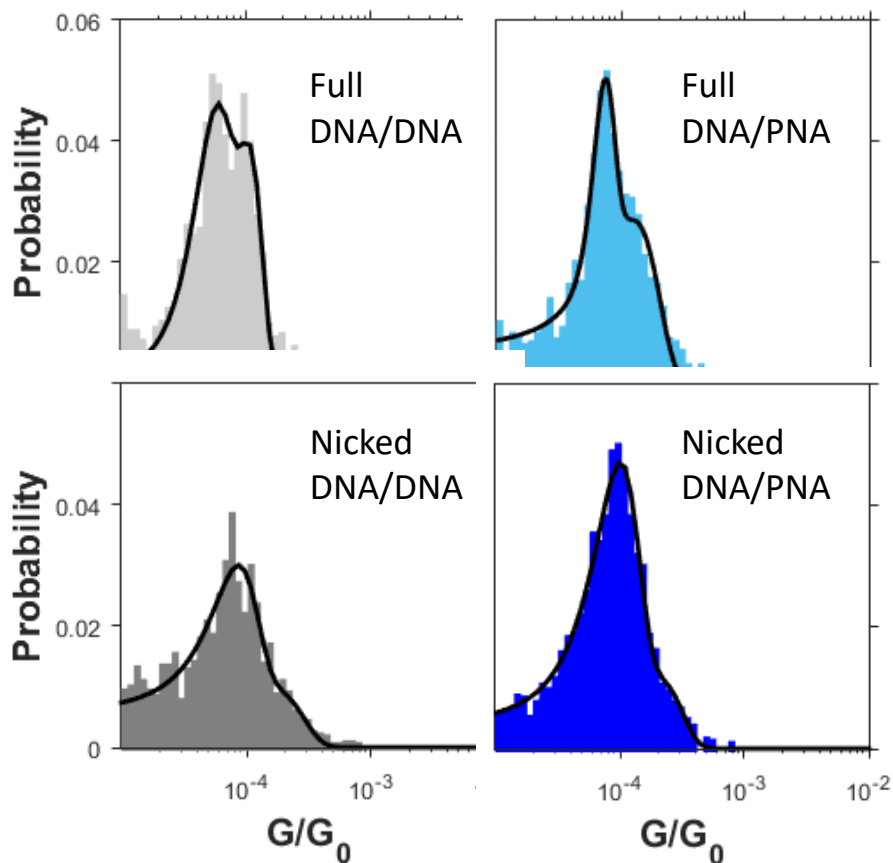


Figure C.3. The conductance histograms for the full and nicked versions of the DNA/DNA and DNA/PNA duplexes. The Gaussian fits are shown as overlaid black curves.

C.2.8 Thiol Location Control

To exclude any effect of the thiol location on a backbone in the nicked PNA/PNA:DNA heteroduplex, a control was performed in which the nicked PNA/PNA:DNA heteroduplex was measured with the thiol linker on the DNA 10-mer rather than on the PNA 10-mer. In these

duplexes, the base stack remains composed of the same strands; however, the identity of the strand with the second thiol linker is DNA in one case and PNA in the other. Conductance histograms are shown in Figure C.4 for both nicked heteroduplexes.

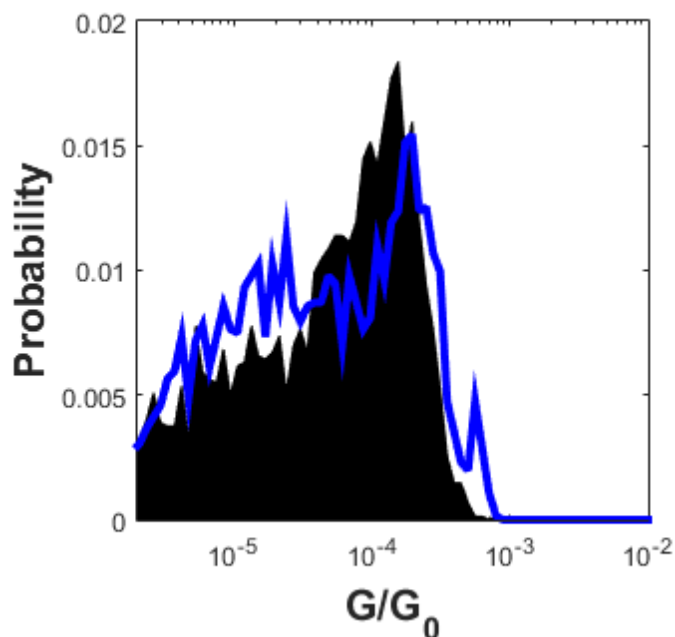


Figure C.4. Conductance histograms for the nicked PNA/PNA:DNA heteroduplex with the thiol linker on the DNA 10-mer (black), and with the thiol linker on the PNA 10-mer (blue).

The results of this control experiment showed equivalent high-mode conductances for both duplexes. This suggests that the location of the thiol, whether on a DNA strand or a PNA strand, does not affect the molecular conductance. This supports the conclusion that charge moves through the base stack, as the base stack composition is the same for both duplexes.⁸

C.2.9 Serial Correlation

In an attempt to distinguish the behavior of the molecular junctions for each duplex, serial correlation analyses were employed for the conductance measurements.⁹ The serial correlation is defined as:

$$r_k = \frac{\frac{1}{N-1} \sum_{n=1}^{N-k} (G_n - \bar{G})(G_{n+k} - \bar{G})}{c_0} \quad \text{Equation C.1}$$

where n and k index periods in the trajectory, G is the conductance for a given period, \bar{G} is the average conductance, and c_0 is the variance of the conductance of the trajectory.

Correlation analyses utilizing the STM-BJ technique display a rapid decay as the movement of the STM tip drives an eventual breakdown of the junction.¹⁰⁻¹² The calculated serial correlation values are indistinguishable between the duplexes because of the rapid loss of correlation. This behavior is attributed to the multiple conductance modes that are probed in the frozen junction technique.¹³⁻¹⁴ Therefore, a statistical analysis of the conductance value fitted for each current response period was performed to compare the full duplexes to their nicked analogues for stabilized molecular junctions.¹⁵ Utilizing custom Matlab scripts, periods of the current response that have a current greater than the solvent threshold are assumed to arise from molecular junctions and are separated from the full current-time, $I(t)$, trajectory (see Figure C.5). The set of periods containing molecular junctions was concatenated for correlation analysis.

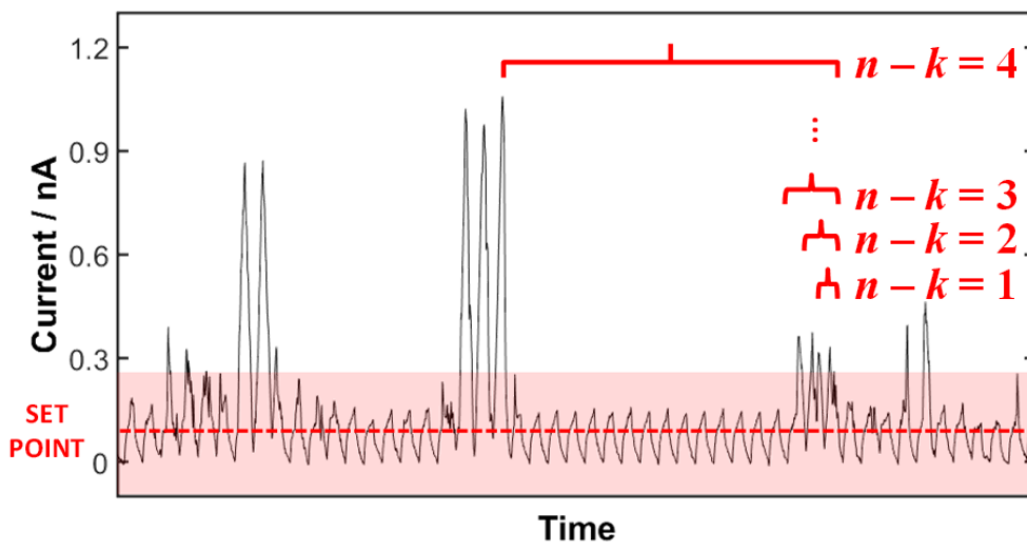


Figure C.5. A current-time, $I(t)$, trajectory showing the method of solvent removal and period concatenation. The set-point of the conductance measurements is shown as a red, dashed line. The red, shaded region depicts the periods of the current response that are within the solvent threshold and are filtered out of the correlation analysis.

The serial correlation (the correlation of the conductance in the n^{th} period of a trajectory with that in the $(n - k)^{\text{th}}$ period) is calculated for the full and nicked duplexes and shown in Figure S6 for the frozen junction technique. Despite creating stabilized molecular junctions, serial correlation analyses did not show distinguishable decay characteristics between the set of duplexes. Correlation analyses were subsequently directed to the initial periods of the STM-BJ measurements to ensure a comparison within a similar range of current values (see Figure 4.5).

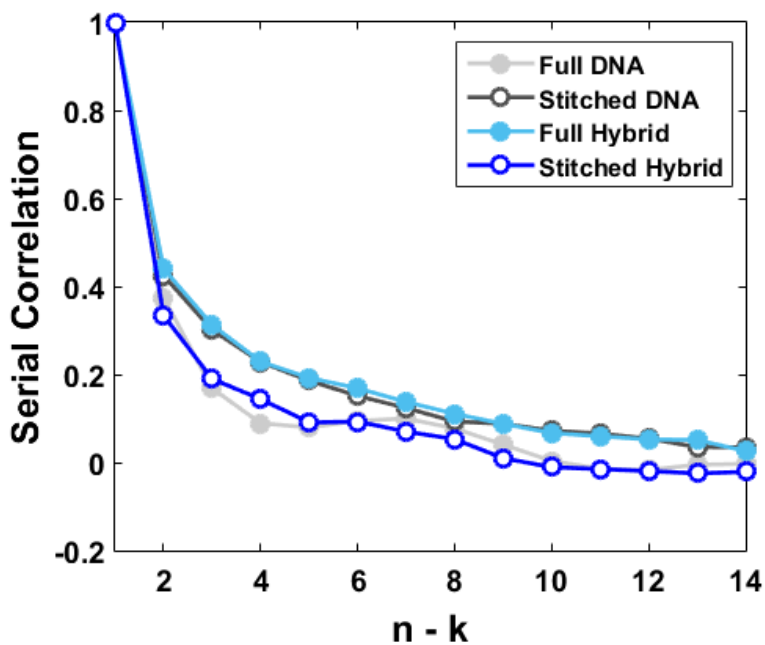


Figure C.6. Serial correlation is shown for the full and nicked versions of the DNA and DNA/PNA duplexes using the ‘frozen junction’ method.

C.3 DNA CONDUCTANCE COMPARISON

The conductance data presented in Figure C.7 are shown versus the total number of base pairs. Inclusion of the G/C base pairs in the length count eliminates the exponential dependence demonstrated in Figure 4.7, in which only the number of A/T pairs are used as a metric for the tunneling length.

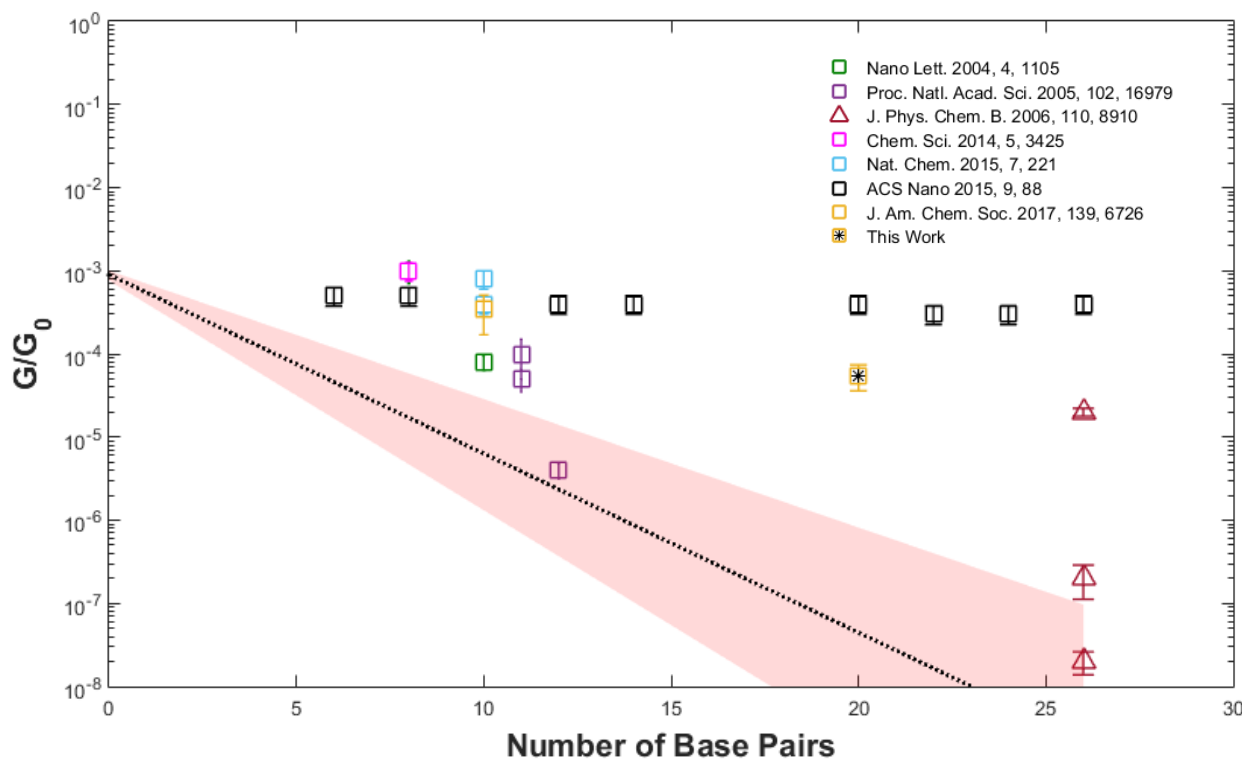


Figure C.7. Conductance values for DNA duplexes as a function of the total number of base pairs of the duplex measured by various methods. In the conductance measurements, the DNA was attached to the surface by three-carbon (C3) thiol linkers. Squares identify the conductance measured by the scanning tunneling microscope break junction method. Triangles identify values measured by atomic force microscopy conductance utilizing a gold nanoparticle. The dashed line indicates the best fit function shown in Figure 7; and the shaded region shows a 95% confidence interval for the best fit.

C.4 REFERENCES

1. Manicardi, A. G., L.; Ghidini, A.; Corradini, R., Pyrene-modified PNAs: Stacking interactions and selective excimer emission in PNA₂DNA triplexes. *Beilstein J. Org. Chem.* **2014**, *10*, 1495-1503.
2. Sacui, I.; Hsieh, W.-C.; Manna, A.; Sahu, B.; Ly, D. H., Gamma Peptide Nucleic Acids: As Orthogonal Nucleic Acid Recognition Codes for Organizing Molecular Self-Assembly. *J. Am. Chem. Soc.* **2015**, *137*, 8603-8610.
3. Beall, E.; Ulku, S.; Liu, C.; Wierzbinski, E.; Zhang, Y.; Bae, Y.; Zhang, P.; Achim, C.; Beratan, D. N.; Waldeck, D. H., Effects of the Backbone and Chemical Linker on the Molecular Conductance of Nucleic Acid Duplexes. *J. Am. Chem. Soc.* **2017**, *139*, 6726-6735.
4. Yeh, J. I.; Shivachev, B.; Rapireddy, S.; Crawford, M. J.; Gil, R. R.; Du, S.; Madrid, M.; Ly, D. H., Crystal Structure of Chiral γ PNA with Complementary DNA Strand: Insights into the Stability and Specificity of Recognition and Conformational Preorganization. *J. Am. Chem. Soc.* **2010**, *132*, 10717-10727.

5. *Comprehensive Chiroptical Spectroscopy: Applications in Stereochemical Analysis of Synthetic Compounds, Natural Products, and Biomolecules*; Berova, N.; Polavarapu, P. L.; Nakanishi, K.; Woody, R.W., Eds.; John Wiley & Sons: Hoboken, NJ, 2012.
6. Hegner, M.; Wagner, P.; Semenza, G., Ultralarge Atomically Flat Template-Stripped Au Surfaces for Scanning Probe Microscopy. *Surf. Sci.* **1993**, *291*, 39-46.
7. Beall, E.; Yin, X.; Waldeck, D. H.; Wierzbinski, E., A scanning tunneling microscope break junction method with continuous bias modulation. *Nanoscale* **2015**, *7*, 14965-14973.
8. Liu, T.; Barton, J. K., DNA Electrochemistry through the Base Pairs Not the Sugar-Phosphate Backbone. *J. Am. Chem. Soc.* **2005**, *127*, 10160-10161.
9. Dunn, P. F., *Measurement and Data Analysis for Engineering and Science*; McGraw-Hill: New York, 2005.
10. Park, Y. S.; Whalley, A. C.; Kamenetska, M.; Steigerwald, M. L.; Hybertsen, M. S.; Nuckolls, C.; Venkataraman, L., Contact Chemistry and Single-Molecule Conductance: A Comparison of Phosphines, Methyl Sulfides, and Amines. *J. Am. Chem. Soc.* **2007**, *129*, 15768-15769.
11. Zhou, J.; Chen, F.; Xu, B., Fabrication and Electronic Characterization of Single Molecular Junction Devices: A Comprehensive Approach. *J. Am. Chem. Soc.* **2009**, *131*, 10439-10446.
12. Bruot, C.; Xiang, L.; Palma, J. L.; Tao, N., Effect of Mechanical Stretching on DNA Conductance. *ACS Nano* **2015**, *9*, 88-94.
13. Li, C.; Pobelov, I.; Wandlowski, T.; Bagrets, A.; Arnold, A.; Evers, F., Charge Transport in Single Au | Alkanedithiol | Au Junctions: Coordination Geometries and Conformational Degrees of Freedom. *J. Am. Chem. Soc.* **2008**, *130*, 318-326.
14. Haiss, W.; Martín, S.; Leary, E.; Zalinge, H. v.; Higgins, S. J.; Bouffier, L.; Nichols, R. J., Impact of Junction Formation Method and Surface Roughness on Single Molecule Conductance. *J. Phys. Chem. C* **2009**, *113*, 5823-5833.
15. Zhou, J.; Chen, G.; Xu, B., Probing the Molecule-Electrode Interface of Single-Molecule Junctions by Controllable Mechanical Modulations. *J. Phys. Chem. C* **2010**, *114*, 8587-8592.

APPENDIX D:
SUPPORTING INFORMATION FOR CHAPTER 5

D.1 BACKGROUND CONTROL EXPERIMENTS

To ensure that the histograms created for the PNA duplexes can be attributed to PNA molecular junctions, conductance measurements were performed with the exclusion of the PNA incubation step. All other procedural steps were followed as described. The number of experiments performed for the control study was equivalent to the number performed for the PNA duplexes. The results of the control study are shown in Figure D.1. The number of modulation periods observed for experiments excluding the PNA duplexes is considerably less than those for the duplexes shown in Figure 5.2.

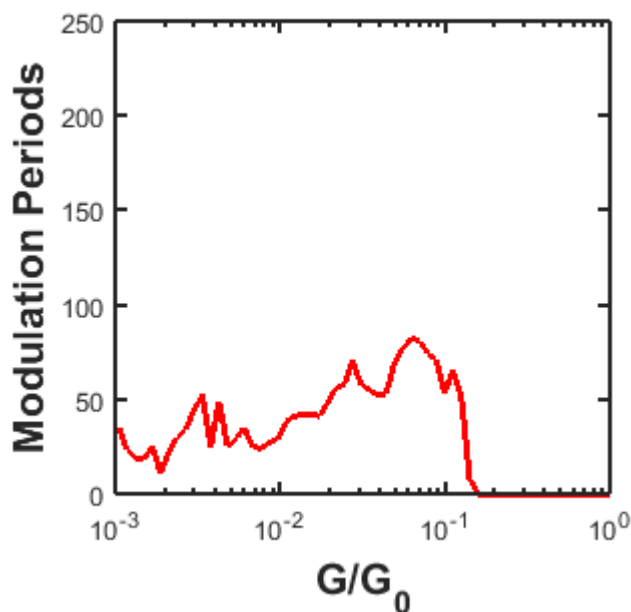


Figure D.1. The results of the control study are shown for the number of experiments performed using PNA duplexes. The number of modulation periods is considerably less than those for each PNA duplex.

In an attempt to determine the origin of the current responses observed in the control study, a substrate was electrochemically oxidized (1.5 V, 60 s) and measured alongside a substrate that did not undergo electrochemical oxidation. A comparison is shown in Figure D.2. The unmodified surface shows significantly fewer modulated periods than the oxidized surface. While the origin of the modulation periods observed in the control study cannot be concluded to arise from gold oxidation, oxidizing the gold substrate surface results in many more current responses with supposed molecular junctions.

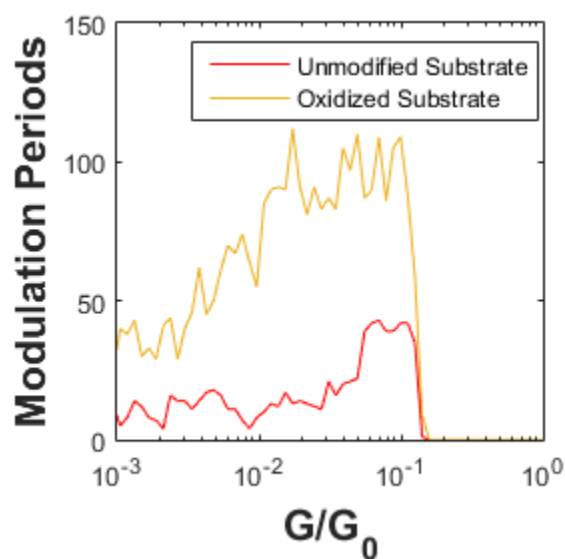


Figure D.2. A comparison of the modulation periods observed for an unmodified substrate and a substrate that has undergone electrochemical oxidation. An equivalent number of trajectories was collected for both substrates.

APPENDIX E:
EQUIPMENT PREPARATION FOR SINGLE MOLECULE CONDUCTANCE
MEASUREMENTS

E.1 CELL PREPARATION

The Teflon cell is cleaned prior to conductance measurements via piranha soaking. After 30 minutes of soaking in piranha solution, the cell is rinsed with DI water and dried with a low-fiber cloth (TechniCloth).



Figure E.1. The image shows the Teflon cell, which holds the substrates used for the break junction experiments.

E.2 STAGE PREPARATION

The stage is disassembled and the stage as well as the clip assembly components are washed with ethanol.



Figure E.2. The image shows the disassembled stage excluding the clip assembly.

Following the washing of the stage, the stage is reassembled. The Teflon cell is held onto the stage using the copper clip shown in Figure E.1.



Figure E.3. The completely assembled stage including the Teflon cell is shown here.

E.3 SCANNER PREPARATION

The STM tip is prepared by first washing the end portion of the gold wire with ethanol. Approximately 2 cm of the gold wire is cut from the end of the gold wire spool and held with tweezers. With the wire cutters nearly parallel to the wire, the gold wire is cut with an upward motion along the length of the gold wire. The sharpness of the gold wire tip is confirmed using a microscope.

After the gold wire for the STM tip is cut, the wire is inserted into the tube of the preamplifier tube such that the wire is strongly lodged and resistant to movement. The angle of the wire should be parallel to the angle of the preamplifier tube.



Figure E.4. The scanner with a gold tip inserted into the preamplifier tube is shown here.

E.4 APPLICATION OF THE EXTERNAL BIAS

To apply a modulated bias across the substrate-tip gap, the voltage must be applied externally from a function generator that is separate from the Agilent microscope electronics.



Figure E.5. The function generator (SRS Model DS345) used to apply the externally modulated bias is shown.

The output signal of the external function generator is connected to the breakout box of the Agilent 5500 SPM system via coaxial cables. Because the applied bias must also be measured during the experiment, the signal from the function generator is split and enters the breakout box in two ports.

One utilized port is the “Bias In” port. The “Bias In” port supersedes the internally applied bias when the port switch is in the “on” position. When the port switch is in the “off” position, the bias established by the Agilent software interface is applied.

The second port utilized is the “Friction” port. Friction is not measured when the software is in “STM” mode; therefore, the “Friction” port is otherwise useless during STM measurements. In the same manner as the “Bias In” port, the switch must be in the “on” position to read the externally applied bias.



Figure E.6. The breakout box for the Agilent 5500 SPM system is shown. The incoming coaxial cable from the function generator is split and enters the breakout box in the “Bias In” port and the “Friction” port. For each port, there is an on/off switch; the position of the switch shown here corresponds to “off” position for both ports.

In addition to the measurement of the current with respect to distance, the Agilent instrument will report the ‘friction’ measured as a function of distance; however, the ‘friction’ values on the y-axis indicate the applied bias (see Figure E.7).

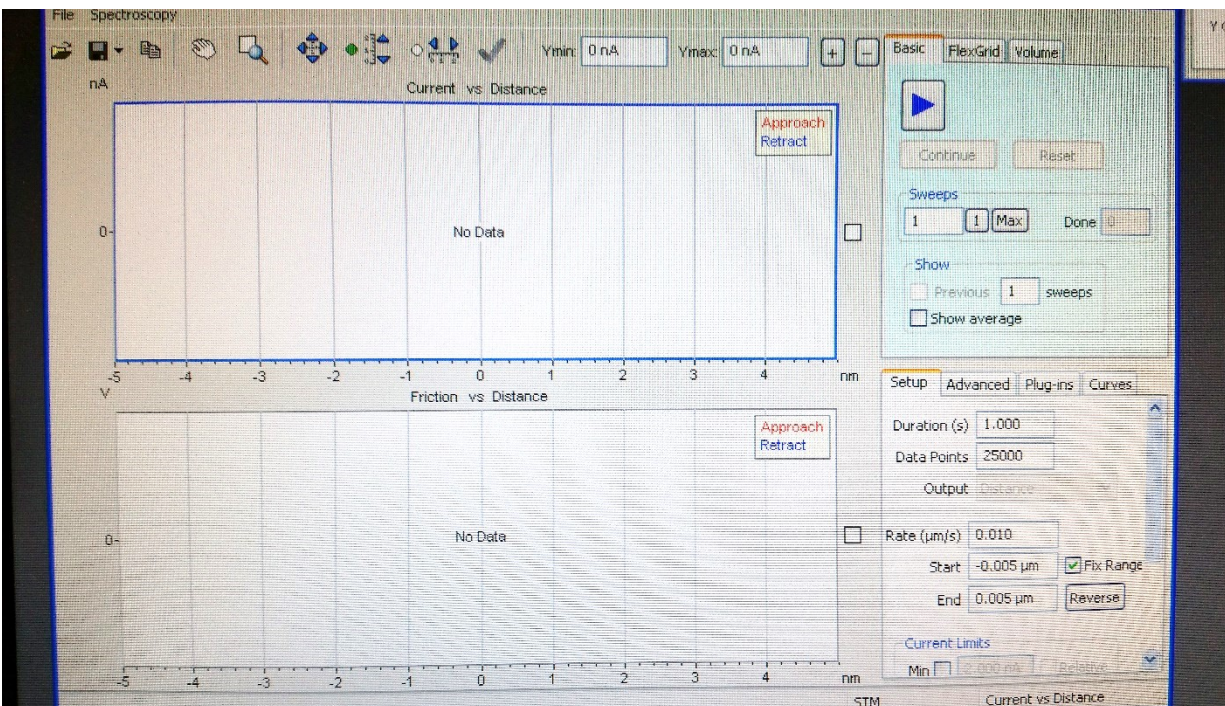


Figure E.7. The image shows the PicoView interface displaying the data panels including currents vs. distance and friction vs. distance measurements.

E.5 DATA ACQUISITION

Trajectories are collected via the PicoView interface. Figure E.7 shows an image of this software interface screen. The setup parameters are adjusted to the desired settings; and trajectories are collected with the “Collect” button in the “Basic” panel. Filenames are initially set as “_00001” and naturally iterate as trajectories are saved. Note that this format of the filename is necessary for the files to be correctly read by the data analysis scripts. Typical settings include 25,000 data points, a 1.000 second withdrawal duration, and a 10 nanometer withdrawal range.

E.6 DATA ANALYSIS

E.6.1 Reading and Filtering Trajectories

The collected trajectories are filtered and compiled into a dataset using the Matlab script shown below. Often, there will be current responses that show a steady decrease in the amplitude of each modulation period with increasing displacement. These current responses are assumed to arise from a poor break between the gold substrate and gold STM tip and not represent molecular junctions. Therefore, trajectories that do not show molecular current responses, yet persist for several modulation periods at a stable current are rejected.

readNmanual100:

```
function [Data]=readNmanual100(firstfile,lastfile,BiasType); %11/11/2014
scrsz = get(0,'ScreenSize');
imatrix=1;
for tn=firstfile:lastfile;
    if tn<10; pre='_0000'; elseif tn>=10 && tn<100; pre='_000';
        elseif tn>=100 && tn<1000; pre='_00'; elseif tn>=1000 && tn<10000; pre='_0'; else pre='_';
    end;
    titlenext=tn; fext='.txt'; tt=sprintf('%i',titlenext);titlenextstr=num2str(tt);
    titlenextstr=[pre,titlenextstr,fext];
    [t,s,I,V]=textread(titlenextstr,'%f%f%f%f',25000,'headerlines',168); [i]=tn;
    I=-1.*I;
    switch BiasType;
        case {'Constant','constant','const','Const'};
            leakage=I(25000,1); I=I-I(25000,1);
        case {'modulation','Modulation'}
            leakage=zeros(size(I));
    end;
    NominalFreq=1e3.*.5; %% 0.5 pre-set frequency
    IJ=fix((10./NominalFreq).*25000);
    for ij=1; % finding x0

        while I(ij)>150; ij=ij+2; if I==zeros(size(I))+100; break; end; end;
    end;
    min=ij-.2*IJ; max=ij+2.2*IJ;
    switch BiasType;
        case {'Constant','constant','const','Const'};
            if I==zeros(size(I)); min=1; max=2; end;
            leakage=leakage+I(max); I=I-I(max);
        case {'modulation','Modulation'};
```

```

if min<1000 | max>24000; min=1; max=2; end;
end;
figure('OuterPosition',[1 scrsz(4)/6 scrsz(3) scrsz(4)/1.2]);
subplot(1,3,1);
plot(t(min:max),I(min:max),'-');title(num2str(firstfile+tn-1));
xlabel('time / s'); ylabel('I / nA'); xlim([t(min) t(max)]);ylim([-0.1 1000]);
subplot(1,3,2);
plot(t(min:max),I(min:max),'-');
xlabel('time / s'); ylabel('I / nA'); xlim([t(min) t(max)]); ylim([-0.1 100]);
subplot(1,3,3);
plot(t((min):(max)),I((min):(max)),'-');
xlabel('time / s'); ylabel('I / nA'); xlim([t(min) t(max)]); ylim([-0.1 10]);
[screen]=[tn lastfile]; display(screen);
%manual selection of data
reply=input('analyze?','s');
if isempty(reply); end; str2num(reply);
if reply=='1'; Is=I;
Data(imatrix)=struct('t',t,'s',s,'I',Is,'leakage',leakage,'V',V); imatrix=imatrix+1;
elseif reply=='e'; break; end;
close(1);
end;
First=Data(1);
savefile='FIRST.mat';
save(savefile,'First');
savefile='DATAm.mat';
save(savefile,'Data');

```

E.6.2 Creating the Sample Trajectories

To create a library of sample current responses, the Simulink module shown in Figure E.8 is opened. The script shown below is then executed.

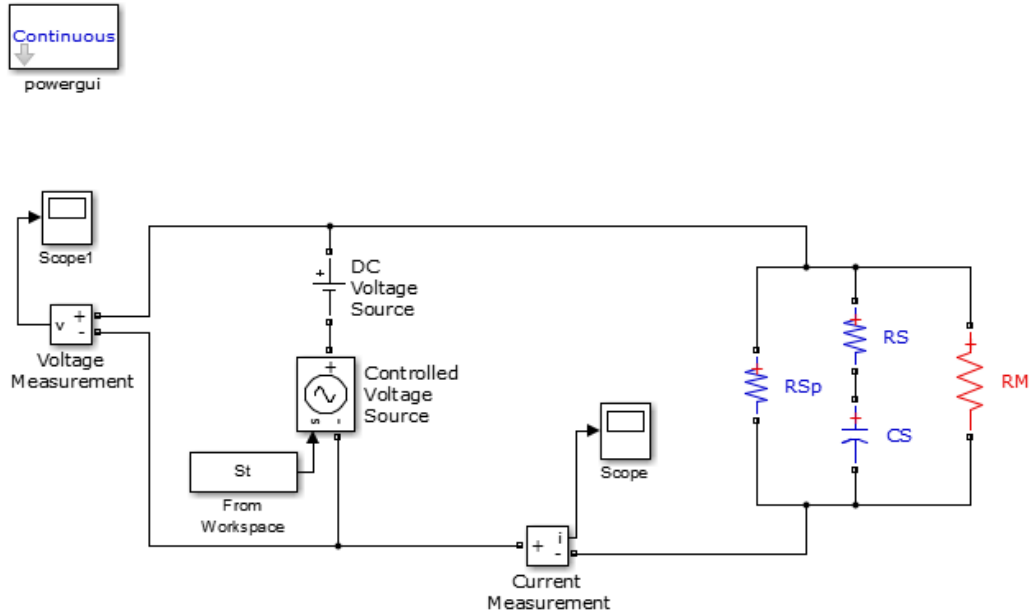


Figure E.8. Shown here is the Simulink module used to create the sample current responses. The circuit components shown in blue correspond to the solvent current and the circuit component shown in red is the molecular resistance that is varied to generate the library.

ResponseLibraryGenerator:

```

ModFreq=.5000; % in kHz
t=linspace(0,3/(ModFreq.*1e3),80);
S=.05*sawtooth(2.*pi.*500.*t,.5);
St=timeseries(S,t);
R=logspace(log10(1e4),log10(1e8),80);
for i=1:size(R,2);
set_param('RRCsim/RM','Resistance','R(i)')
sim('RRCsim')
Isymulated(i)=struct('tsym',Isym.time,'Isym',Isym.signals.values'.*1e9','R',R(i));
[i]
end;
RS=get_param('RRCsim/RS','Resistance');
CS=get_param('RRCsim/CS','Capacitance');
RSp=get_param('RRCsim/RSp','Resistance');
save CurrResLib.mat

```

E.6.3 Partitioning the Dataset

Each trajectory in the dataset is partitioned into individual modulation periods using the following script:

RpiecesVoltage(SolvMax,L,first):

```
function RpiecesVoltage(SolvMax,L,first); %06/22/2015
%ModFreq has to be measured before running the function (real frequency has
%to be determined /kHz
%-----
load DATAm.mat;%%load DATAusm.mat; %%DATAm.mat or DATA.m name changed in
directory for this analysis, so it is not overwritten
Imin=.01;
Imax=1000;
IAXIS=logspace(log10(Imin),log10(Imax),200);
IAXIS2D0=0; if Imin<=0; IAXIS2D0=1.1.*Imin; else IAXIS2D0=.9.*Imin; end;
IAXIS2D=cat(2,IAXIS2D0,IAXIS);
F=zeros(1,25000);
IJ=fix(25000.*L./40);
%%READING AND FILTERING DATA
tic;
%%-----
%%FileType=FileType;
%switch FileType;
% case 'ascii'
%[Data]=readN(firstfile,lastfile);
% case 'bin'
% [Data]=readNbin(firstfile,lastfile);
% end;
%assignin('base','Data',Data);
savefile='RFITPIECES.mat';
for imatrix=first:size(Data,2); [imatrix size(Data,2)]
iii=1; while Data(imatrix).V(iii)<2e-2; Data(imatrix).V(iii)=Data(imatrix).V(iii)+.1;end
    for ij=1; % finding x0
        while Data(imatrix).I(ij)>30; ij=ij+2; if ij>24000-IJ-9; break; end; end;
    end;
    %%phase matching etc
n=1; k0=1; ND=struct('t', {}, 'I', {});
for k=1:size(Data(imatrix).V,1);
    if Data(imatrix).V(k)<2e-2;
        n=n+1;
        k0=k+1;
    else j=k-k0+1;
        ND(n).t(j)=Data(imatrix).t(k); ND(n).I(j)=Data(imatrix).I(k);
    end; j=j+1;
end;
%removing solvent periods
z=1;
for i=1:size(ND,2);
    if isempty(ND(i).t)==1; continue;
    elseif size(ND(i).t,2)<5; continue;
```

```

elseif max(ND(i).I)>.95*Imax; continue;
elseif max(ND(i).I)<SolvMax; break;
else
    Pieces(imatrix,z)=ND(i); end; z=z+1;
end;
end;
toc;
assignin('base','Pieces',Pieces);
save(savefile,'Pieces');

```

E.6.4 Fitting the Partitioned Dataset

Each modulation period is fit using the library of current responses and the best fit is established using the following script:

```

Rfit:
function Rfit; %04/14/2015
%STEPS: 1-readN; 2-BreakJunctionModulation10nAVbiasmatchAusm; 3-Rpieces;
%-----
%%BLOCK 1 - READOUT OF THE DATA
load RFITPIECES.mat;
load CurrResLib.mat %%Depends on the library
tic;
%%resampling to match simulated data-----
for i=1:size(Pieces,1);
    for k=1:size(Pieces,2);
        if size(Pieces(i,k).I,2)>0;
            size(Pieces(i,k).I,2)
PiecesN(i,k).I=resample(Pieces(i,k).I,size(Isymulated(1,1).Isym,2),size(Pieces(i,k).I,2));
        ['resampling']
        [i k]
            end;
        end;
    end;
end;
%%-----
RFit=struct('R',{},'chi2',{});
for i=1:size(PiecesN,1);
    for k=1:size(PiecesN,2);
        g=zeros(size(Isymulated));
        for n=1:size(Isymulated,2);
            if size(Pieces(i,k).I,2)>0;
g(n)=ssqq(Isymulated(1,n).Isym,-1.*PiecesN(i,k).I);
            end;end;
N=find(g==min(g));N=N(1,1);
        [i k N]

```

```

RFit(i,k).R=Isymulated(1,N).R;
RFit(i,k).chi2=g(N);
clear g;
end;
end;
assignin('base','RFit',RFit);
toc;

```

E.6.5 Excluding the Worst-Fit Modulation Periods

The worst-fit modulation periods are excluded from the analysis by first establishing a level for the exclusion. To include the best x% of the fitted modulation periods, “lvl=x” is entered, where x is in decimal form. The included modulation periods are compiled and assigned to the resistance axis using the following script:

```

RfitLevel:
%reply=input('lvl','s');
%lvl=str2double(reply); lvl=num2str(lvl);
n=1;
for i=1:size(RFit,1);
for k=1:size(RFit,2);
if RFit(i,k).chi2>0;
    CHI2(n)=RFit(i,k).chi2;
    n=n+1;
end;
end;
end;
CHI2=sort(CHI2);
CHI2L=CHI2(fix(lvl.*size(CHI2,2)));
nR=zeros(size(RFit,1),size(R,2));
for i=1:size(RFit,1);
for k=1:size(RFit,2);
if RFit(i,k).chi2>0 & RFit(i,k).chi2<CHI2L;
nR(i,:)=nR(i,:)+hist(RFit(i,k).R,R);
end;end;end;
NR=sum(nR,1);

```